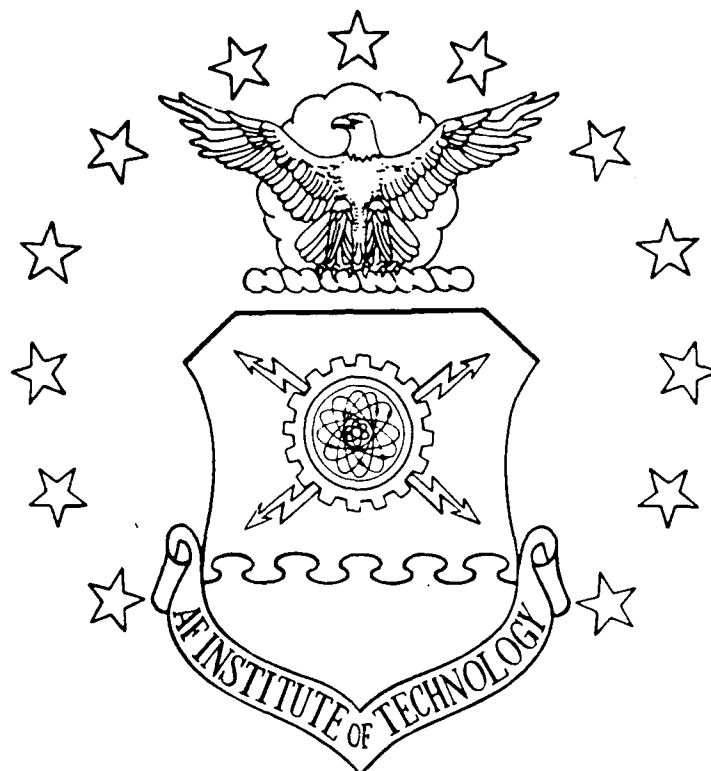


AD-A215 337



RIGOROUS CALCULATIONS OF LUMPED ELECTRICAL
PARAMETERS FOR A MICROSTRIP INTERDIGITATED
ELECTRODE STRUCTURE

THESIS

Henry Paul Leal
Captain, USAF

AFIT/GE/MA/89D-1

DISTRIBUTION STATEMENT A

Approved for public release
Distribution Unlimited

DEPARTMENT OF THE AIR FORCE
AIR UNIVERSITY

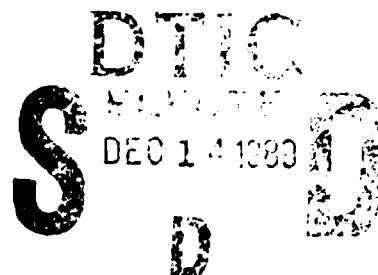
AIR FORCE INSTITUTE OF TECHNOLOGY

Wright-Patterson Air Force Base, Ohio

89 12 14 008

DTIC
ELECTE
DEC 14 1989
S
D
D

AFIT/GE/MA/89D-1



RIGOROUS CALCULATIONS OF LUMPED ELECTRICAL
PARAMETERS FOR A MICROSTRIP INTERDIGITATED
ELECTRODE STRUCTURE

THESIS

Henry Paul Leal
Captain, USAF

AFIT/GE/MA/89D-1

Approved for public release; distribution unlimited

AFIT/GE/MA/89D-1

RIGOROUS CALCULATIONS OF LUMPED ELECTRICAL
PARAMETERS FOR A MICROSTRIP INTERDIGITATED
ELECTRODE STRUCTURE

THESIS

Presented to the Faculty of the School of Engineering
of the Air Force Institute of Technology
Air University
In Partial Fulfillment of the
Requirements for the Degree of
Master of Science in Electrical Engineering

Henry Paul Leal, BSEE
Captain, USAF

December, 1989

Approved for public release; distribution unlimited

Accession For	
NTIS - CSAGI	<input checked="" type="checkbox"/>
DTIC TAB	<input type="checkbox"/>
Unannounced	<input type="checkbox"/>
Justification	
By	
Distribution	
Availability Codes	
Dist	
A-1	

Acknowledgments

Throughout the course of this research effort, I received guidance, advice, and encouragement from many sources. I especially want to thank my thesis advisor, Capt Gregory Warhola, for his guidance and overall assistance to this research, and Major Harry Barksdale for his contributions relating to electromagnetic theory. I also want to thank Major Edward Kolesar, Capt John Wiseman, and Capt Tom Jenkins for their contributions of pertinent CHEMFET data.

In addition, I would like to recognize a classmate, Capt James Cole, who introduced me to AFIT's ELXSI System 6400 (ICC-EMBOS) and AFIT's METALIB plotting routines. The ELXSI reduced the run time on my FORTRAN programs significantly, while METALIB provided excellent plots to illustrate my solutions.

Finally, I want to express my sincere appreciation to my wife Lynn, and my daughters Kelsey and Paula, for their continued love, encouragement, and support.

Henry Paul Leal

Table of Contents

	Page
Acknowledgments	ii
Table of Contents	iii
List of Figures	vii
List of Tables	x
Abstract	xi
I. Introduction	1-1
1.1 Purpose	1-1
1.2 Organization	1-1
1.3 Definitions	1-2
1.4 Background	1-3
1.4.1 CHEMFET.	1-4
1.4.2 Epoxy Resin Cure Sensor.	1-5
1.4.3 Background Analysis.	1-5
II. Problem Statement	2-1
2.1 Research Objective: Electrical Model	2-1
2.2 Identification of Lumped Electrical Parameters	2-1
2.3 Literature Review of Microstrip Parameters	2-2
2.3.1 Microstrip Interdigitated Electrode Structures.	2-3
2.3.2 Miscellaneous Microstrip Configurations.	2-4
2.4 Model Elements from the Electric Field	2-6

	Page
III. Problem Analysis	3-1
3.1 Periodic Structure	3-2
3.2 Five Layers of Material	3-2
3.3 Transverse Electromagnetic Wave in the Transverse Plane	3-4
3.4 Two-dimensional Frequency Limit	3-7
3.5 Laplace's Equation in the Transverse Plane	3-8
3.6 Boundary Conditions in the Transverse Plane	3-9
3.7 Analysis Summary	3-13
IV. Capacitance Solution	4-1
4.1 Potential in Each Layer	4-2
4.1.1 Potential Functions	4-2
4.1.2 Applying Boundary Conditions to Determine the Coefficients.	4-3
4.2 Charge Calculations	4-4
4.3 Evaluation of the Capacitive Elements	4-5
4.3.1 Cell Symmetry and the Eigenfunctions.	4-5
4.3.2 Symmetry and the Charge Function.	4-8
4.3.3 Capacitance to Ground: C_g	4-9
4.3.4 Capacitance Between Electrodes: C_E	4-9
4.4 Estimating the Potential Coefficients	4-10
V. Resistive Solution	5-1
5.1 Resistive Potential Functions	5-1
5.2 Applying Boundary Data Between Regions	5-2
5.3 Resistance Calculation	5-3
5.4 Estimating the Coefficients	5-5

	Page
VI. Numerical Results	6-1
6.1 Results of the Capacitive Solution	6-1
6.1.1 Potential Along the Boundaries.	6-1
6.1.2 Constant Voltage Contours.	6-6
6.1.3 Capacitance Graphs.	6-12
6.2 Results of the Resistive Solution	6-24
6.2.1 Illustrating the Resistive Potential Solution.	6-24
6.2.2 Resistive Element Graphs.	6-24
VII. Frequency Dependence of the Model Elements	7-1
7.1 Effects of Conductivity on the Frequency-Dependent Model Elements	7-5
7.2 Effects of Permittivity on the Frequency-Dependent Model Elements	7-10
7.3 Comparison of the Model Element Values (High Frequency and Frequency-Dependent)	7-11
7.4 Analysis of the Frequency-Dependent Results	7-18
VIII. Conclusion	8-1
8.1 Summary	8-1
8.2 Significance of the Thesis	8-3
8.3 Recommendations for Future Research	8-3
Appendix A. Detailed Capacitive Potential Solution	A-1
A.1 Potential in Layer 2	A-2
A.2 Potential in Layer 3	A-5
A.3 Potentials in Layers 4 and 5	A-8
A.4 Boundary Between Layers 2 and 3	A-13
A.5 Boundary Between Layers 3 and 4	A-21
A.6 Evaluation of I_m^1	A-23
A.7 Evaluation of I_m^2	A-24

	Page
A.8 Evaluation of I_{mn}^3	A-25
A.9 Summary of Linear Equations	A-29
A.10 Glossary of Variable Quantities	A-30
Appendix B. Detailed Charge Calculations	B-1
Appendix C. Detailed Resistive Potential Solution	C-1
C.1 Potential Solution for Region a	C-2
C.2 Potential Solution for Region b	C-5
C.3 Potential Solution for Region c	C-9
C.4 Boundary Between Regions	C-13
C.5 Summary of Coefficient Equations	C-18
Appendix D. List of Symbols	D-1
Bibliography	BIB-1
Vita	VITA-1

List of Figures

Figure	Page
1.1. Microstrip transmission line	1-2
1.2. Microstrip interdigitated electrode structure	1-3
1.3. Microstrip interdigitated electrode sensor structure	1-4
2.1. Microstrip interdigitated electrode sensor structure parameters	2-2
3.1. Periodic cell of interdigitated electrode sensor structure	3-3
3.2. Simplified model for the interdigitated electrode sensor structure	3-12
3.3. Problem diagram for model elements	3-14
4.1. Problem diagram for capacitive solution	4-1
5.1. Diagram of resistive layer	5-1
6.1. Potential function along lower boundary with $N = 10, 20$, and 50	6-3
6.2. Potential function along upper boundary with $N = 10, 20$, and 50	6-4
6.3. Potential function at the lower and upper boundaries with various d 's	6-5
6.4. Potential function at the lower and upper boundaries with various d 's (with sensor coating)	6-7
6.5. Constant voltage contours in cell using the case A data set	6-8
6.6. Constant voltage contours in cell using the case B data set	6-9
6.7. Constant voltage contours in cell using the case C data set	6-10
6.8. Constant voltage contours in cell using the case D data set	6-11
6.9. Constant voltage contours of the sensor cell with 40 contour levels	6-12
6.10. Constant voltage contours of the sensor cell with 80 contour levels	6-13
6.11. Capacitive element graphs for varying d , with air above the electrodes	6-15
6.12. Capacitive element graphs for varying d , with the sensor coating considered	6-16
6.13. Capacitive element graphs for varying h , with air above the electrodes	6-18

Figure	Page
6.14. Capacitive element graphs for varying h , with the sensor coating considered . . .	6-19
6.15. Capacitive element graphs for varying s , with air above the electrodes	6-21
6.16. Capacitive element graphs for varying h , with the sensor coating considered . . .	6-22
6.17. Capacitive element graphs for varying p , with the sensor coating considered . . .	6-23
6.18. Capacitive element graphs for varying permittivity in layer 4	6-25
6.19. Lower boundary of the resistive solution with $N = 10, 20$, and 50	6-26
6.20. Low frequency constant voltage contours (50) in the sensor coating layer	6-27
6.21. Low frequency constant voltage contours (100) in the sensor coating layer	6-27
6.22. Cell resistance graph for varying p	6-29
6.23. Cell resistance graph for varying s	6-30
6.24. Cell resistance graph for varying conductivity in the sensor coating	6-30
7.1. Behavior of the model elements versus frequency	7-3
7.2. R_p versus frequency (50 through 200 coefficients)	7-5
7.3. C_g versus frequency (50 through 200 coefficients)	7-6
7.4. C_E versus frequency (50 through 200 coefficients)	7-6
7.5. C_g versus frequency for $\sigma_4 = 10^{-7}, 10^{-8}$, and 10^{-10}	7-7
7.6. C_E versus frequency for $\sigma_4 = 10^{-7}, 10^{-8}$, and 10^{-10}	7-8
7.7. R_p versus frequency for $\sigma_4 = 10^{-7}, 10^{-8}$, and 10^{-10}	7-9
7.8. C_g versus frequency for $\epsilon_{r_4} = 20, 500, 1300$	7-12
7.9. C_E versus frequency for $\epsilon_{r_4} = 20, 500, 1300$	7-13
7.10. R_p versus frequency for $\epsilon_{r_4} = 20, 500, 1300$	7-14
7.11. Model Elements versus frequency for $\epsilon_{r_4} = 100$	7-15
7.12. Model Elements versus frequency for $\epsilon_{r_4} = 75$	7-16
7.13. Model Elements versus frequency for $\epsilon_{r_4} = 50$	7-17
7.14. Input impedance using frequency-dependent and high frequency elements values	7-19
7.15. Inter-terminal impedance using frequency-dependent and high frequency elements values	7-20

Figure	Page
A.1. Problem diagram for the detailed capacitive solution	A-1
B.1. Contour for Charge Integration	B-1
C.1. Diagram of resistive layer for detailed solution	C-1

List of Tables

Table	Page
6.1. Normalized data used for boundary potentials (with no coating)	6-2
6.2. Normalized data used for boundary potentials (with coating)	6-6
6.3. Data used for voltage contour plots	6-6
6.4. Normalized model parameters used as the baseline for capacitance calculations .	6-14
6.5. Normalized model parameters used as baseline for the resistive calculations . . .	6-28
7.1. Normalized data used for the frequency analysis	7-2

Abstract

This research investigates a microstrip interdigitated electrode structure used in integrated circuit sensors and presents an electrical model for the device. The structure is assumed to: (1) have a periodic arrangement of interdigitated electrodes, (2) have electrodes of sufficient length to ignore effects created by the ends of the structure, (3) be operating at a sufficiently low frequency, where the potential is essentially constant along the electrode's length and where the substrate is essentially a conductor, and finally (4) have five layers of homogeneous, isotropic, non-magnetic material in the plane transverse to the structure's length. Within these constraints, the problem focuses on solving for the potential distribution using Laplace's equation.

The electrical model developed consists of three elements—a capacitance from each of two electrodes to ground, a capacitance between the electrodes, and a resistance through the sensor coating. The values for the individual elements are found from the potential solution. Potential functions, in the form of infinite Fourier series, are developed for each layer within a periodic cell. The coefficients of the Fourier series are determined by matching boundary conditions across interfaces between the material layers. These coefficients are estimated numerically by truncating the infinite series, and solving a linear system of equations.

Results are presented for a variety of cell parameters (cell dimensions and material properties), which illustrate the dependence of the individual elements on these cell parameters. Specifically, the results indicate that all model elements are strongly influenced by the electrical properties of the sensor coating; and therefore, all elements play a major role in the sensing action of the device. The frequency dependence of the model parameters are also developed, using a complex permittivity. Results are presented for various material parameters, which illustrate the high and low frequency limits of all model elements with a transition centered at the frequency where the sensor coating changes from a conductor to a lossy dielectric.

RIGOROUS CALCULATIONS OF LUMPED ELECTRICAL PARAMETERS FOR A MICROSTRIP INTERDIGITATED ELECTRODE STRUCTURE

I. Introduction

1.1 Purpose

This thesis investigates the microstrip interdigitated electrode structure used in integrated circuit sensors and presents an electrical model for the device. The electrical parameters of interest are developed using the potential distribution within the device.

1.2 Organization

The remainder of this chapter contains definitions of key terms and summaries of previous research which motivated this thesis topic. Chapter II presents the specific thesis problem and reviews related research investigating similar topics. Chapter III provides an analysis of the interdigitated electrode sensor structure, which leads to a simplified mathematical model. This analysis also introduces an approximation under which the potential distribution satisfies Laplace's equation in the transverse plane; it also provides the mathematical conditions that this transverse potential distribution must satisfy. Chapter IV presents the solution for the capacitive elements, while Chapter V presents the solution for the resistive element. Numerical results of the research are presented for a particular device in Chapter VI, including graphs of the model elements with respect to variations of the physical and material aspects of the structure. In addition, constant voltage contour plots of the structure are presented to illustrate the solution. Chapter VII presents a frequency analysis of the model using complex permittivity, which displays the effects of the

sensor coating's permittivity and conductivity on the, now, frequency-dependent lumped elements. The thesis concludes with a brief summary and recommendations for further research.

1.3 Definitions

The key terms related to this research effort are microstrip transmission line, interdigitated electrode structure, and interdigitated electrode sensor structure.

A *microstrip* is a conducting metal strip used in electronic circuits to convey electrical energy from one circuit component to another. A layer of insulating dielectric material separates the strip of metal from a substrate having bulk dielectric and conductive properties (see Figure 1.1). A ground plane is located below the substrate.

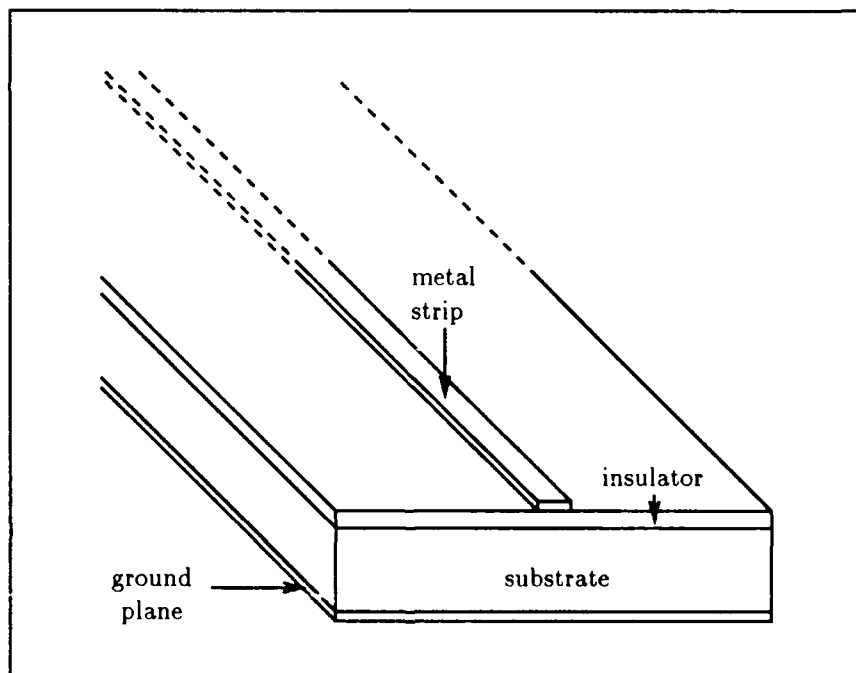


Figure 1.1. Microstrip transmission line

An *interdigitated electrode structure* is a configuration similar to two forks with their tines interlaced. The microstrip interdigitated electrode structure is a configuration of interlaced mi-

crostrips (fingers), where each microstrip segment is located between two microstrips from the other electrode (see Figure 1.2).

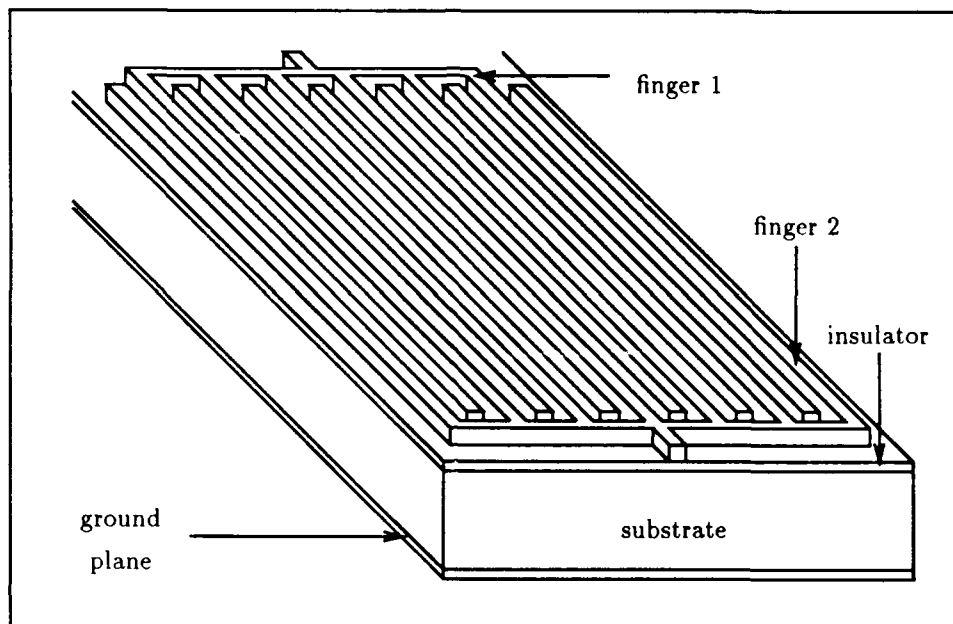


Figure 1.2. Microstrip interdigitated electrode structure

An *interdigitated electrode sensor structure* uses the microstrip interdigitated electrode structure with a special coating applied over the structure (see Figure 1.3). The coating material has variable electrical properties, which are dependent on external events and which change the electrical performance of the structure. The sensor's fundamental purpose is to detect these changes.

1.4 Background

Integrated circuit sensors are miniaturized versions of the interdigitated electrode sensor structure along with support electronics necessary to monitor its electrical performance. Two such devices are offered as examples—a chemically-sensitive field-effect transistor (CHEMFET) and a resin cure sensor.

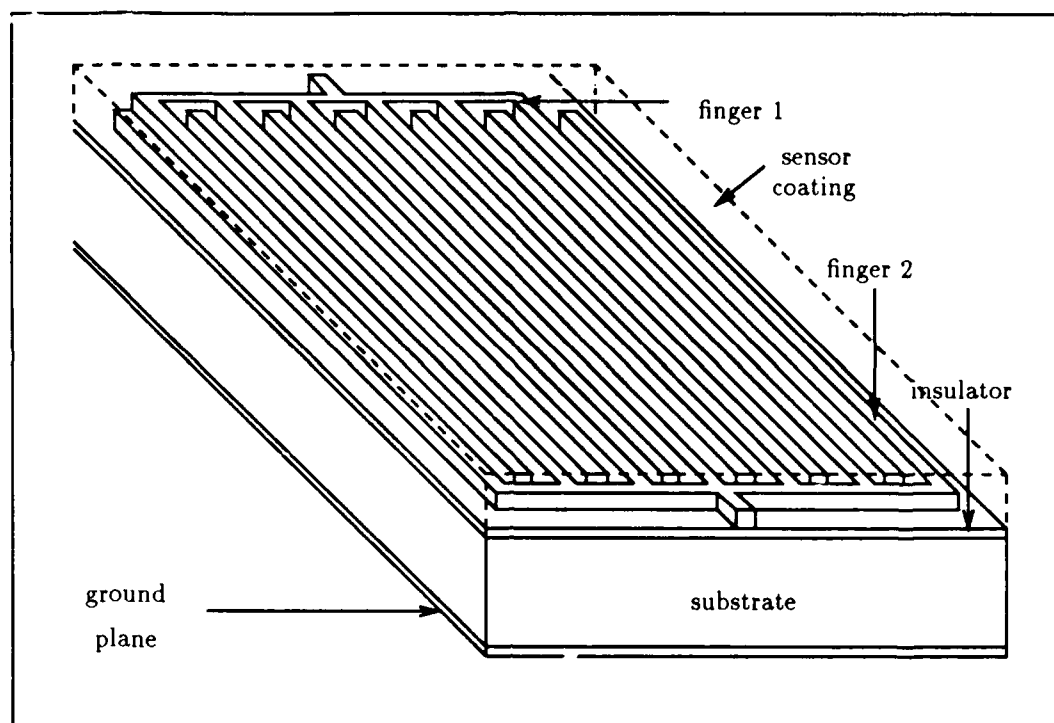


Figure 1.3. Microstrip interdigitated electrode sensor structure

1.4.1 *CHEMFET*. Wiseman investigated two different (small and large) interdigitated electrode sensor structures utilizing the CHEMFET configuration [18]. He coated the interdigitated structure with a special polymer (copper phthalocyanine) whose electrical properties are sensitive to certain environmentally-sensitive gas contaminants (nitrogen dioxide and diisopropyl methylphosphonate). The large interdigitated structure had 29 inner fingers and 30 outer fingers. These fingers were $7.5\ \mu\text{m}$ wide, $3.792\ \text{mm}$ long, and they were separated from each other by $9.0\ \mu\text{m}$. The small interdigitated structure had 15 inner fingers and 16 outer fingers. These fingers were $6.0\ \mu\text{m}$ wide, $3.792\ \text{mm}$, and were similarly separated from each other by $9.0\ \mu\text{m}$.

Wiseman did not mathematically analyze his interdigitated structure (from an electromagnetic perspective), and the dimensions were chosen based upon fabrication design rules. Wiseman cited work by Lee (section 1.4.2) as validation for using the interdigitated structure. Wiseman rec-

ommended further research regarding the interdigitated structure, with the goal of mathematically predicting a physical configuration which offers the greatest electrical response to a given variation in the coating material's electrical properties, thereby creating an optimum sensing capability.

1.4.2 Epoxy Resin Cure Sensor. Lee presented an epoxy resin cure sensor using an interdigitated structure [14]. He coated the interdigitated structure with epoxy resin whose electrical properties vary depending on the epoxy's cure state. Lee's interdigitated structure had nine inner and ten outer fingers. The fingers were 12.5 μm wide, 5 mm long, and were separated from each other by 12.5 μm .

Lee performed a detailed analysis of his interdigitated structure. He developed a circuit model of the structure using a finite difference numerical solution to determine the potential distribution. Using the finite difference method, unknown voltages were determined at discrete points throughout the structure. This led to a large number of unknowns (10,000 for a 100 by 100 point grid). Since the potential distribution is valid only for a specific physical configuration, these unknowns were determined for each structural arrangement under investigation. While the finite difference technique yields valid results, it can be advantageous to solve for the potential distribution with a method requiring fewer unknowns. In addition, Lee's analysis assumed the microstrips were infinitely thin, which limited his results. For future research, Lee recommended a full analysis of the interdigitated structure using microstrips with finite height.

1.4.3 Background Analysis. In each of the integrated sensor circuits described, most of the interdigitated electrode structure dimensions were influenced by fabrication limitations. While each of these research efforts demonstrated the effectiveness of the interdigitated electrode sensor structure, each recommended further research to investigate a physical configuration which would yield the best sensor, or simply have the greatest electrical response to any changes in the applied coating's material properties.

II. Problem Statement

2.1 Research Objective: Electrical Model

To adequately predict an optimum design for the interdigitated electrode sensor structure, a lumped element electrical model of the device is proposed. The problem solved in this thesis is the development of lumped electrical parameters to describe the device. This chapter describes the specific electrical parameters being addressed and reviews the literature concerning the methods utilized to determine similar parameters.

2.2 Identification of Lumped Electrical Parameters

The individual parameters under investigation are described below. They are a capacitance associated with the substrate and insulator, resistance of the substrate, capacitance between electrodes, and resistance between electrodes (Figure 2.1).

Capacitance Associated with the Substrate and Insulator. For an applied voltage, there is a corresponding charge distribution on each finger. This charge can be used to define a capacitance value between each finger and the ground plane below. The total capacitance is the combination of a capacitance associated with the substrate (labeled C_s in Figure 2.1) and a capacitance associated with the insulator (labeled C_i in Figure 2.1).

Resistance of the Substrate. The substrate is composed of a material having bulk conductive properties. Thus, the substrate will provide some resistance between the oxide and the ground plane. This resistance is labeled R_s in Figure 2.1.

Capacitance Between Electrodes. A capacitance between the electrodes can be defined based upon the charge and potential differences between the two electrodes. This capaci-

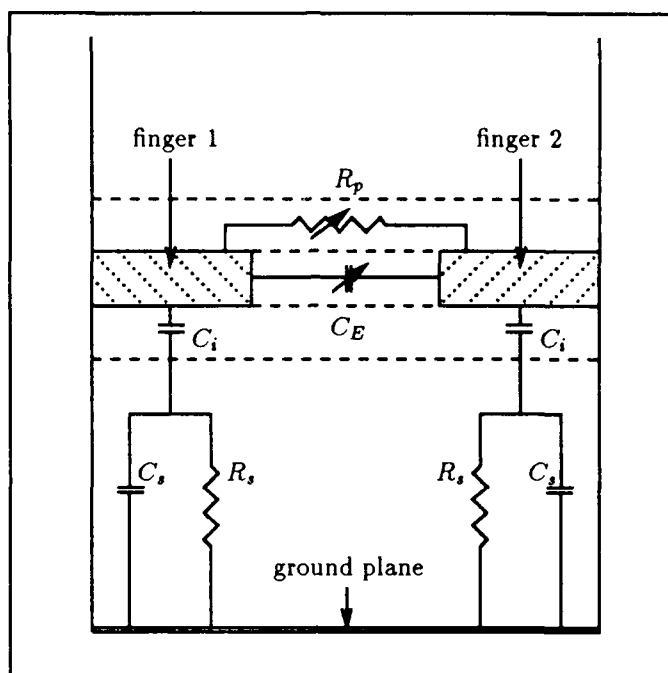


Figure 2.1. Microstrip interdigitated electrode sensor structure parameters

tance value varies due to the electrical properties of the sensor coating. The capacitance between electrodes is labeled C_E in Figure 2.1.

Resistance Between the Electrodes. Because the sensor coating is partially conductive, there is a finite resistance between the two electrodes. This resistance typically varies with respect to the chemical properties and state of the sensor coating, and it is labeled R_p in Figure 2.1.

2.3 Literature Review of Microstrip Parameters

Several authors have investigated microstrip parameters in various configurations. This section reviews microstrip interdigitated electrode structures and miscellaneous microstrip configurations.

2.3.1 Microstrip Interdigitated Electrode Structures. The literature concerning other interdigitated electrode structures typically offers analysis of the fingers in a specific configuration. Unfortunately, the interdigitated electrode sensor structure is unique because of the partially conductive coating covering the electrode fingers. However, the approach and analysis of similar structures without sensor coatings provides insight into the techniques that can be employed to analyze the interdigitated electrode sensor structure.

Interdigital Capacitor. Alley analyzed a thin film interdigital capacitor [2]. His interdigitated structure contained an even number of fingers (equal number per electrode) and the fingers had equal width and separation. Alley determined the capacitance of his structure using even and odd mode capacitance formulas for coupled lines developed by Smith [15]. While Alley did consider possible resistance between the electrodes (due to a lossy dielectric beneath the fingers), his analysis was limited to infinitely thin electrodes (no finite height).

Interdigitated Microstrip Parameters. Dalby presented interdigitated microstrip circuit parameters for both single and coupled microstrips [5]. His physical arrangement included an arbitrary material layer above the microstrips and arbitrary dimensions for all finger features. Dalby presented parameter formulas for both thin and thick single microstrips, as well as odd and even mode parameter formulas for the thin coupled microstrips. Unfortunately, these formulas were presented without derivation or reference, which limited this reader's ability to modify his results for other configurations or verify the accuracy of his formulas.

Smith developed formulas for even and odd mode capacitances for coupled microstrips using conformal mapping techniques [15]. As with Dalby's work, Smith considered arbitrary material layers above and below the microstrips with arbitrary dimensions for the coupled strips. While Smith rigorously presented the upper and lower bounds to the capacitance values, his results do not apply to this specific problem because he employed a shielding enclosure and microstrips of infinitesimal height.

2.3.2 Miscellaneous Microstrip Configurations. Aside from interdigitated structures, many articles have been published concerning microstrip transmission lines that may be useful in analyzing the interdigitated electrode sensor structure. In all of the articles discussed below, the electrical parameters were calculated by first determining the electric field associated with a specified physical configuration. While none of the arrangements match the interdigitated electrode sensor structure exactly, the generalized method provides a logical approach for developing a solution to this thesis problem (seek the electric field associated with the interdigitated electrode sensor structure).

Microstrips in Various Configurations. Yamashita and Atsuki analyzed shielded stripline within three layers of material using a Green's function and a variational method [19]. They developed expressions for the line capacitance and other strip parameters (characteristic impedance, wavelength, and wave velocity). While they considered the thickness of the stripline conductors, they did not address coupled strips. Because of this limitation and their shielded enclosure, their results did not apply to the interdigitated electrode sensor structure.

Kitazawa and Hayashi analyzed two-line [10] and three-line [11] coupled, thin striplines embedded in three layers of anisotropic material with ground planes above and below these layers. They developed a capacitance matrix using a Green's function and a variational method. Expressions for the line capacitance and other line parameters (characteristic admittance, impedance matrix, and inductance) were presented. Since they neglected strip height and used an upper ground plane, their results are not adaptable to this thesis problem.

Krage and Haddad investigated shielded single and coupled thin microstrips embedded in two and three layers of material [12]. They solved for the electric and magnetic fields, using a Fourier series representation for the fields, and determined the Fourier coefficients from the boundary conditions between layers. They presented expressions for the line capacitance and other parameters (characteristic impedance and line inductance) based upon the field solutions. Since

the microstrips were shielded and strip height was neglected, their results do not apply to the interdigitated electrode sensor structure.

Judd and others analyzed shielded single and coupled thick microstrips embedded in two layers of material [8]. A Fourier series representation of the potential in each layer was presented, and the Fourier coefficients were determined using the boundary conditions between layers. They presented an expression for the capacitance based upon the potential solution, and the capacitance was estimated by truncating the infinite series. These specific results did not apply to the thesis problem, because a shielded enclosure was incorporated and only two layers of material was considered. However, this method did seem suitable for analyzing the interdigitated electrode sensor structure.

Hill and others investigated coupled microstrips and triplates in a single medium [6]. They solved for the electric field within the structure using an infinite series form of a Green's function. An expression for the capacitance was then developed from the field solution. The specific results do not apply to the interdigitated electrode sensor structure, because their analysis incorporated only one material layer.

General Multi-Conductor Capacitance Matrix. Weeks presented a generalized method for determining a capacitance matrix for multi-conductor transmission lines [17]. With this technique, the conductors are set to specific potential levels, which isolates each capacitance term and allows each capacitive element to be determined separately. Kitazawa used this method for the case of a multi-microstrip configuration [9]. While these microstrips were not arranged in an interdigitated configuration, Kitazawa proved that Weeks' technique is also suitable for analyzing microstrips. Kitazawa developed expressions for the electric and magnetic fields within his arbitrary arrangement of equal height microstrips using a dyadic Green's function. Once the fields were known, Kitazawa used Weeks' method to determine all resulting capacitance parameters. Because Kitazawa did not consider conductive materials, his specific results do not apply to the thesis problem.

2.4 Model Elements from the Electric Field

The importance of the electric field was illustrated throughout the previous articles. Once the electric field was determined for a particular microstrip structure, the electrical parameters of interest were found using fundamental relationships, such as Gauss' law and Ohm's law.

Capacitive Elements. The charge, Q , on the microstrip electrode is found using Gauss' law by integrating the electric flux density over a suitable surface, γ , enclosing the electrode. Capacitance, C , is then found from the relationship $Q = CV$, where V is the voltage potential. Using a forcing potential of 1 volt yields

$$C = Q = \oint_{\gamma} \epsilon E_n dl \quad (2.1)$$

where ϵ is the permittivity of the material, E_n is the electric field normal to the surface, and dl is an element of surface area.

Resistive Elements. Within conductive regions, the current density, \mathbf{J} , is found using the relationship $\mathbf{J} = \sigma \mathbf{E}$, where σ is the conductivity of the material and \mathbf{E} is the electric field. The current through the conductive region is found by integrating the current density over a suitable surface (γ), through all of the current paths. The resistance is then found using Ohm's law, $V = IR$, where I is the current and R is the resistance, or equivalently $G = I/V$, where G is the conductance ($G = 1/R$). Using a forcing potential of 1 volt yields

$$G = \int_{\gamma} J_n dl = \int_{\gamma} \sigma E_n dl \quad (2.2)$$

where J_n and E_n are the current density and electric field, respectively, normal to the surface.

Therefore, to develop the electrical model elements, we seek a solution to the electric field within the microstrip interdigitated electrode sensor structure.

III. Problem Analysis

It was shown in the previous chapter that the electrical parameters of interest can be determined from the electric field within the interdigitated electrode structure. Since the electric field can be found directly from the potential distribution, the thesis concentrates on solving for the potential distribution within the interdigitated electrode sensor structure. This research further concentrates on the plane transverse to the length of the structure, since the length is the largest single dimension (an electrode finger is much longer than its width or height). Therefore the effects at the structure's endpoints (the bus where the appropriate digits are joined) are neglected. According to Alley [2:1029], neglecting end-effects introduces only a small error (less than 2%) in the capacitance values. End-effects are also ignored in this thesis for the resistive element, although no analysis is provided, nor is any reference, to support this approximation. Towards the objective of solving for the potential, the physical structure must be analyzed to determine the mathematical conditions that the potential must satisfy.

In section 3.1, the periodic nature of the interdigitated electrode sensor structure is addressed and a corresponding periodic cell is created to represent the interdigitated structure, while the material layers within the cell are defined in section 3.2. In section 3.3, a relationship is developed between the electric field and the transverse potential, using a transverse electromagnetic (TEM) wave analysis. An upper frequency bound for the analysis is then established in section 3.4, which reduces the electric field to simply the gradient of the transverse potential. In section 3.5, this potential is shown to satisfy Laplace's equation. Section 3.6 discusses the boundary conditions between the layers, which lead to specific boundary conditions that a high and low frequency potential solution must satisfy. Finally, in section 3.7, a summary is presented to consolidate the analysis.

3.1 Periodic Structure

As viewed from the transverse plane (transverse to the length of the electrodes), the interdigitated electrode sensor structure possesses a repetitive pattern consisting of two adjacent electrode fingers (refer to Figure 1.3). Since the interdigitated electrode sensor structure contains many fingers (59 in the CHEMFET), this pattern repeats itself 30 times. Hence, a periodic cell can be created to represent the interdigitated electrode structure. This approximation introduces an error for the outer few sets of fingers, but fortunately, this perturbation only represents a small portion of the total structure. The arrangement consisting of one-half of each finger is considered the periodic cell (see Figure 3.1). This periodic condition requires a vanishing normal component of the electric field on the vertical walls of the cell. Considering the vertical direction to be the y -axis, this situation implies that at the cell walls

$$E_x = 0 \quad (3.1)$$

where E_x is the x component of the electric field, or alternately,

$$\frac{\partial V}{\partial x} = 0 \quad (3.2)$$

where V is the voltage, or potential.

3.2 Five Layers of Material

There are five layers of material present in the periodic cell. The first layer is the substrate material, which is directly above the ground plane. The second layer is the insulator material, which is located beneath the interdigitated electrodes. The third layer represents the region between the fingers. Due to the integrated circuit fabrication process, this layer is part insulator (or passivation) material, part sensor coating, and part air. For simplification, this layer will be designated insulator, but the model will remain flexible and allow arbitrary material parameters in a homogeneous layer. The fourth layer is the sensor coating, while the fifth layer is air. Each region has an associated

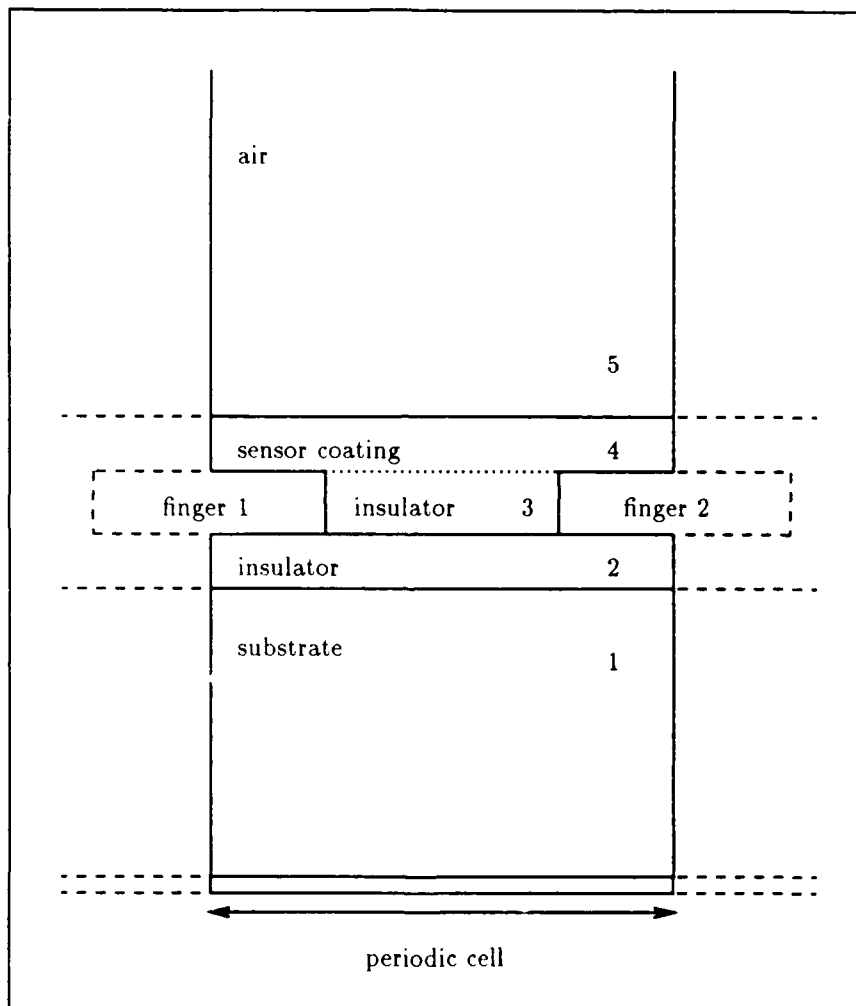


Figure 3.1. Periodic cell of interdigitated electrode sensor structure

permittivity (ϵ), while the substrate and sensor coating possess finite conductivity (σ) as well. The permeability of each region is considered equal to the permeability of free space (μ_0). These layers are also identified in Figure 3.1. To simplify the model, each material layer is considered homogeneous and isotropic; that is, the material and electrical properties are uniform throughout their bulk material.

3.3 *Transverse Electromagnetic Wave in the Transverse Plane*

In solving for the electric field within the interdigitated electrode sensor structure, it is necessary to establish a relationship between the structure's electric field and the potential within the periodic cell. Towards this objective, the electrodes are considered perfect conductors, and all the current within the structure is considered to be along the length of the structure, thereby assuming transverse electromagnetic (TEM) fields within the microstrip structure. While the metal may not be ideal and some transverse current can be expected, these assumptions provide a starting point for the analysis and provide a basis to establish a relationship between the potential and the electric field. The following analysis summarizes the discussion in Collins [3:67-70]. Let z denote the direction which aligns with the length of the interdigitated structure, with y denoting the vertical direction (with respect to the periodic cell), and x denoting the horizontal direction (with respect to the periodic cell). The basic TEM premise is

$$E_z = H_z = 0 \quad (3.3)$$

where E_z and H_z are the z components of the electric and magnetic fields, respectively. Equation 3.3 implies a perfect conductor, and all the current is in the z direction. The corresponding time-harmonic Maxwell equations, for $\exp(j\omega t)$ time dependence, are

$$\nabla \times \mathbf{E}_t = -j\omega\mu\mathbf{H}_t \quad (3.4)$$

$$\nabla \times \mathbf{H}_t = j\omega\epsilon\mathbf{E}_t \quad (3.5)$$

where \mathbf{E}_t and \mathbf{H}_t are the transverse electric and magnetic fields, respectively, ω is the angular (excitation) frequency, μ and ϵ are the material's permeability and permittivity, respectively, and $j = \sqrt{-1}$. Since

$$\nabla = \hat{x} \frac{\partial}{\partial x} + \hat{y} \frac{\partial}{\partial y} + \hat{z} \frac{\partial}{\partial z} \quad (3.6)$$

where \hat{x} , \hat{y} , and \hat{z} are the unit vectors in the x , y , and z directions, respectively. Let

$$\nabla_t = \hat{x} \frac{\partial}{\partial x} + \hat{y} \frac{\partial}{\partial y} \quad (3.7)$$

$$\nabla_z = \hat{z} \frac{\partial}{\partial z} \quad (3.8)$$

Then, we may write

$$\nabla = \nabla_t + \nabla_z \quad (3.9)$$

Accordingly, Maxwell's equations can be expressed as

$$(\nabla_t \times \mathbf{E}_t) + (\nabla_z \times \mathbf{E}_t) = -j\omega\mu\mathbf{H}_t \quad (3.10)$$

$$(\nabla_t \times \mathbf{H}_t) + (\nabla_z \times \mathbf{H}_t) = j\omega\epsilon\mathbf{E}_t \quad (3.11)$$

Using Equation 3.3, the curl of the transverse electric and magnetic fields are

$$\nabla \times \mathbf{E}_t = \hat{z} \left(\frac{\partial E_y}{\partial x} - \frac{\partial E_x}{\partial y} \right) \quad (3.12)$$

and

$$\nabla \times \mathbf{H}_t = \hat{z} \left(\frac{\partial H_y}{\partial x} - \frac{\partial H_x}{\partial y} \right) \quad (3.13)$$

Thus

$$\nabla_t \times \mathbf{E}_t = 0 \quad (3.14)$$

$$\nabla_t \times \mathbf{H}_t = 0 \quad (3.15)$$

$$\nabla_z \times \mathbf{E}_t = -j\omega\mu\mathbf{H}_t \quad (3.16)$$

$$\nabla_z \times \mathbf{H}_t = j\omega\epsilon\mathbf{E}_t \quad (3.17)$$

Since $\nabla_t \times \mathbf{E}_t = 0$, Equations 3.14, 3.15, 3.16, and 3.17 will be satisfied by

$$\mathbf{E}_t = g_1(z)\nabla_t\phi(x, y) \quad (3.18)$$

$$\mathbf{H}_t = g_2(z)\nabla_t\psi(x, y) \quad (3.19)$$

where g_1 , g_2 , ϕ , and ψ are scalar functions which need to be determined. From Equation 3.16

$$\mathbf{H}_t = -\frac{1}{j\omega\mu}\nabla_z \times \mathbf{E}_t \quad (3.20)$$

Using Equation 3.20 in 3.17 yields

$$\nabla_z \times \nabla_z \times \mathbf{E}_t = \omega^2\mu\epsilon\mathbf{E}_t \quad (3.21)$$

Using the identity

$$\nabla_z \times \nabla_z \times \mathbf{E}_t = \nabla_z (\nabla_z \cdot \mathbf{E}_t) - \nabla_z^2 \mathbf{E}_t \quad (3.22)$$

and the fact that

$$\nabla_z \cdot \mathbf{E}_t = 0 \quad (3.23)$$

yields

$$\nabla_z \times \nabla_z \times \mathbf{E}_t = -\nabla_z^2 \mathbf{E}_t \quad (3.24)$$

Using Equation 3.24 in 3.21 yields

$$\frac{\partial^2 \mathbf{E}_t}{\partial z^2} + k^2 \mathbf{E}_t = 0 \quad (3.25)$$

where $k^2 = \omega^2 \mu \epsilon$, and k is the wavenumber associated with the material. Using Equation 3.18 in 3.25 yields

$$g_1''(z) \nabla_t \phi(x, y) + k^2 g_1(z) \nabla_t \phi(x, y) = 0 \quad (3.26)$$

where the prime symbol denotes differentiation with respect to z . For a non-trivial transverse field, this implies

$$g_1''(z) + k^2 g_1(z) = 0 \quad (3.27)$$

Hence

$$g_1(z) = A_{\pm} \exp(\pm j k z) \quad (3.28)$$

where A_{\pm} is an arbitrary constant. Using Equation 3.28 in 3.18 yields

$$\mathbf{E}_t = A_{\pm} \nabla_t \phi(x, y) \exp(\pm j k z) \quad (3.29)$$

3.4 Two-dimensional Frequency Limit

In solving for the electric field, it can be advantageous to remove the z dependence from the electric field. Therefore, let us consider the power series expansion of the $\exp(\pm j k z)$ terms in Equation 3.29

$$\exp(\pm j k z) = 1 \pm (j k z) + \frac{(j k z)^2}{2!} \pm \frac{(j k z)^3}{3!} + \dots \quad (3.30)$$

Thus, if $k z \ll 1$, Equation 3.29 simplifies to

$$\mathbf{E}_t \approx \nabla_t \phi(x, y) \quad (3.31)$$

where the arbitrary constant (A_{\pm}) was absorbed into $\phi(x, y)$. Equation 3.31 indicates that, for $k z \ll 1$, the potential in the transverse plane is essentially constant along the z direction, and the subscript t notation can be deleted since all remaining functions are transverse functions. Thus,

$$\mathbf{E} = \nabla \phi(x, y) \quad (3.32)$$

Since the wavenumber, k , is related to frequency by

$$k = \omega \sqrt{\mu \epsilon} = \omega \sqrt{\mu_0 \epsilon_0} \sqrt{\epsilon_r} \quad (3.33)$$

there is a specific frequency associated with the condition that $kz = 1$, which limits the use of the approximation of Equation 3.31 (all cell layers contain nonmagnetic material; that is $\mu_r = 1$).

Since $c = \frac{1}{\sqrt{\mu_0 \epsilon_0}} \approx 3 \cdot 10^{10}$ cm/sec, where c is the speed of light in a vacuum, the frequency limit (ω_L) imposed due to the length of the fingers (L) is

$$\omega_L = \frac{c}{L \sqrt{\epsilon_r}} \quad (3.34)$$

For the interdigitated electrode in the CHEMFET, $L \approx 0.4$ cm, and the largest-valued ϵ_r is associated with layer 4 (mean value for the polyphthalocyanine polymers is $\epsilon_r \approx 650$, with an overall range of 16-1300 [4:167]). Thus, for this case

$$\omega_L \approx \frac{3 \cdot 10^{10}}{0.4 \sqrt{650}} = 2.94 \cdot 10^9 \text{ rad/sec} \quad (3.35)$$

which translates to an ordinary frequency limit, f_L , associated with this length as

$$f_L = \frac{\omega_L}{2\pi} = 468 \text{ MHz} \quad (3.36)$$

Thus, for frequencies as large as 50 MHz ($f \ll f_L$), the electric field in the CHEMFET's interdigitated electrode structure is essentially constant along the z direction, thereby transforming the three-dimensional problem into a two-dimensional problem in x and y .

3.5 Laplace's Equation in the Transverse Plane

In the transverse plane, the electric field must satisfy

$$\nabla_t \cdot \mathbf{E}_t = \frac{\rho}{\epsilon} \quad (3.37)$$

where ρ is the charge density. In a charge free region away from the conductors, this equation simplifies to

$$\nabla_t \cdot \mathbf{E}_t = 0 \quad (3.38)$$

The subscript t notation can be dropped, since the only variables remaining are in the transverse, x - y , plane and Equation 3.32 can be substituted into 3.38 to obtain Laplace's equation.

$$\nabla^2 \phi(x, y) = 0 \quad (3.39)$$

3.6 Boundary Conditions in the Transverse Plane

In the transverse plane, the voltage must be continuous at the boundary between two layers (for example between layers 1 and 2), and the normal component of the \mathbf{E} field must satisfy

$$\hat{n} \cdot \left[\left(\epsilon_1 - j \frac{\sigma_1}{\omega} \right) \mathbf{E}_1 - \left(\epsilon_2 - j \frac{\sigma_2}{\omega} \right) \mathbf{E}_2 \right] = 0 \quad (3.40)$$

where \hat{n} is a unit vector normal to the boundary, ϵ_n is the permittivity of layer n , $j = \sqrt{-1}$, σ_n is the conductivity of layer n , ω is the angular (radian) excitation frequency, and \mathbf{E}_n is the electric field in layer n . For the transverse plane, \hat{y} is normal to the layer boundaries, so Equation 3.40 reduces to

$$\left(\epsilon_1 - j \frac{\sigma_1}{\omega} \right) E_{1y} = \left(\epsilon_2 - j \frac{\sigma_2}{\omega} \right) E_{2y} \quad (3.41)$$

where E_{ny} is the y component of the electric field in layer n .

Since this relationship is frequency dependent, the real part of the equation will dominate at large frequencies, while the imaginary part will dominate at low frequencies. The high frequency behavior of Equation 3.41 can be demonstrated by considering the limit as ω becomes large ($\omega \rightarrow \infty$); then, Equation 3.41 reduces to

$$\epsilon_1 E_{1y} = \epsilon_2 E_{2y} \quad (3.42)$$

This result is identical to the case with no conductivity present on either side of the boundary. By applying this high frequency condition at each boundary, the cell will appear to contain only pure dielectric material in each layer and we can solve for the potential distribution and, eventually, the capacitance for this ideal case. Thus, the high frequency boundary conditions should lead to the capacitive elements of the model.

The low frequency behavior of Equation 3.41 can be illustrated by multiplying each side by ω and taking the limit as $\omega \rightarrow 0$ to obtain, for example

$$\sigma_1 E_{1y} = \sigma_2 E_{2y} \quad (3.43)$$

If only one side of the boundary possesses conductivity (for example, layer 1), the above equation simplifies to $E_{1y} = 0$. This low frequency boundary condition permits the material to be treated as a conductor. Solving for the potential distribution with this boundary condition will eventually provide the resistance of the material in this ideal case. Since the sensor coating layer (layer 4) is surrounded by materials with $\sigma = 0$ (air and insulator), this low frequency boundary conditions can be enforced on layer 4 to solve for the potential distribution and, eventually, the resistance through this layer in the ideal case.

Within the cell, the conductivity of the substrate (layer 1) is much greater than the conductivity of the sensor coating (layer 4). This situation implies that the low frequency boundary condition can apply to the substrate boundary at frequencies where the high frequency boundary conditions still apply to the sensor coating layer. An angular frequency (ω_s) can be defined to signify the point where the substrate transitions from a conductor to a dielectric (the point where the real part equals the imaginary part on the left hand side of Equation 3.41). This transition occurs when

$$\omega_s = \frac{\sigma_1}{\epsilon_1} \quad (3.44)$$

By restricting the model to frequencies far below this point, the substrate can be treated as a good conductor to further simplify the model.

For example, if the conductivity of the substrate is 0.2 U/cm and the relative permittivity is 11.9, the transition frequency is

$$\omega_s = \frac{0.2}{11.9\epsilon_o} \quad (3.45)$$

where $\epsilon_o = 10^{-11}/36\pi$ F/cm is the permittivity of free space. Thus, the radian transition frequency is

$$\omega_s \approx 1.9 \cdot 10^{11} \text{ rad/sec} \quad (3.46)$$

The corresponding transition frequency (f_s) is

$$f_s = \frac{\omega_s}{2\pi} = 30 \text{ GHz} \quad (3.47)$$

This parameter represents the frequency where the substrate layer no longer acts as a good conductor. Therefore, if the operating frequency is much less than f_s , the substrate remains a good conductor (note: Kraus [13:446] defines a good conductor as $100\omega\epsilon < \sigma$). For example, an interdigitated electrode structure 0.4 cm long, having a substrate with $\sigma_1 = 0.2$ U/cm and $\epsilon_{r1} = 11.9$, will have $f_s \approx 100 \cdot f_L$. Thus, the substrate behaves as a good conductor for the frequency range ($0 < f < f_L$). By restricting the model of the interdigitated electrode structure to frequencies below the transition frequency of the substrate, the ground plane appears to be just below layer 2 and the model for the interdigital sensor structure simplifies to that shown in Figure 3.2.

If a semiconductor substrate (silicon) is used, a depletion layer capacitance must also be considered [16:192-194]. This capacitance is dependent on the voltage bias to the metal-insulator-semiconductor contact and adds a significant complexity to the model calculations. This additional capacitance introduces a variable model element (variable depending on the potential of each electrode), which is not considered in this thesis. The simplified model depicted in Figure 3.2 can still

be used for a semiconductor substrate, if a suitable ground plane is introduced between layers 1 and 2.

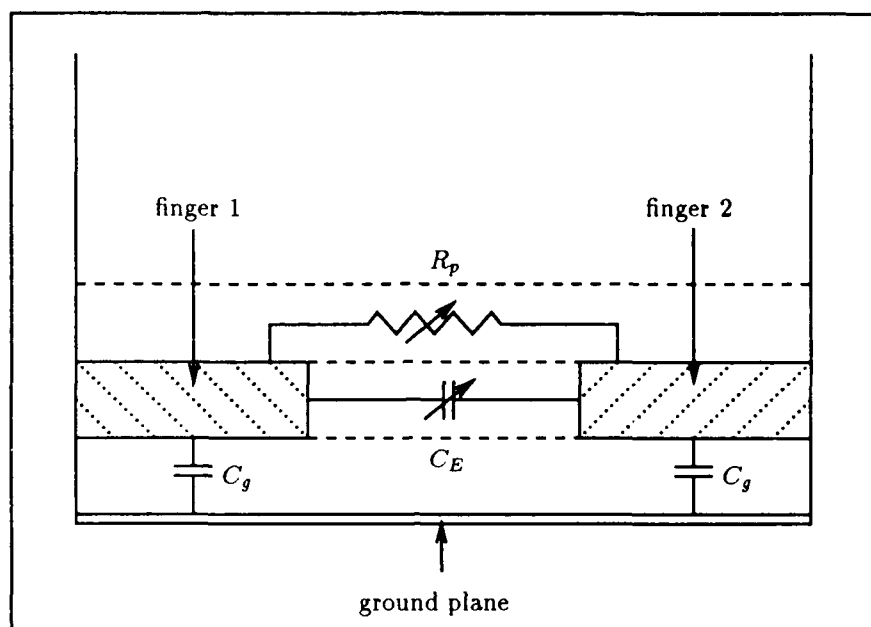


Figure 3.2. Simplified model for the interdigitated electrode sensor structure

The sensor coating (layer 4) has a much smaller conductivity value than the substrate. Therefore, throughout the operational frequency range considered herein ($0 < f < f_L \ll f_s$), both small and large ω behaviors will be observed at the boundaries of layer 4. As discussed for the substrate, there is a characteristic frequency associated with the transition of layer 4 from a conductor to a lossy dielectric. Using the condition where $\sigma_4 = \omega_p \epsilon_4 \epsilon_0$, a frequency (ω_p) can be defined as the angular frequency where the polymer transitions from a conductor to a lossy dielectric.

For the sensor coating used in the CHEMFET, $\sigma_4 = 10^{-8}$ U/cm and $\epsilon_4 = 650\epsilon_0$, and

$$\omega_p = \frac{\sigma_4}{\epsilon_4} = \frac{10^{-8}}{650\epsilon_0} = 174 \text{ rad/sec} \quad (3.48)$$

The corresponding ordinary frequency in hertz (f_p) is

$$f_p = \frac{\omega_p}{2\pi} = 27.7 \text{ Hz} \quad (3.49)$$

Thus, for higher frequencies ($f_p \ll f \ll f_L \ll f_s$), the sensor coating is a lossy dielectric. We can solve for the potential and the capacitive elements of Figure 3.2 for the ideal case of a pure dielectric material in each layer by enforcing the following high frequency boundary conditions on the potential, according to the development of Equations 3.41 and 3.42:

$$\epsilon_2 E_{2y} = \epsilon_3 E_{3y} \quad (3.50)$$

$$\epsilon_3 E_{3y} = \epsilon_4 E_{4y} \quad (3.51)$$

$$\epsilon_4 E_{4y} = \epsilon_5 E_{5y} \quad (3.52)$$

with the ground plane appearing below layer 2.

Similarly, for low frequencies ($0 \leq f \ll f_p$), we can solve for the potential in the conductive layer 4 and model it by a lumped resistive element, by enforcing the following low frequency boundary conditions on the potential as in Equation 3.43:

$$E_{4y} = 0 \quad (3.53)$$

3.7 Analysis Summary

In summary, to find the electrical parameters of interest, we must solve for the potential distribution in the transverse plane. This potential function is periodic and incorporates just four material layers (the ground plane appears above layer 1 since the substrate is a good conductor for the frequency range of interest). The resulting problem diagram is shown in Figure 3.3.

In this diagram, d is the insulator thickness, h is the electrode height, l is the combined height of the electrode and sensor coating layer, while s is the electrode separation. These quantities are normalized to the width of the electrode and are, hence, nondimensional quantities. V_1 and V_2 represent the potential on the left and right electrode, respectively. Within each layer, the

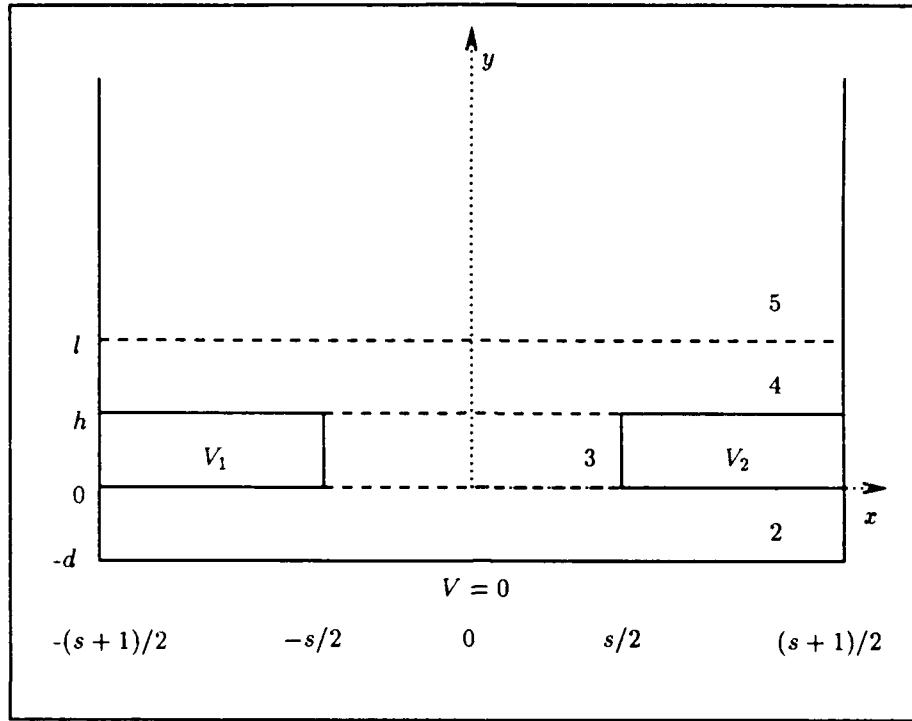


Figure 3.3. Problem diagram for model elements

potential must satisfy Laplace's equation. In addition, the potential above layer 5 must be bounded at infinity. Using the boundary data shown in the diagram, the potential must then satisfy the following conditions:

$$\nabla^2 \phi_k(x, y) = 0 \quad \text{for } k = 2, 3, 4, 5 \quad (3.54)$$

$$\frac{\partial \phi_k}{\partial x}(\pm \frac{s+1}{2}, y) = 0 \quad \text{for } k = 2, 4, 5 \quad (3.55)$$

$$\phi_2(x, -d) = 0 \quad \text{for } |x| \leq \frac{s+1}{2} \quad (3.56)$$

$$\lim_{y \rightarrow \infty} |\phi_5(x, y)| < \infty \quad \text{for } |x| < \frac{s+1}{2} \quad (3.57)$$

$$\phi_2(x, 0) = V_1 \quad \text{for } -\frac{s+1}{2} < x < -\frac{s}{2} \quad (3.58)$$

$$\phi_4(x, h) = V_1 \quad \text{for } -\frac{s+1}{2} < x < -\frac{s}{2} \quad (3.59)$$

$$\phi_2(x, 0) = V_2 \quad \text{for } \frac{s}{2} < x < \frac{s+1}{2} \quad (3.60)$$

$$\phi_4(x, h) = V_2 \quad \text{for } \frac{s}{2} < x < \frac{s+1}{2} \quad (3.61)$$

$$\phi_3(-\frac{s}{2}, y) = V_1 \quad \text{for } 0 \leq y \leq h \quad (3.62)$$

$$\phi_3(\frac{s}{2}, y) = V_2 \quad \text{for } 0 \leq y \leq h \quad (3.63)$$

In addition, the voltage must satisfy the boundary conditions at the interfaces between the layers.

First, the potential is continuous across layers:

$$\phi_2(x, 0) = \phi_3(x, 0) \quad \text{for } |x| < \frac{s}{2} \quad (3.64)$$

$$\phi_3(x, h) = \phi_4(x, h) \quad \text{for } |x| < \frac{s}{2} \quad (3.65)$$

$$\phi_4(x, l) = \phi_5(x, l) \quad \text{for } |x| < \frac{s+1}{2} \quad (3.66)$$

Also, the electric field normal to each interface must satisfy equations analogous to Equation 3.41.

To determine the capacitive elements, we solve for the potential distribution using the high frequency boundary conditions of the normal component of the electric field:

$$\epsilon_2 E_{2y} = \epsilon_3 E_{3y} \quad \text{for } |x| < \frac{s}{2} \text{ and } y = 0 \quad (3.67)$$

$$\epsilon_3 E_{3y} = \epsilon_4 E_{4y} \quad \text{for } |x| < \frac{s}{2} \text{ and } y = h \quad (3.68)$$

$$\epsilon_4 E_{4y} = \epsilon_5 E_{5y} \quad \text{for } |x| < \frac{s+1}{2} \text{ and } y = l \quad (3.69)$$

Since $E_y = -\partial\phi/\partial y$ in each of the layers, these equations yield the following conditions on the potential in each of the layers:

$$\frac{\partial\phi_2}{\partial y}(x, 0) = \frac{\partial\phi_3}{\partial y}(x, 0) \quad \text{for } |x| < \frac{s}{2} \quad (3.70)$$

$$\frac{\partial\phi_3}{\partial y}(x, h) = \frac{\partial\phi_4}{\partial y}(x, h) \quad \text{for } |x| < \frac{s}{2} \quad (3.71)$$

$$\frac{\partial\phi_4}{\partial y}(x, l) = \frac{\partial\phi_5}{\partial y}(x, l) \quad \text{for } |x| < \frac{s+1}{2} \quad (3.72)$$

To determine the resistive element, we solve only for the potential distribution in layer 4, using the low frequency boundary conditions of the normal component of the electric field, Equation 3.43. From Figure 3.3, with $V_1 = +1/2$ and $V_2 = -1/2$, the potential distribution must satisfy the following conditions:

$$\nabla^2 \phi_4(x, y) = 0 \quad (3.73)$$

$$\phi_4(x, h) = -\frac{1}{2} \quad \text{for } -\frac{s+1}{2} < x < -\frac{s}{2} \quad (3.74)$$

$$\phi_4(x, h) = \frac{1}{2} \quad \text{for } \frac{s}{2} < x < \frac{s+1}{2} \quad (3.75)$$

$$\frac{\partial \phi_4}{\partial x} \left(\pm \frac{s+1}{2}, y \right) = 0 \quad \text{for } h \leq y \leq l \quad (3.76)$$

The low frequency boundary conditions of the normal component of the electric field are

$$E_y = 0 \quad \text{for } |x| < \frac{s}{2}, \text{ and } y = h \quad (3.77)$$

$$E_y = 0 \quad \text{for } |x| < \frac{s+1}{2}, \text{ and } y = l \quad (3.78)$$

Since $E_y = -\partial \phi_4 / \partial y$, these equations transform into the following conditions on the potential in layer 4:

$$\frac{\partial \phi_4}{\partial y}(x, h) = 0 \quad \text{for } |x| < \frac{s}{2} \quad (3.79)$$

$$\frac{\partial \phi_4}{\partial y}(x, l) = 0 \quad \text{for } |x| < \frac{s+1}{2} \quad (3.80)$$

IV. Capacitance Solution

To determine the capacitive elements of the model, we solve Laplace's equation for the potential distribution within the periodic cell, using the boundary conditions corresponding to the large frequency limit. First, the potential functions of each layer are found which satisfy the partial differential equation and boundary conditions at $x = \pm(s+1)/2$ or $x = \pm s/2$, as appropriate. These functions contain constants, which are determined by enforcing the boundary conditions at the interfaces between the layers. The electric field is then determined from the gradient of the potential, and the charge is found using Gauss' law. The capacitance values are found directly from the charge using $Q = CV$, where Q is charge, C is the capacitance of interest, and V is the known potential. A diagram depicting the simplified periodic cell and the notation is shown in Figure 4.1.

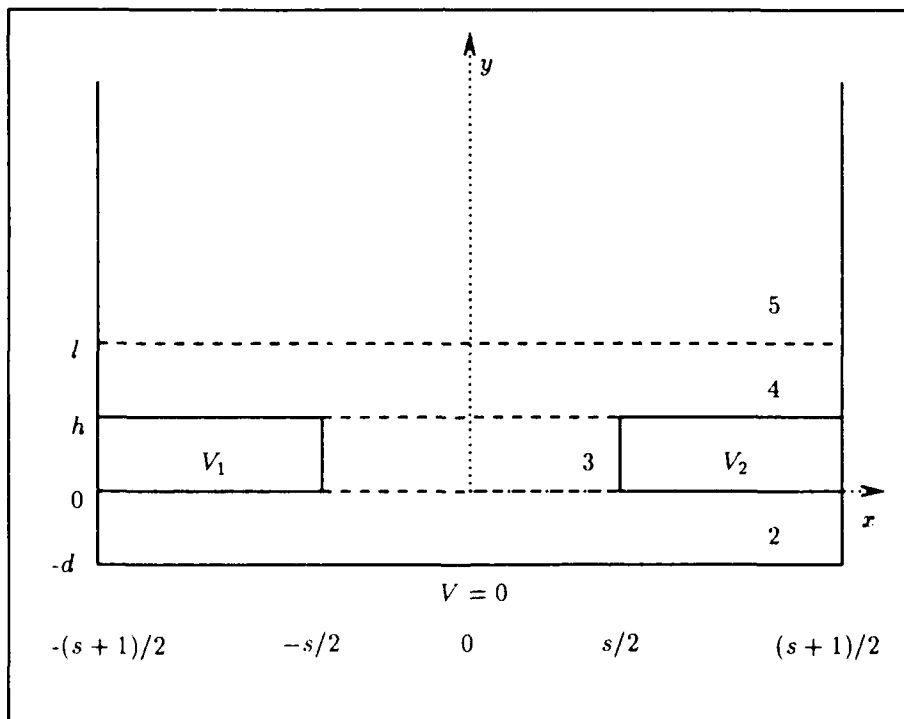


Figure 4.1. Problem diagram for capacitive solution

4.1 Potential in Each Layer

The potential function in each region was determined using the separation of variables technique with Laplace's equation in the transverse (x - y) plane. Eigenfunctions of the independent variable x are needed to match the potential and normal electric field across layer interfaces. Presented here is a summary of the solution, which is detailed in Appendix A.

4.1.1 Potential Functions Using the separation of variables technique, we obtain the potential ϕ_k in layer k for $k = 2, 3, 4, 5$ as functions of the impressed voltages, V_1 and V_2 , and all cell parameters. These potential functions are:

$$\phi_2(x, y) = a_0(y + d) + \sum_{n=1}^{\infty} a_n \sinh[\lambda_2(y + d)] \psi_n^2(x) \quad (4.1)$$

$$\phi_3(x, y) = v_3(x) + \sum_{n=1}^{\infty} \left\{ b_n \cosh \left[\lambda_3 \left(y - \frac{h}{2} \right) \right] + c_n \sinh \left[\lambda_3 \left(y - \frac{h}{2} \right) \right] \right\} \psi_n^3(x) \quad (4.2)$$

$$\phi_4(x, y) = d_0 + \sum_{n=1}^{\infty} d_n \mathcal{F}_n^4(y) \psi_n^4(x) \quad (4.3)$$

$$\phi_5(x, y) = d_0 + \sum_{n=1}^{\infty} d_n \exp(-\lambda_5 y) \psi_n^5(x) \quad (4.4)$$

where

$$\lambda_k = \frac{n\pi}{s+1} \quad \text{for } k = 2, 4, 5 \quad (4.5)$$

$$\lambda_3 = \frac{n\pi}{s} \quad (4.6)$$

$$\psi_n^k(x) = \cos \left[n\pi \left(\frac{x}{s+1} + \frac{1}{2} \right) \right] \quad \text{for } k = 2, 4, 5 \quad (4.7)$$

$$\psi_n^3(x) = \sin \left[n\pi \left(\frac{x}{s} + \frac{1}{2} \right) \right] \quad (4.8)$$

$$v_3(x) = \left(\frac{V_2 - V_1}{s} \right) x + \frac{V_2 + V_1}{2} \quad (4.9)$$

$$\mathcal{F}_n^4(y) = \exp(-\lambda_4 l) \left\{ \cosh[\lambda_4(l - y)] + \frac{\epsilon_5}{\epsilon_4} \sinh[\lambda_4(l - y)] \right\} \quad (4.10)$$

and a_n , b_n , c_n , and d_n are constants used to satisfy the boundary conditions. The superscript in $\psi_n^k(y)$ denotes the layer of interest, instead of the normal "power" interpretation.

4.1.2 *Applying Boundary Conditions to Determine the Coefficients.* To determine the unknown constants, we have the boundary conditions to enforce at the interface between layers 2 and 3 and that between layers 3 and 4. The potential is continuous across each layer (continuity condition), while the y component of the electric field must satisfy the capacitive boundary conditions imposed by Equations 3.70, 3.71, and 3.72 (jump condition). Therefore, we use the orthogonal properties of the trigonometric functions to "sift" certain coefficients out of the infinite series. This will allow us to develop a system of equations which we can solve to determine the four sets of coefficients.

For the continuity condition, we sift with the outer (layers 2 and 4) eigenfunction since the boundary data is known across the entire width of the periodic cell. However, we sift with the inner (layer 3) eigenfunction for the jump condition, since it is restricted to $|x| < \frac{d}{2}$. From the solution detailed in Appendix A, the following equations must be solved to find the coefficients a_n , b_n , c_n , and d_n :

$$a_0 d(s+1) - \sum_{n=1}^{\infty} \frac{2s}{n\pi} b_n \Phi_n^c [1 - (-1)^n] + d_0(s+1) = (s+1)(V_1 + V_2) \quad (4.11)$$

$$a_0 d(s+1) + \sum_{n=1}^{\infty} \frac{2s}{n\pi} c_n \Psi_n^c [1 - (-1)^n] - d_0(s+1) = 0 \quad (4.12)$$

$$a_m \Theta_m^c \frac{s+1}{2} - 2 \sum_{n=1}^{\infty} b_n \Phi_n^c I_{mn}^3 + d_m \mathcal{F}_m^4(h) \frac{s+1}{2} = 2\mathcal{I}_m \quad (4.13)$$

$$a_m \Theta_m^c \frac{s+1}{2} + 2 \sum_{n=1}^{\infty} c_n \Psi_n^c I_{mn}^3 - d_m \mathcal{F}_m^4(h) \frac{s+1}{2} = 0 \quad (4.14)$$

$$\frac{\epsilon_2 s}{m\pi} [1 - (-1)^m] a_0 + \sum_{n=1}^{\infty} \frac{\epsilon_2 n\pi}{s+1} a_n \Gamma_n^c I_{nm}^3 + \epsilon_3 m\pi b_m \Psi_m^c + \sum_{n=1}^{\infty} \frac{\epsilon_4 n\pi}{s+1} d_n \mathcal{H}_n^4(h) I_{nm}^3 = 0 \quad (4.15)$$

$$\frac{\epsilon_2 s}{m\pi} [1 - (-1)^m] a_0 + \sum_{n=1}^{\infty} \frac{\epsilon_2 n\pi}{s+1} a_n \Gamma_n^c I_{nm}^3 - \epsilon_3 m\pi c_m \Phi_m^c - \sum_{n=1}^{\infty} \frac{\epsilon_4 n\pi}{s+1} d_n \mathcal{H}_n^4(h) I_{nm}^3 = 0 \quad (4.16)$$

where m is a positive integer and

$$\Theta_m^c = \sinh\left(\frac{m\pi d}{s+1}\right) \quad (4.17)$$

$$\Gamma_n^c = \cosh \left(\frac{m\pi d}{s+1} \right) \quad (4.18)$$

$$\mathcal{F}_m^4(h) = \exp(-\lambda_m l) \left\{ \cosh[\lambda_m(l-h)] + \frac{\epsilon_5}{\epsilon_4} \sinh[\lambda_m(l-h)] \right\} \quad (4.19)$$

$$\mathcal{H}_n^4(h) = \exp(-\lambda_n l) \left\{ \sinh[\lambda_n(l-h)] + \frac{\epsilon_5}{\epsilon_4} \cosh[\lambda_n(l-h)] \right\} \quad (4.20)$$

$$\Phi_n^c = \cosh \left(\frac{n\pi h}{2s} \right) \quad (4.21)$$

$$\Psi_n^c = \sinh \left(\frac{n\pi h}{2s} \right) \quad (4.22)$$

$$\lambda_n = \frac{n\pi}{s+1} \quad (4.23)$$

$$\mathcal{I}_m = \langle V_1, \psi_m^2 \rangle^- + \langle V_2, \psi_m^2 \rangle^+ + I_m^1 + I_m^2 \quad (4.24)$$

$$\langle V_1, \psi_m^2 \rangle^- = \frac{V_1(s+1)}{m\pi} \sin \left(\frac{m\pi}{2s+2} \right) \quad (4.25)$$

$$\langle V_2, \psi_m^2 \rangle^+ = (-1)^m \frac{V_2(s+1)}{m\pi} \sin \left(\frac{m\pi}{2s+2} \right) \quad (4.26)$$

$$I_m^1 = \frac{(V_2 - V_1)(s+1)^2}{sm^2\pi^2} \cos \left(\frac{m\pi}{2s+2} \right) [(-1)^m - 1] \\ + \frac{(V_2 - V_1)(s+1)}{2m\pi} \sin \left(\frac{m\pi}{2s+2} \right) [1 - (-1)^m] \quad (4.27)$$

$$I_m^2 = -[1 + (-1)^m] \frac{(V_2 + V_1)(s+1)}{2m\pi} \sin \left(\frac{m\pi}{2s+2} \right) \quad (4.28)$$

$$I_{mn}^3 = \begin{cases} -\frac{s}{2} \sin \left(\frac{m\pi}{2s+2} \right) & \text{for } n = \frac{ms}{s+1} \\ \frac{sn}{\pi[n^2 - (\frac{ms}{s+1})^2]} \cos \left(\frac{m\pi}{2s+2} \right) [1 - (-1)^{n+m}] & \text{for } n \neq \frac{ms}{s+1} \end{cases} \quad (4.29)$$

4.2 Charge Calculations

To find the charge on either microstrip, we integrate the normal electric flux density around a closed contour enclosing the microstrip. The result of the charge calculations is simply presented here, while the calculations are detailed in Appendix B. The charge on either microstrip is

$$Q = \frac{1}{2} \epsilon_2 a_0 (s+1) + \epsilon_2 \sum_{n=1}^{\infty} a_n \sin \left(\frac{n\pi}{2} \right) \Gamma_n^c + \frac{h\epsilon_3}{s} (V_1 - V_2) \\ - 2\epsilon_3 \sum_{n=1}^{\infty} \cos \left(\frac{n\pi}{2} \right) b_n \sinh \left(\frac{n\pi h}{2s} \right) + \epsilon_4 \sum_{n=1}^{\infty} d_n \sin \left(\frac{n\pi}{2} \right) \mathcal{H}_n^4(h) \quad (4.30)$$

4.3 Evaluation of the Capacitive Elements

To solve for the capacitive elements, we utilize Weeks' method [17] to solve for the elements one at a time. The capacitance to ground element, C_g , is found by setting both electrodes to the same potential ($V_1 = V_2$). The charge on either conductor can then only be associated with a capacitance to ground, since an electric flux cannot exist between the two conductors when they are at the same potential. Therefore, if we solve for the potential and charge for the case of $V_1 = V_2 = 1$ volt, then

$$C_g = Q_{(V_1=V_2=1)} \quad (4.31)$$

where $Q_{(V_1=V_2=1)}$ is the charge for the case of $V_1 = V_2 = 1$ volt.

To solve for C_E , one of the electrodes is grounded (for example, $V_1 = 1$ volt and $V_2 = 0$ volts). Now the total capacitance to ground (C_T), from the ungrounded electrode, is the parallel combination of C_g and C_E . Since capacitances in parallel add, then

$$C_E = C_T - C_g \quad (4.32)$$

$$= Q_{(V_1=1, V_2=0)} - Q_{(V_1=V_2=1)} \quad (4.33)$$

where $Q_{(V_1=1, V_2=0)}$ is the charge for the case of $V_1 = 1$ volt and $V_2 = 0$ volts.

This method requires the potential to be solved for two separate cases. Therefore, it can be advantageous to use symmetry within the periodic cell to reduce the computational requirements and solve for the potential only once. Hence, it is beneficial to consider symmetry within the periodic cell.

4.3.1 Cell Symmetry and the Eigenfunctions. To investigate possible symmetry within the periodic cell, it is necessary to further analyze the eigenfunctions in each layer of the cell. From Equation A.16, the eigenfunctions in layers 2, 4, and 5 are

$$\Psi_n(x) = A_n \cos \left[n\pi \left(\frac{x}{s+1} + \frac{1}{2} \right) \right] \quad (4.34)$$

Since

$$\cos(\alpha + \beta) = \cos(\alpha) \cos(\beta) - \sin(\alpha) \sin(\beta) \quad (4.35)$$

we may write

$$\Psi_n(x) = A_n \cos \left(\frac{n\pi x}{s+1} \right) \cos \left(\frac{n\pi}{2} \right) - A_n \sin \left(\frac{n\pi x}{s+1} \right) \sin \left(\frac{n\pi}{2} \right) \quad (4.36)$$

$$\Psi_n(x) = \Psi_n^{even}(x) - \Psi_n^{odd}(x) \quad (4.37)$$

where

$$\Psi_n^{even}(x) = A_n \cos \left(\frac{n\pi x}{s+1} \right) \cos \left(\frac{n\pi}{2} \right) \quad (4.38)$$

$$\Psi_n^{odd}(x) = A_n \sin \left(\frac{n\pi x}{s+1} \right) \sin \left(\frac{n\pi}{2} \right) \quad (4.39)$$

Hence, the original eigenfunction has components which have odd and even symmetry with respect to $x = 0$. If the applied voltages are equal, then the potential must be symmetric with respect to $x = 0$, so that

$$\Psi_n(x) = \Psi_n^{even}(x) \quad (4.40)$$

and

$$\Psi_n^{odd} = 0 \quad (4.41)$$

Thus, all the coefficients of the odd-indexed terms must be zero when the potential has even symmetry with respect to $x = 0$, due to the factor $\sin(n\pi/2)$ in Ψ_n^{odd} . Similarly with odd symmetry ($V_1 = -V_2$)

$$\Psi_n(x) = -\Psi_n^{odd}(x) \quad (4.42)$$

and

$$\Psi_n^{even}(x) = 0 \quad (4.43)$$

Hence, all the coefficients of the even-indexed terms must be zero when the potential has odd symmetry with respect to $x = 0$, due to the factor $\cos(n\pi/2)$ in Ψ_n^{even} .

For layer 3, from Equation A.50, the eigenfunction is

$$\Psi_n^3(x) = B_n \sin \left[n\pi \left(\frac{x}{s} + \frac{1}{2} \right) \right] \quad (4.44)$$

Now, employing the trigonometric identity

$$\sin(\alpha + \beta) = \sin(\alpha) \cos(\beta) + \cos(\alpha) \sin(\beta) \quad (4.45)$$

we have

$$\Psi_n^3(x) = B_n \sin \left(\frac{n\pi x}{s} \right) \cos \left(\frac{n\pi}{2} \right) + B_n \cos \left(\frac{n\pi x}{s} \right) \sin \left(\frac{n\pi}{2} \right) \quad (4.46)$$

$$= \Psi_n^{3odd}(x) + \Psi_n^{3even}(x) \quad (4.47)$$

where

$$\Psi_n^{3odd}(x) = B_n \sin \left(\frac{n\pi x}{s} \right) \cos \left(\frac{n\pi}{2} \right) \quad (4.48)$$

$$\Psi_n^{3even}(x) = B_n \cos \left(\frac{n\pi x}{s} \right) \sin \left(\frac{n\pi}{2} \right) \quad (4.49)$$

With even symmetry ($V_1 = V_2$)

$$\Psi_n^3(x) = \Psi_n^{3even}(x) \quad (4.50)$$

and

$$\Psi_n^{3odd} = 0 \quad (4.51)$$

Thus, all the coefficients of the even-indexed terms in layer 3 must be zero for even symmetry. For odd symmetry ($V_1 = -V_2$)

$$\Psi_n^3(x) = \Psi_n^{3odd}(x) \quad (4.52)$$

and

$$\Psi_n^{3even}(x) = 0 \quad (4.53)$$

Hence, all the coefficients of the odd-indexed terms in layer 3 must be zero for odd symmetry.

4.3.2 Symmetry and the Charge Function. We can use the results of the previous section to simplify the charge expression. From Equation 4.30

$$\begin{aligned} Q = & \frac{1}{2}\epsilon_2 a_0(s+1) + \epsilon_2 \sum_{n=1}^{\infty} a_n \sin\left(\frac{n\pi}{2}\right) \cosh\left(\frac{n\pi d}{s+1}\right) + \frac{h\epsilon_3}{s}(V_1 - V_2) \\ & - 2\epsilon_3 \sum_{n=1}^{\infty} \cos\left(\frac{n\pi}{2}\right) b_n \sinh\left(\frac{n\pi h}{2s}\right) + \epsilon_4 \sum_{n=1}^{\infty} d_n \sin\left(\frac{n\pi}{2}\right) \mathcal{H}_n^4(h) \end{aligned} \quad (4.54)$$

$$= Q1 + Q2 + Q3 + Q4 + Q5 \quad (4.55)$$

where each term in order was assigned a corresponding label. With even symmetry ($V_1 = V_2$), the odd terms in layers 2 and 4 are zero ($a_n = d_n = 0$ for odd n) and the even terms in layer 3 are zero ($b_n = c_n = 0$ for even n). Hence,

$$Q2 = Q3 = Q4 = Q5 = 0 \quad (4.56)$$

and

$$Q^{even} = Q1 = \frac{1}{2}\epsilon_2 a_0(s+1) \quad (4.57)$$

For odd symmetry ($V_1 = -V_2$), the even terms in layer 2 are zero; thus, $a_0 = 0$ and

$$Q^{odd} = Q2 + Q3 + Q4 + Q5 \quad (4.58)$$

These symmetry considerations are important because they simplify the calculations required for the capacitive elements of the model. To determine the C_g element, both electrodes are fixed to the same potential (for example $V_1 = V_2 = 1$ volt), while for the C_E element, one electrode is grounded (for example $V_1 = 1$ volt with $V_2 = 0$). However, the non-symmetric case ($V_1 = 1$ and $V_2 = 0$) is equivalent to the superposition of even symmetry ($V_1 = V_2 = .5$) and odd symmetry ($V_1 = -V_2 = .5$). Thus, using cell symmetry, we have a method to extract the even symmetry charge using the solution to the potential in this non-symmetric case.

Therefore, we only have to solve for the potential coefficients once (in the non-symmetric case) to determine both capacitive elements. Without these symmetry arguments, the potential coefficients would have to be determined separately for each case.

4.3.3 Capacitance to Ground: C_g . With even symmetry in the transverse plane, both electrodes have the same potential, and the charge on either conductor will only be associated with a capacitance to ground. Hence this capacitance to ground C_g can be found from the relationship

$$C_g = \frac{Q^{even}}{V} \quad (4.59)$$

where Q^{even} is the charge from the even symmetry case and V is the potential on the electrode. The potential coefficients are calculated using $V_1 = 1$ and $V_2 = 0$. Since this situation is equivalent to the superposition of an even symmetry case ($V_1 = V_2 = .5$) and an odd symmetry case ($V_1 = -V_2 = .5$), we use $V = .5$ in the formula corresponding to the value in the even symmetry case. Thus

$$C_g = 2Q^{even} = \epsilon_2 a_0 (s + 1) \quad (4.60)$$

4.3.4 Capacitance Between Electrodes: C_E . With $V_1 = 1$ and $V_2 = 0$, the total capacitance to ground will be the parallel combination of C_E and C_g . Since capacitances in parallel add, the total capacitance, C_T , is

$$C_T = C_E + C_g = \frac{Q}{V} \quad (4.61)$$

where Q is the total charge and V is the potential on the electrode. Hence, with $V = 1$

$$C_E = C_T - C_g = Q - 2Q^{even} = Q^{odd} - Q^{even} \quad (4.62)$$

or

$$\begin{aligned} C_E = & \epsilon_2 \sum_{n=1}^{\infty} a_n \sin\left(\frac{n\pi}{2}\right) \Gamma_n^c + \frac{h\epsilon_3}{s} (V_1 - V_2) - 2\epsilon_3 \sum_{n=1}^{\infty} \cos\left(\frac{n\pi}{2}\right) b_n \sinh\left(\frac{n\pi h}{2s}\right) \\ & + \epsilon_4 \sum_{n=1}^{\infty} d_n \sin\left(\frac{n\pi}{2}\right) \mathcal{H}_n^4(h) - \frac{1}{2}\epsilon_2 a_0(s+1) \end{aligned} \quad (4.63)$$

4.4 Estimating the Potential Coefficients

By truncating the infinite series of Equations 4.11-4.16 at N terms (where N is an integer), we can estimate the first N terms of each set of potential coefficients. Therefore we can determine a_0, a_1, \dots, a_{N-1} , b_1, b_2, \dots, b_N , c_1, c_2, \dots, c_N , and d_0, d_1, \dots, d_{N-1} by solving a system of $4N$ Equations. The equivalent matrix equation formulation is

$$\begin{bmatrix} a1_m & b1_{mn} & 0 & d1_m \\ a1_m & 0 & c1_{mn} & -d1_m \\ a2_{mn} & b2_m & 0 & d2_{mn} \\ a2_{mn} & 0 & c2_m & -d2_{mn} \end{bmatrix} \begin{bmatrix} a_n \\ b_n \\ c_n \\ d_n \end{bmatrix} = \begin{bmatrix} F_m \\ 0 \\ 0 \\ 0 \end{bmatrix} \quad (4.64)$$

where

$$a1_m = \begin{cases} d(s+1) & \text{for } m = 0 \\ \Theta_m^c \frac{s+1}{2} & \text{for } m \neq 0 \end{cases} \quad (4.65)$$

$$b1_{mn} = \begin{cases} -\frac{2s}{n\pi} \Phi_n^c [1 - (-1)^n] & \text{for } m = 0 \\ -2\Phi_n^c I_{mn}^3 & \text{for } m \neq 0 \end{cases} \quad (4.66)$$

$$c1_{mn} = \begin{cases} \frac{2s}{n\pi} \Psi_n^c [1 - (-1)^n] & \text{for } m = 0 \\ 2\Psi_n^c I_{mn}^3 & \text{for } m \neq 0 \end{cases} \quad (4.67)$$

$$d1_m = \begin{cases} s+1 & \text{for } m=0 \\ \mathcal{F}_m^4(h)^{\frac{s+1}{2}} & \text{for } m \neq 0 \end{cases} \quad (4.68)$$

$$a2_{mn} = \begin{cases} \frac{\epsilon_2 s}{m\pi} [1 - (-1)^m] & \text{for } n=0 \\ \frac{\epsilon_2 n\pi}{s+1} \Gamma_n^c f_{nm}^3 & \text{for } n \neq 0 \end{cases} \quad (4.69)$$

$$b2_m = \epsilon_3 m \pi \Psi_m^c \quad (4.70)$$

$$c2_m = -\epsilon_3 m \pi \Phi_m^c \quad (4.71)$$

$$d2_{mn} = \frac{\epsilon_4 n \pi}{s+1} \mathcal{H}_n^4 \quad (4.72)$$

$$F_m = \begin{cases} (s+1)(V_1 + V_2) & \text{for } m=0 \\ 2\mathcal{I}_m & \text{for } m \neq 0 \end{cases} \quad (4.73)$$

V. Resistive Solution

To determine the resistive element of the model, we solve Laplace's equation for the potential distribution within the conductive layer 4, using the boundary conditions associated with the low frequency limit. First, the layer is divided into three regions to match the boundary data. The potential functions in each region are then found, which satisfy the partial differential equation and the boundary conditions at $y = h$ and $y = l$. These functions contain unknown constants that are determined by enforcing boundary conditions at the interfaces between the regions. The electric field (\mathbf{E}) is determined from the gradient of the potential and the current density (\mathbf{J}) is found using $\mathbf{J} = \sigma \mathbf{E}$, where σ is the conductivity of the layer. The current through the layer is found by integrating the current density over a suitable contour, and the resistance is then determined using Ohm's law. The problem diagram is shown in Figure 5.1, in which the x axis has been translated by $-h$ to simplify the analysis. Thus, $0 \leq y \leq p$, where $p = l - h$.

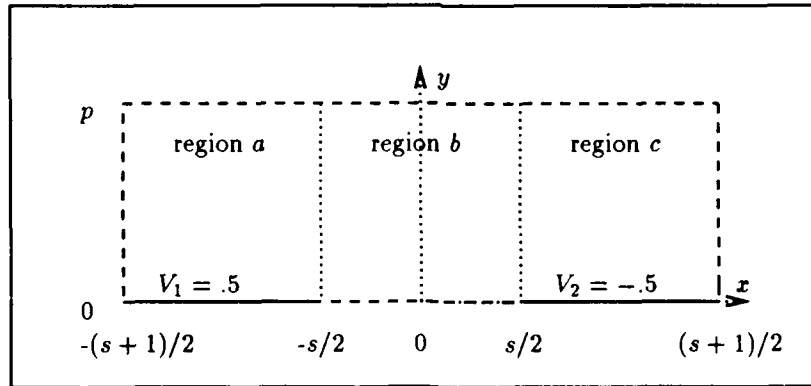


Figure 5.1. Diagram of resistive layer

5.1 Resistive Potential Functions

The resistive layer is divided into 3 regions (see Figure 5.1). Region a is the left region which is bounded by $-(s+1)/2 \leq x \leq -s/2$. Region b is the center region which is bounded by

$-s/2 \leq x \leq s/2$. Region *c* is the right region which is bounded by $s/2 \leq x \leq (s+1)/2$. In the resistive solution, we concentrate on the case of odd symmetry with respect to $x = 0$ ($V_1 = -V_2 = 1/2$), since the even symmetry case ($V_1 = V_2$) does not produce any electric flux between the two electrodes. Using the resistive boundary conditions and the separation of variables approach, a series form of the voltage potential is obtained, with eigenfunctions in the independent variable y , consisting of trigonometric functions, while the corresponding functions in x are hyperbolic functions. For simplification, the results are summarized here, while the complete solution is detailed in Appendix C (ϕ_k denotes the potential in region k , with $k = a, b$, or c). The potentials in the resistive solution are

$$\phi_a(x, y) = \frac{1}{2} + \sum_{n=1}^{\infty} e_n \cosh \left[\frac{(2n-1)\pi}{2p} \left(x + \frac{s+1}{2} \right) \right] \sin \left[\frac{(2n-1)\pi y}{2p} \right] \quad (5.1)$$

$$\phi_b(x, y) = f_0 + \sum_{n=1}^{\infty} g_n \sinh \left(\frac{n\pi x}{p} \right) \cos \left(\frac{n\pi y}{p} \right) \quad (5.2)$$

$$\phi_c(x, y) = -\phi_a(-x, y) \quad (5.3)$$

where e_n , f_0 , and g_n are constants used to satisfy the continuity of the potential and its x derivative, across the boundaries of the regions.

5.2 Applying Boundary Data Between Regions

The constants can be determined by enforcing the boundary conditions between the regions. Because of symmetry with respect to $x = 0$, either the left boundary (regions *a* and *b*) or the right boundary (regions *b* and *c*) produce the same system of equations to solve. At the boundary, the potential is continuous across the boundary (continuity condition) and the x component of the electric field is also continuous (jump condition) since the conductivity is identical on both sides of the boundary. This situation leads to two boundary equations with infinite series on each side of the

equations. However, orthogonality of the cosine functions can be used to reduce the two equations to only an infinite series involving the e_n coefficients. The resulting equations from Appendix C are

$$\sum_{n=1}^{\infty} e_n \left[\Gamma_n^r \frac{4}{(2n-1)\pi} + \frac{s}{\nu} \Theta_n^r \right] = -1 \quad (5.4)$$

$$\sum_{n=1}^{\infty} e_n \left\{ \frac{m\Phi_m^r}{\Psi_m^r} \frac{4(2n-1)}{\pi[(2n-1)^2 - 4m^2]} \Gamma_n^r + \frac{2(2n-1)^2}{\pi[(2n-1)^2 - 4m^2]} \Theta_n^r \right\} = 0 \quad (5.5)$$

where m is a positive integer and

$$\Gamma_n^r = \cosh \left[\frac{(2n-1)\pi}{4p} \right] \quad (5.6)$$

$$\Theta_n^r = \sinh \left[\frac{(2n-1)\pi}{4p} \right] \quad (5.7)$$

$$\Phi_m^r = \cosh \left(\frac{m\pi s}{2p} \right) \quad (5.8)$$

$$\Psi_m^r = \sinh \left(\frac{m\pi s}{2p} \right) \quad (5.9)$$

The superscript r notation denotes quantities used in the resistive solution. Once the e_n 's are determined, the g_m 's and f_0 can be found from the relationships

$$f_0 = \frac{1}{p} \sum_{n=1}^{\infty} e_n \Theta_n^r \quad (5.10)$$

$$g_m = -\frac{1}{\Psi_m^r} \sum_{n=1}^{\infty} e_n \Gamma_n^r \frac{4(2n-1)}{\pi[(2n-1)^2 - 4m^2]} \quad (5.11)$$

5.3 Resistance Calculation

To determine the resistance of layer 4, we calculate the current flowing through layer 4. From Ohm's law

$$V = IR \quad (5.12)$$

where V is the voltage potential, I is the current, and R is the resistance. Equivalently,

$$G = I/V \quad (5.13)$$

where $G = 1/R$, and G is the conductance of layer 4. The current density (\mathbf{J}) is related to the electric field (\mathbf{E}) by

$$\mathbf{J} = \sigma \mathbf{E} \quad (5.14)$$

where σ is the conductivity within layer 4. The total current can be determined by integrating the current density over a suitable contour, which encompasses all the current density. Referring to Figure 5.1, the current density in the x direction (J_x) is integrated along the y axis from $y = 0$ to $y = p$. From Equation 5.2, the potential in region b is

$$\phi_b(x, y) = f_0 x + \sum_{n=1}^{\infty} g_n \sinh\left(\frac{n\pi x}{p}\right) \cos\left(\frac{n\pi y}{p}\right) \quad (5.15)$$

Using the relationship

$$E_x = -\frac{\partial \phi}{\partial x} \quad (5.16)$$

we may write

$$E_x(x, y) = -f_0 - \sum_{n=1}^{\infty} \frac{n\pi}{p} g_n \cosh\left(\frac{n\pi x}{p}\right) \cos\left(\frac{n\pi y}{p}\right) \quad (5.17)$$

At $x = 0$, this reduces to

$$E_x(0, y) = -f_0 - \sum_{n=1}^{\infty} \frac{n\pi}{p} g_n \cos\left(\frac{n\pi y}{p}\right) \quad (5.18)$$

Using Equation 5.18 in Equation 5.14 yields the current density along the y axis, where $x = 0$.

Thus,

$$J_x(0, y) = -\sigma f_0 - \sigma \sum_{n=1}^{\infty} \frac{n\pi}{p} g_n \cos\left(\frac{n\pi y}{p}\right) \quad (5.19)$$

The current through layer 4 is, formally,

$$\begin{aligned}
 I &= \int_0^p J_x(0, y) dy \\
 &= \int_0^p \left[-\sigma f_0 - \sigma \sum_{n=1}^{\infty} \frac{n\pi}{p} g_n \cos\left(\frac{n\pi y}{p}\right) \right] dy \\
 &= -\sigma f_0 \int_0^p dy - \sigma \sum_{n=1}^{\infty} \frac{n\pi}{p} g_n \int_0^p \cos\left(\frac{n\pi y}{p}\right) dy \\
 &= -\sigma f_0 p - \sigma \sum_{n=1}^{\infty} \frac{n\pi}{p} g_n \left[\frac{p}{n\pi} \sin\left(\frac{n\pi y}{p}\right) \right]_0^p \\
 &= -\sigma f_0 p - \sigma \sum_{n=1}^{\infty} g_n \sin(n\pi) \\
 I &= -\sigma f_0 p
 \end{aligned} \tag{5.20}$$

Using Equation 5.20 in 5.13, with $V = 1$ volt, yields

$$G = -\sigma f_0 p \tag{5.21}$$

Equivalently,

$$R = (-\sigma f_0 p)^{-1} \tag{5.22}$$

5.4 Estimating the Coefficients

With the equations presented in the section 5.2, the unknown constants can now be estimated by truncating the infinite series in Equations 5.4 and 5.5 at an integer N . Converting the equations to matrix form yields

$$[M_{mn}][e_n] = [F_m] \tag{5.23}$$

where

$$M_{mn} = \begin{cases} \frac{4}{(2n-1)\pi} \Gamma_n^r + \frac{2}{p} \Theta_n^r & \text{for } m = 0 \\ \frac{m\Phi_m^r}{\Psi_m^r} \frac{4(2n-1)}{\pi[(2n-1)^2 - 4m^2]} \Gamma_n^r + \frac{2(2n-1)^2}{\pi[(2n-1)^2 - 4m^2]} \Theta_n^r & \text{for } m \neq 0 \end{cases} \tag{5.24}$$

$$F_m = \begin{cases} -1 & \text{for } m = 0 \\ 0 & \text{for } m \neq 0 \end{cases} \quad (5.25)$$

Hence we can approximate e_1, e_2, \dots, e_N by solving N equations ($m = 0, 1, 2, \dots, N - 1$), and thus obtain an $N \times N$ matrix. From the e_n terms, we can also estimate f_0 and the g_m terms using Equations 5.10 and 5.11.

VI. Numerical Results

Up to this point, the analysis and solutions have been general in nature, with dimensional and material values of the periodic cell unspecified. In this chapter, we use the expressions developed in previous chapters with particular values for the structure's dimensions and material properties. Specifically, we focus on cell dimensions and material aspects which are representative of the chemically-sensitive field-effect transistor (CHEMFET) [18]. Within this chapter, section 6.1 concentrates on the results of the capacitive solution, while section 6.2 focuses on the resistive solution.

In sections 6.1.1 and 6.1.2, the capacitive solution is illustrated by investigating the potential along the interfaces between layers and by observing constant voltage contour plots using special test data for the cell parameters. In section 6.1.3, graphs of the capacitive elements are presented using a baseline set of cell parameters, while varying individual parameters over a specific range.

In section 6.2.1, we illustrate the resistive solution by observing the potential along the lower border and a constant voltage contour plot created using special test values for the layer parameters. In section 6.2.2, graphs of the resistive elements are presented using the baseline values for the cell, while varying individual parameters over a specific range.

6.1 Results of the Capacitive Solution

A FORTRAN computer program was created to solve the truncated linear system of equations discussed in section 4.4, and thereby approximate the coefficients involved in the capacitive solution of the potential function. The program utilizes the IMSL gaussian elimination FORTRAN routine "LSARG" [7:11].

6.1.1 Potential Along the Boundaries. By truncating the series at N terms (where N is an integer), we are able to estimate the first N coefficients. For the capacitive solution, these

coefficients are: $a_0, a_1, \dots, a_{N-1}, b_1, b_2, \dots, b_N, c_1, c_2, \dots, c_N$, and d_0, d_1, \dots, d_{N-1} . As N becomes larger, the overall accuracy of the final sum will improve, but at the cost of increased computer processing time to solve the coefficients. A worthwhile objective is to use the fewest number of coefficients (smallest N) and yet achieve accurate results.

To select a suitable number of terms, N , the potentials along the lower boundary (between layers 2 and 3) and the upper boundary (between layers 3 and 4) are investigated with $N = 10, 20$, and 50 . Normalized data values used for the program are displayed in Table 6.1 (ϵ_{rk} is the relative permittivity or dielectric constant in layer k , and $\epsilon_k = \epsilon_{rk} \epsilon_0$ where ϵ_0 is the permittivity of free space). The values for the cell parameters were selected using the CHEMFET data as a guide and normalizing all cell dimension with respect to the electrode width. The results at the lower boundary are displayed in Figure 6.1, while the results at the upper boundary are shown in Figure 6.2.

Table 6.1. Normalized data used for boundary potentials (with no coating)

parameter	d	h	l	s	ϵ_{r2}	ϵ_{r3}	ϵ_{r4}	ϵ_{r5}
value	0.1	0.1	0.11	1	3.9	1	1	1

With $N = 50$, both Figures 6.1 and 6.2 show good agreement with Equations 3.58, 3.59, 3.60, and 3.61 for $V_1 = 1$ and $V_2 = 0$. There is some deviation at the edge of the left electrode, but this is expected due to the finite number of terms kept in the Fourier representation of the potential function. The potentials along the boundaries are non-linear due to the small insulator thickness (d). Figure 6.3 displays both the upper and lower boundary potential with various insulator thicknesses.

With Sensor Coating. Figure 6.4 shows the potential function along the lower and upper boundaries with various insulator thicknesses, d , using the data in Table 6.2. Again, the cell parameter values were selected using the CHEMFET structure as a guide and normalizing the cell dimensions with respect to the electrode's width. At the upper boundary, the potential is fairly linear from one electrode to the other (with $d = 5$). The potential is perturbed from this

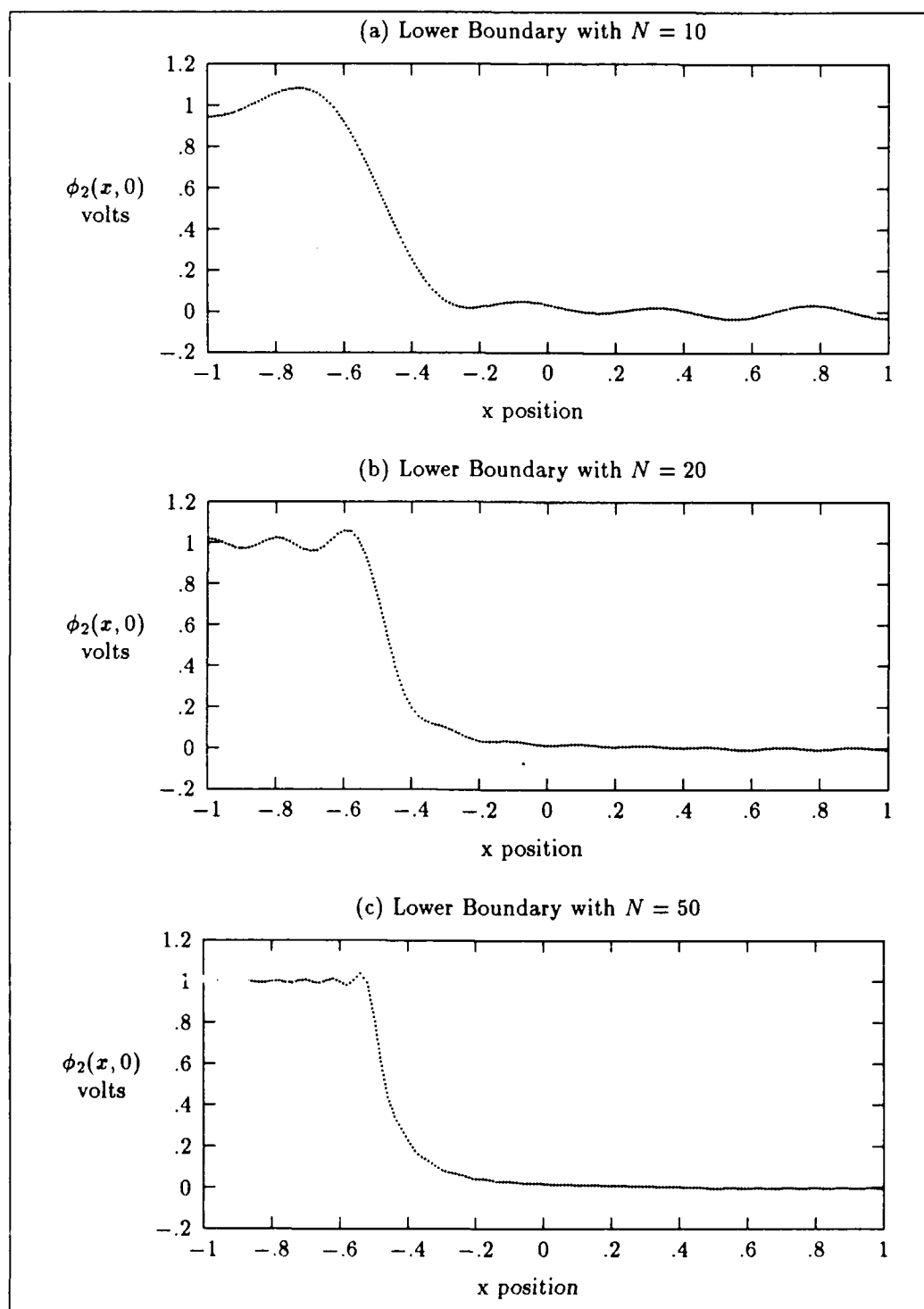


Figure 6.1. Potential function along lower boundary with $N = 10, 20$, and 50

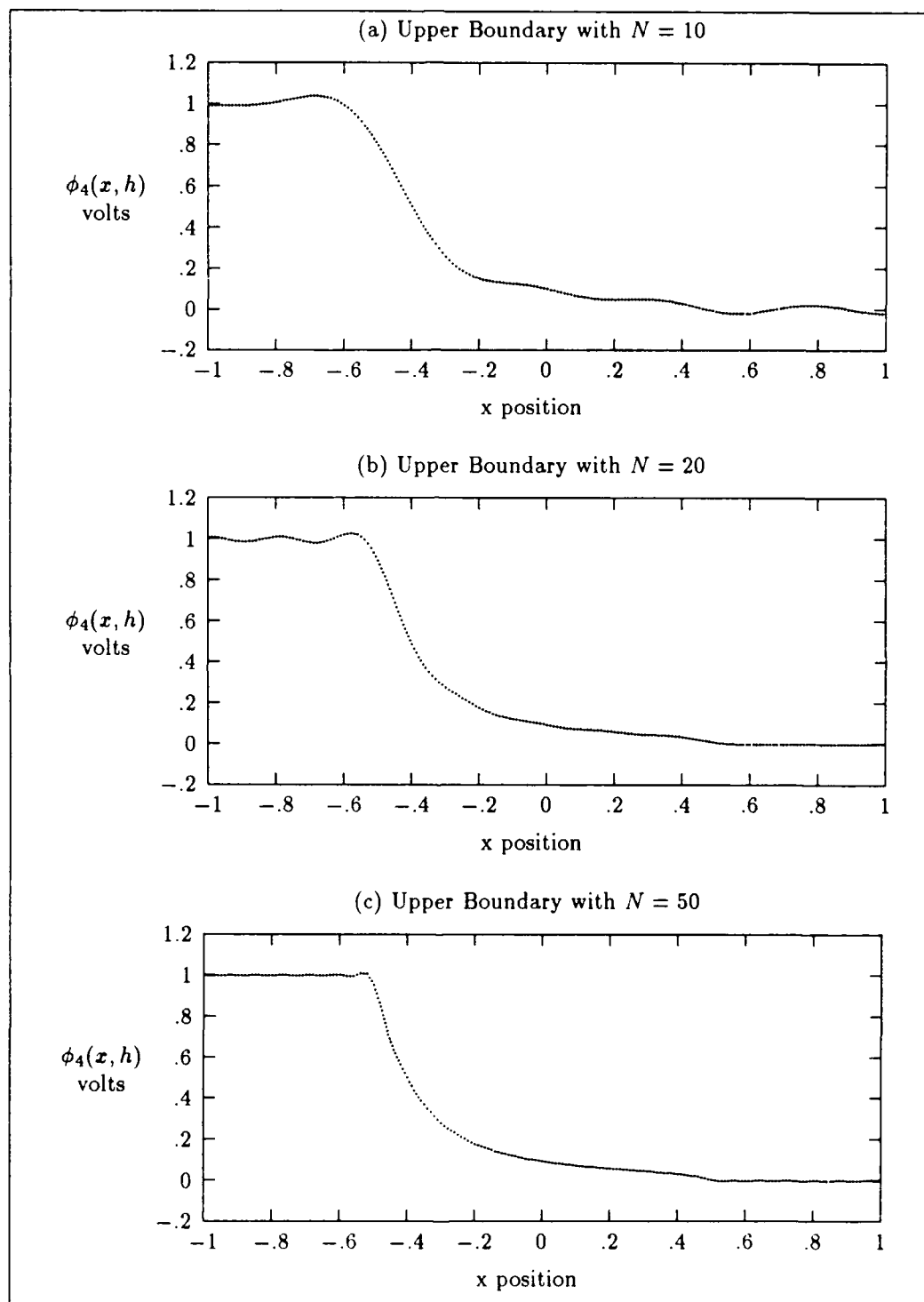


Figure 6.2. Potential function along upper boundary with $N = 10, 20$, and 50

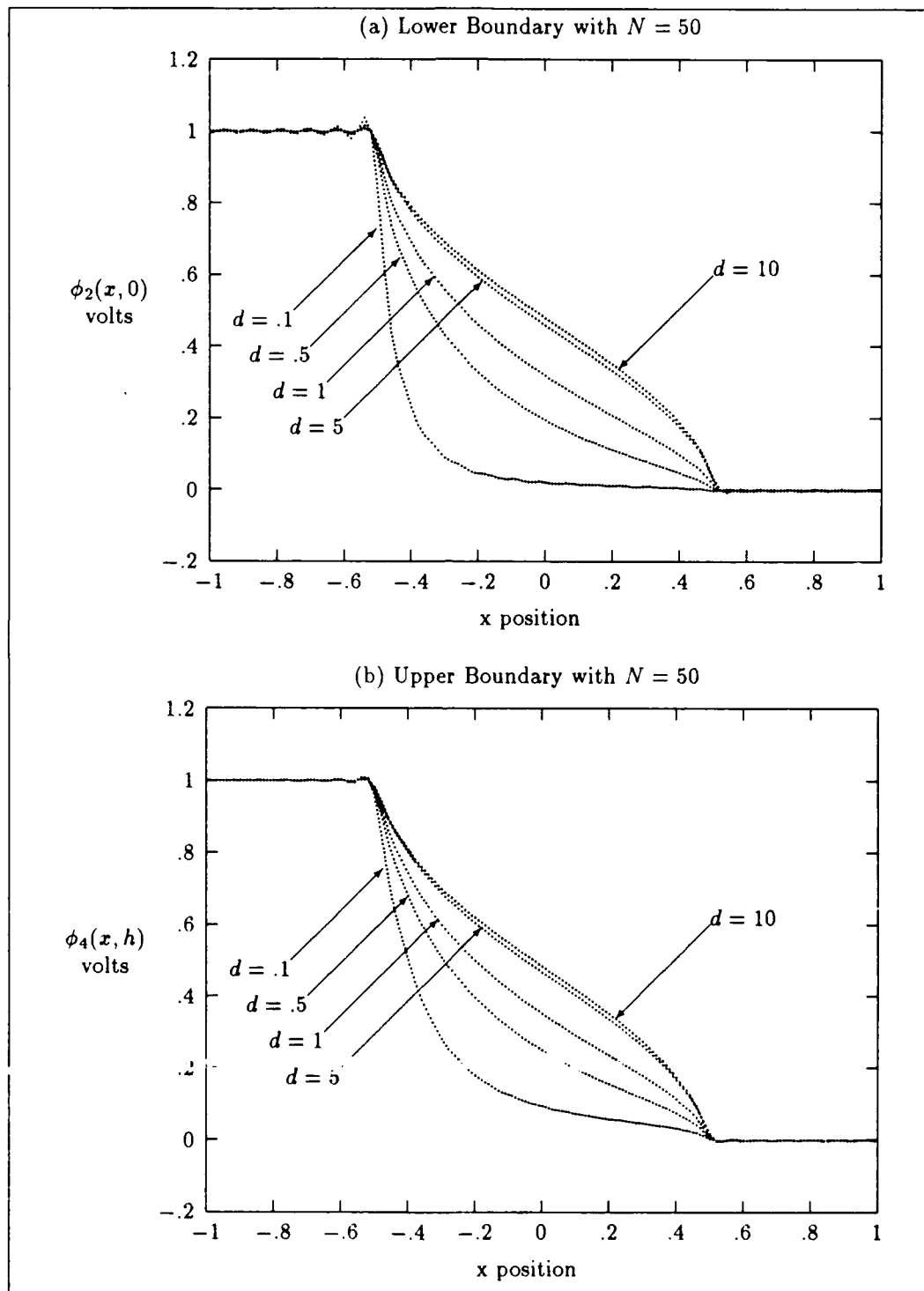


Figure 6.3. Potential function at the lower and upper boundaries with various d 's

linear behavior as the insulator is made thinner (smaller d). At the lower boundary with $d = 5$, the potential is still nearly linear, but the linearity is much more perturbed with a thinner insulator layer compared to the upper boundary.

Comparing Figures 6.3 and 6.4, the potential is nearly linear with the sensor coating above the electrodes as compared to the case of just air covering the electrodes.

Table 6.2. Normalized data used for boundary potentials (with coating)

parameter	d	h	l	s	ϵ_{r2}	ϵ_{r3}	ϵ_{r4}	ϵ_{r5}
value	0.1	0.1	0.11	1	3.9	3.9	500	1

6.1.2 Constant Voltage Contours. A FORTRAN computer program was created to calculate the potential in the cell, using the voltage coefficients obtained from the IMSL routine LSARG. A 100 by 100 point grid was established to view the potential in the cell, with a spacing of $(s + 1)/100$ between grid points. The voltage contour plots were created using AFIT's METALIB FORTRAN plotting routines; specifically, the contour plotting routine "RCONTR" [1] was utilized. Constant voltage contour plots were created for five cases. The model parameters of the five cases are shown in Table 6.3. The fundamental cell parameters were chosen using the CHEMFET structure as a guide; however specific variations were selected in each case to highlight certain aspects of the solution. Here again, the cell dimensions were normalized with respect to the electrode's width.

Table 6.3. Data used for voltage contour plots

case	Figure No.	V_1	V_2	d	h	l	s	ϵ_{r2}	ϵ_{r3}	ϵ_{r4}	ϵ_{r5}
A	6.5	1	0	1	0.1	0.11	1	1	1	1	1
B	6.6	1	-1	1	0.1	0.11	1	1	1	1	1
C	6.7	1	-1	1	0.1	0.11	1	1	100	1	1
D	6.8	1	-1	1	0.1	0.2	1	3.9	3.9	500	1
E	6.9	1	-1	0.1	0.1	0.11	1	3.9	3.9	500	1

Figure 6.5 displays the constant voltage contours using the data for case A. The left electrode is at a 1 volt potential, while the right electrode and bottom border are grounded ($V = 0$). All

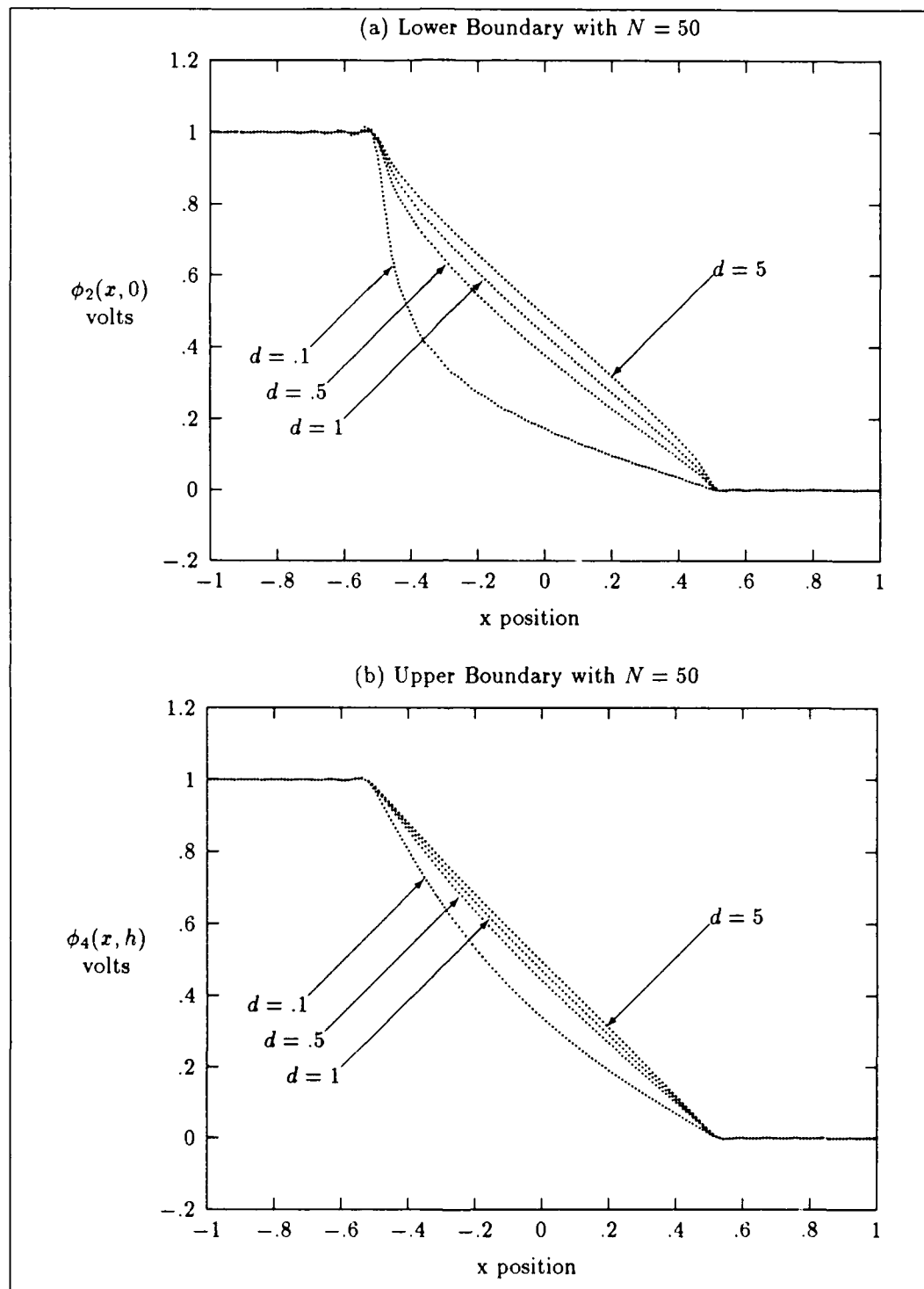


Figure 6.4. Potential function at the lower and upper boundaries with various d 's (with sensor coating)

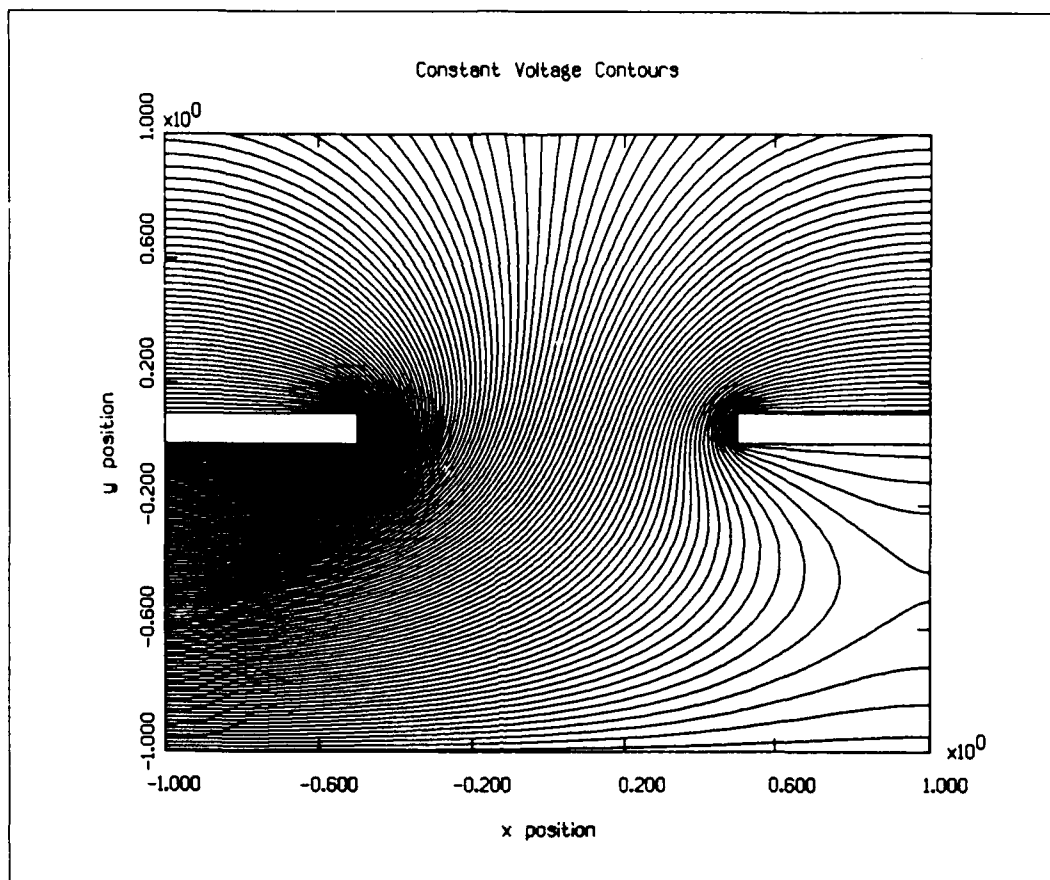


Figure 6.5. Constant voltage contours in cell using the case A data set

layers contain equal permittivity ($\epsilon_r = 1$). The curves are smooth across both boundaries (layers 2-3 and layers 3-4), which demonstrates that the numerical approximation of the solution matches very well at the boundaries. The plot contains 100 voltage levels, so each curve represents a step of 0.01 volts.

Figure 6.6 shows the constant voltage contours using the data for case B. The left and right electrodes have 1 and -1 volt applied respectively, while the bottom border is grounded. All layers contain equal permittivity ($\epsilon_r = 1$). Again the curves are smooth across the boundaries and 100 contour levels are shown, but the levels are now incremental steps of 0.02 volts (2 volt difference

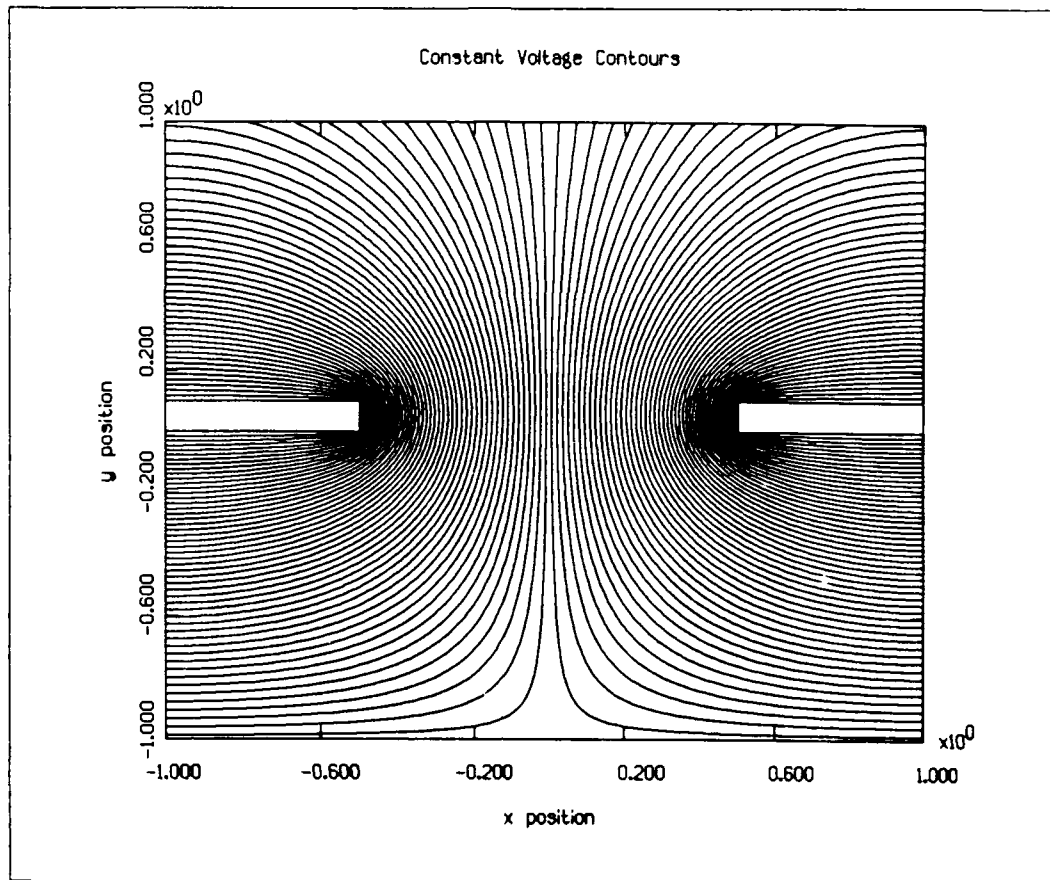


Figure 6.6. Constant voltage contours in cell using the case B data set

between electrodes). The strong electric field near the electrode corners is clearly illustrated, and the even symmetry is also apparent in the plot.

The constant voltage contours using the data for case C is shown in Figure 6.7. The electrodes are set to 1 and -1 volts, with the bottom border grounded. However, a high permittivity layer ($\epsilon_r = 100$) has been introduced between the electrodes. The layer is well defined and the strong electric field within the layer is observed in the contour plot. Again, 100 contour levels are shown with steps of 0.02 volts between curves.

Case D (Figure 6.8) introduces a thick, high permittivity, layer 4 ($\epsilon_r = 500$), while layers 2 and 3 are insulating material ($\epsilon_r = 3.9$) and layer 5 is air ($\epsilon_r = 1$). The electrodes have applied

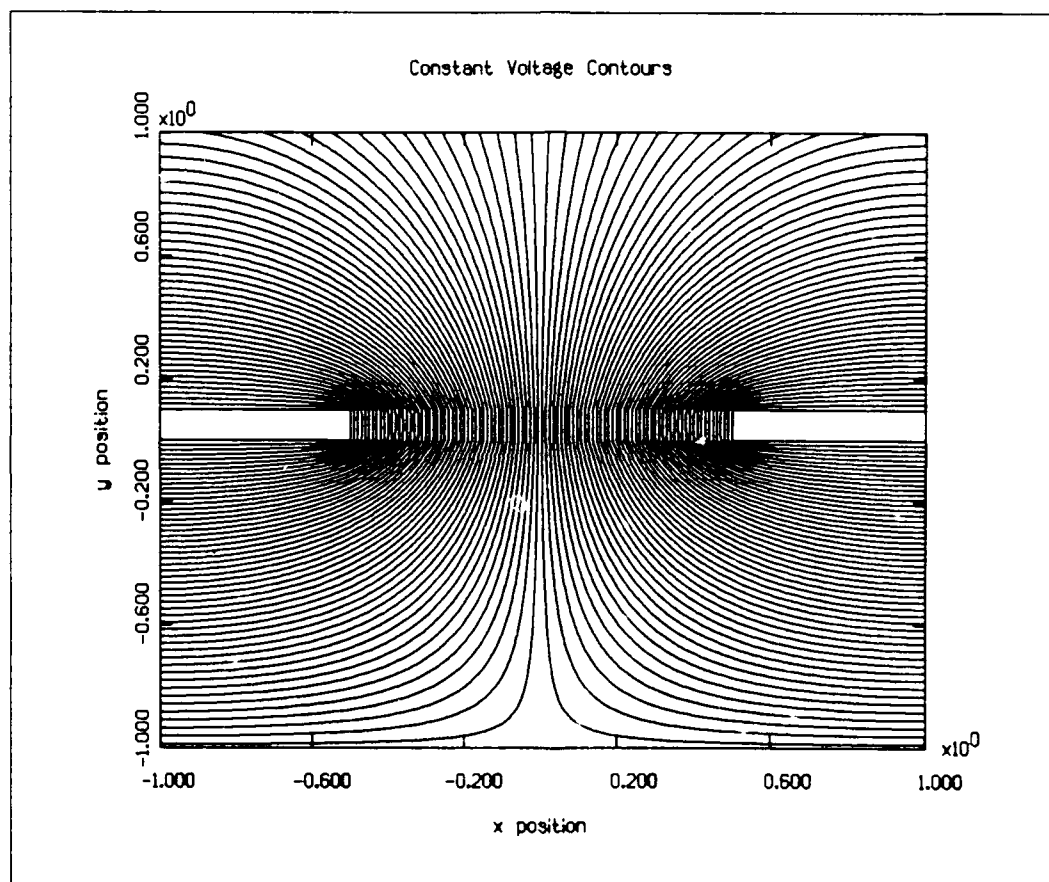


Figure 6.7. Constant voltage contours in cell using the case C data set

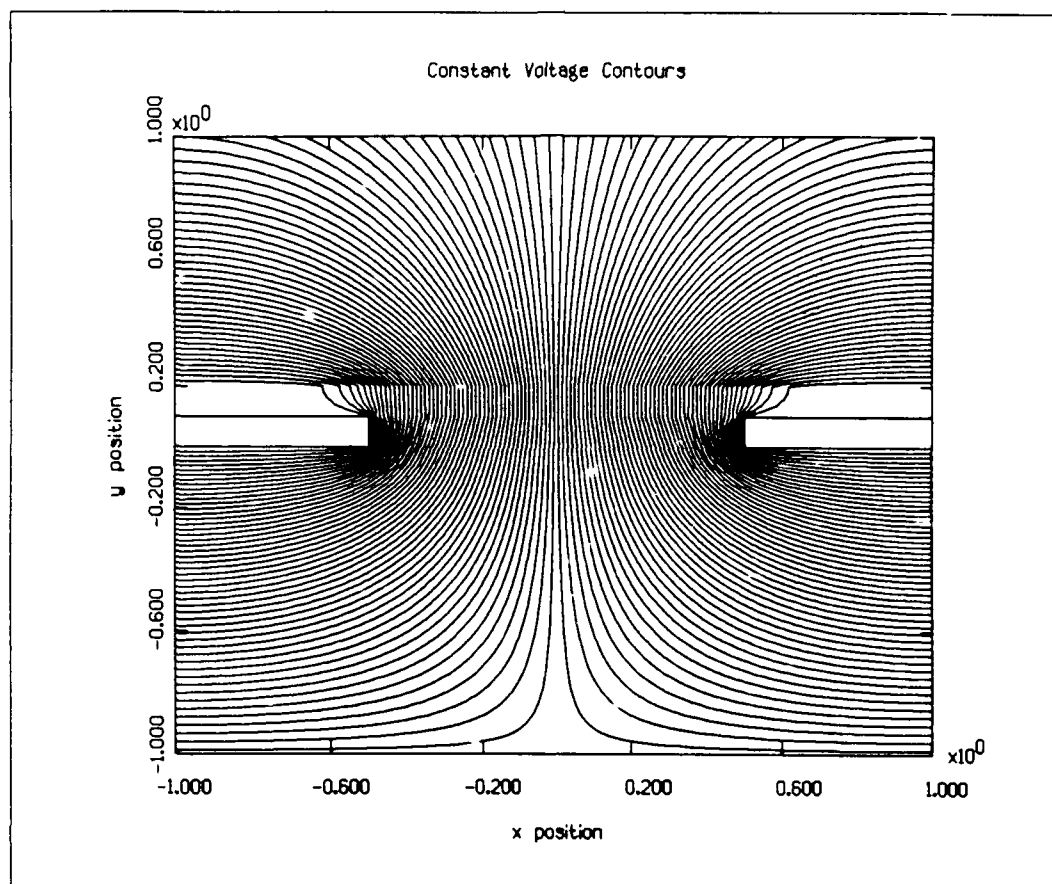


Figure 6.8. Constant voltage contours in cell using the case D data set

potentials of 1 and -1 volt, with the bottom of layer 2 grounded. Layer 4 is well defined in the plot and a strong electric field is observed within the layer. Again 100 contour levels are displayed with a step of 0.02 volts between curves. The solution is smooth across layers 2 and 3 since they contain equal permittivities.

Figure 6.9 and 6.10 display the constant voltage contours of the sensor cell with parameters selected to represent the CHEMFET. Layer 2 is a thin silicon dioxide layer ($\epsilon_r = 3.9$), layer 3 is P-glass ($\epsilon_r = 3.9$), layer 4 is a very thin polymer layer ($\epsilon_r = 500$), while layer 5 is air ($\epsilon_r = 1$). The bottom border is grounded and the electrodes are at ± 1 volt. Layer 4 is not easily seen due to the

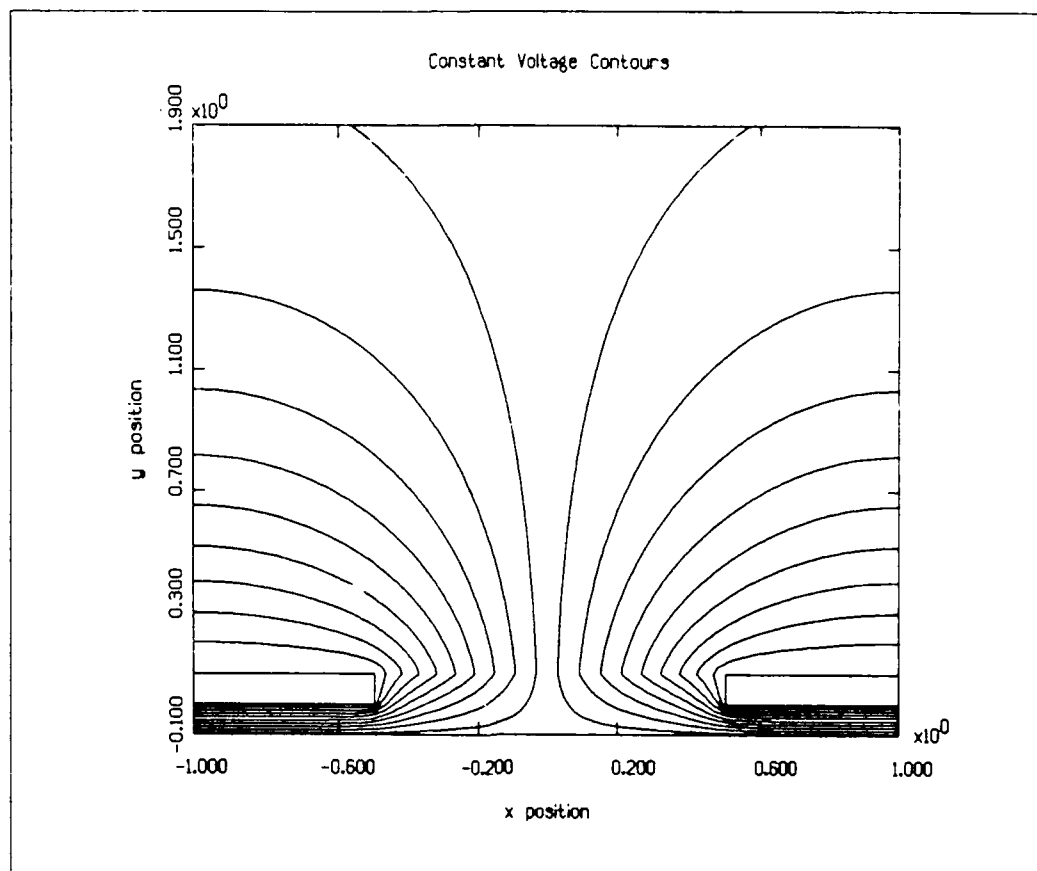


Figure 6.9. Constant voltage contours of the sensor cell with 40 contour levels

scale of the plot. Figure 6.9 contains 40 contour levels with a step of 0.05 volts between curves, while Figure 6.10 contains 80 contour levels with steps of 0.025 volts between curves.

The contour plots shown in Figures 6.5–6.10 illustrate that the solution behaves as expected and provide a visual representation of the solution under different conditions. Boundaries between layers are unrecognizable if the permittivities are identical across the interface. When the permittivities do not match, the boundary becomes well defined.

6.1.3 Capacitance Graphs. With approximations for the potential coefficients, the charge, and the capacitive elements can be calculated, using Equations 4.30, 4.60, and 4.63. Thus, we can experiment with the results and observe the change in the capacitive elements if we vary

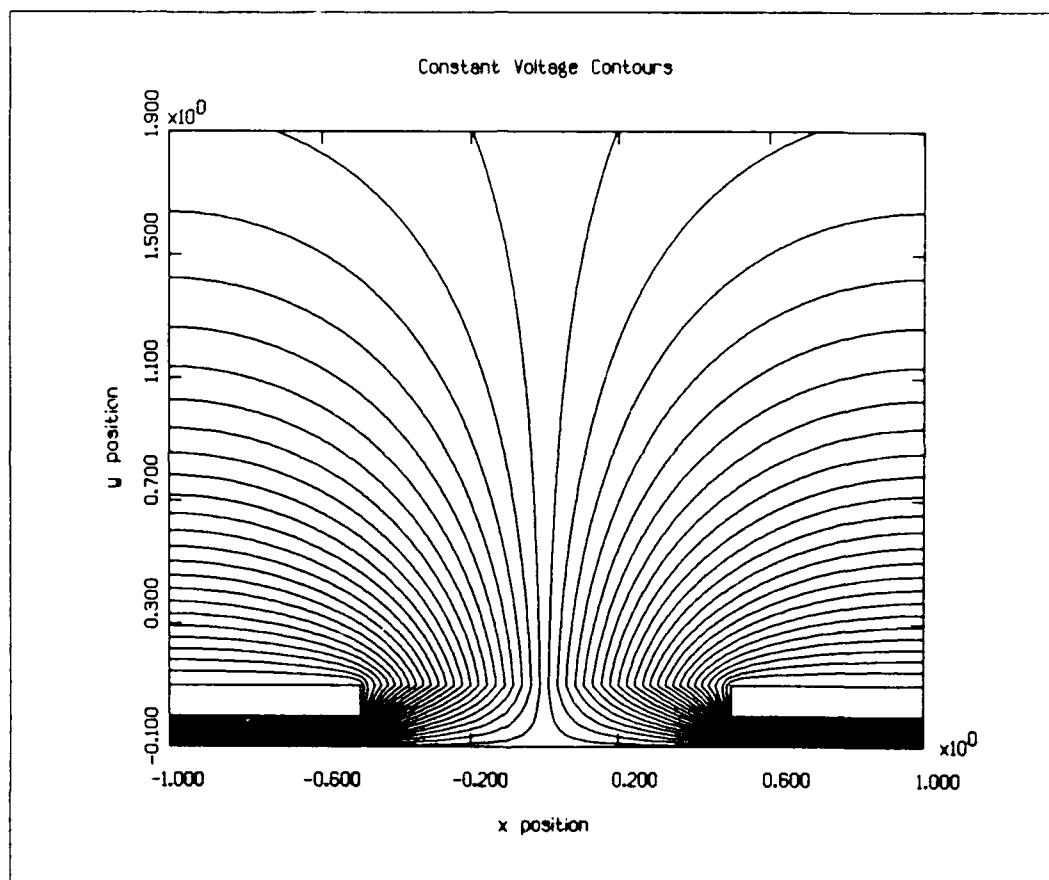


Figure 6.10. Constant voltage contours of the sensor cell with 80 contour levels

key parameters in the periodic cell. This investigation will examine the interdigitated electrode structure with and without the applied sensor coating. The model parameters established as the baseline for the investigation are shown in Table 6.4. These values were selected using the CHEMFET structure as a guide and the cell dimensions were normalized to the electrode's width. The cell capacitance terms are all expressed on a per unit length basis; that is, with units of Farads per centimeter (F/cm).

Table 6.4. Normalized model parameters used as the baseline for capacitance calculations

material above electrodes	d	h	l	s	ϵ_{r2}	ϵ_{r3}	ϵ_{r4}	ϵ_{r5}
air	0.1	0.1	0.11	1	3.9	1	1	1
insulator/sensor coating	0.1	0.1	0.11	1	3.9	3.9	500	1

6.1.3.1 Effects of Insulator Thickness on the Capacitive Elements. Figure 6.11 displays the capacitive elements, C_g and C_E , relative to a range of insulator thicknesses, with the remaining parameters set to their baseline values. The capacitance between electrodes, C_E , increases with insulator thickness, while the capacitance to ground, C_g , decreases. Figure 6.12 shows similar results for the case when the sensor coating is considered. Again, C_g decreases with increasing insulator thickness, while C_E increases. While C_g increases slightly when the sensor coating is considered, C_E increases by a factor of 10. To understand these results, an analysis of the cell is needed.

With a thin insulating layer, most of the electric flux exists between each electrode and the ground plane. As the insulator thickness is increased, there will be a proportionately greater flux between the electrodes and a lesser amount between each electrode and the ground plane. Therefore, as the insulator thickness is increased, we should expect C_E to increase and C_g to decrease.

6.1.3.2 Effects of Electrode Height on the Capacitive Elements. Figure 6.13 shows the capacitive elements, C_g and C_E , relative to a range of electrode heights, with the remaining model parameters set at their baseline values. In the case of air above the electrodes, the numerical results

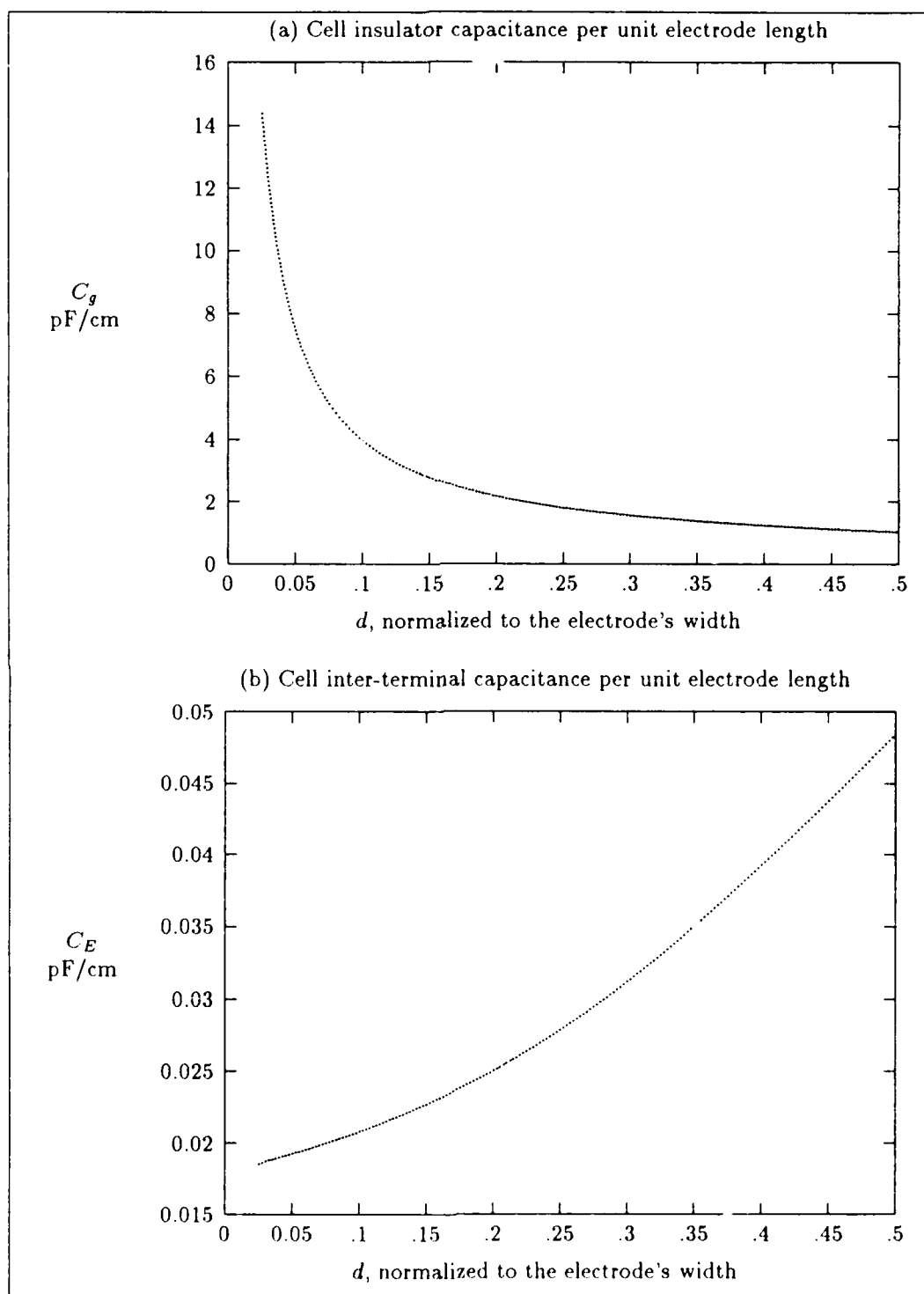


Figure 6.11. Capacitive element graphs for varying d , with air above the electrodes

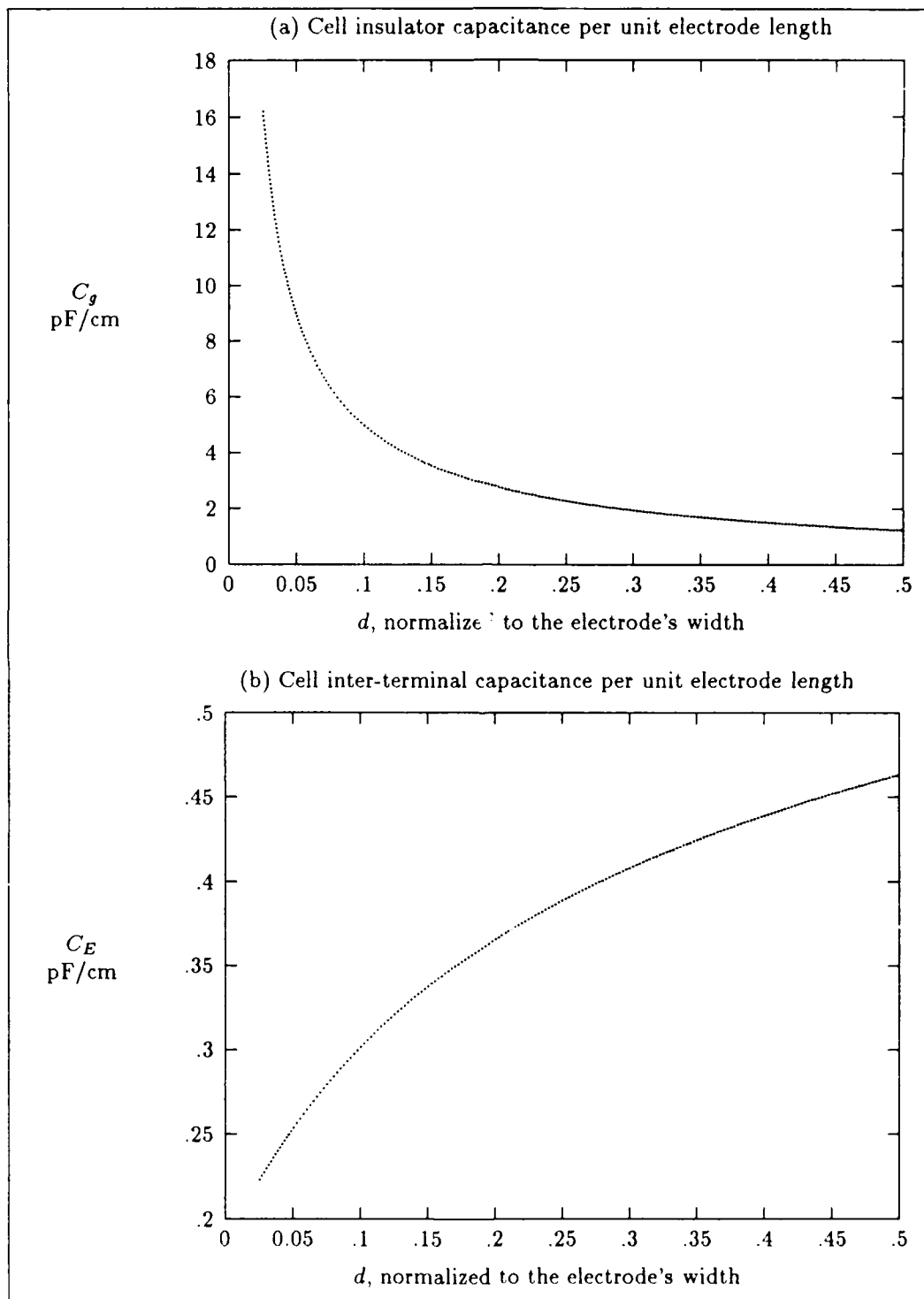


Figure 6.12. Capacitive element graphs for varying d , with the sensor coating considered

shows that both C_g and C_E increase with electrode height. Figure 6.14 displays similar results for the capacitive elements with the sensor coating considered. Again, C_E increases with electrode height, but now C_g decreases. Also, C_E increases by a factor of 10 when the sensor coating is considered. To understand the influence of the electrode height on the capacitive elements, an analysis of the cell is required.

Increasing the electrode height provides more surface area for charge storage, which means that the electric field between the electrodes increases. Therefore, increasing the electrode height should increase C_E . With air above the electrodes, the potential functions across the layer 3 interfaces are non-linear (see Figure 6.3), indicating that most of the cell's electric flux is concentrated between the electrodes and the ground plane rather than between the two electrodes. For this case, increasing the electrode height should increase C_g due to the increased charge storage capacity. With the sensor coating considered, the potential functions along the layer 3 interfaces are significantly more linear (see Figure 6.4), indicating that more flux is concentrated between the two electrodes. In this case, increasing the electrode's height will decrease C_g due to the correspondingly increased electric field between the two electrodes.

6.1.3.3 Effects of Electrode Separation on the Capacitive Elements. Figure 6.15 displays the capacitive elements, C_g and C_E , relative to a range of electrode separations, with the remaining model parameters set to their baseline values. The numerical results show that C_g increases with larger separation, approaching the limiting value for the parallel combination of two uncoupled microcaps in the layered materials. The results also indicate that the inter-terminal capacitance, C_E , decreases with larger separation. Figure 6.16 shows similar results for the capacitive elements when the sensor coating is considered. Again, C_g increases with larger electrode separation to a limiting value, while C_E decreases. To understand these results, an analysis of the cell is needed.

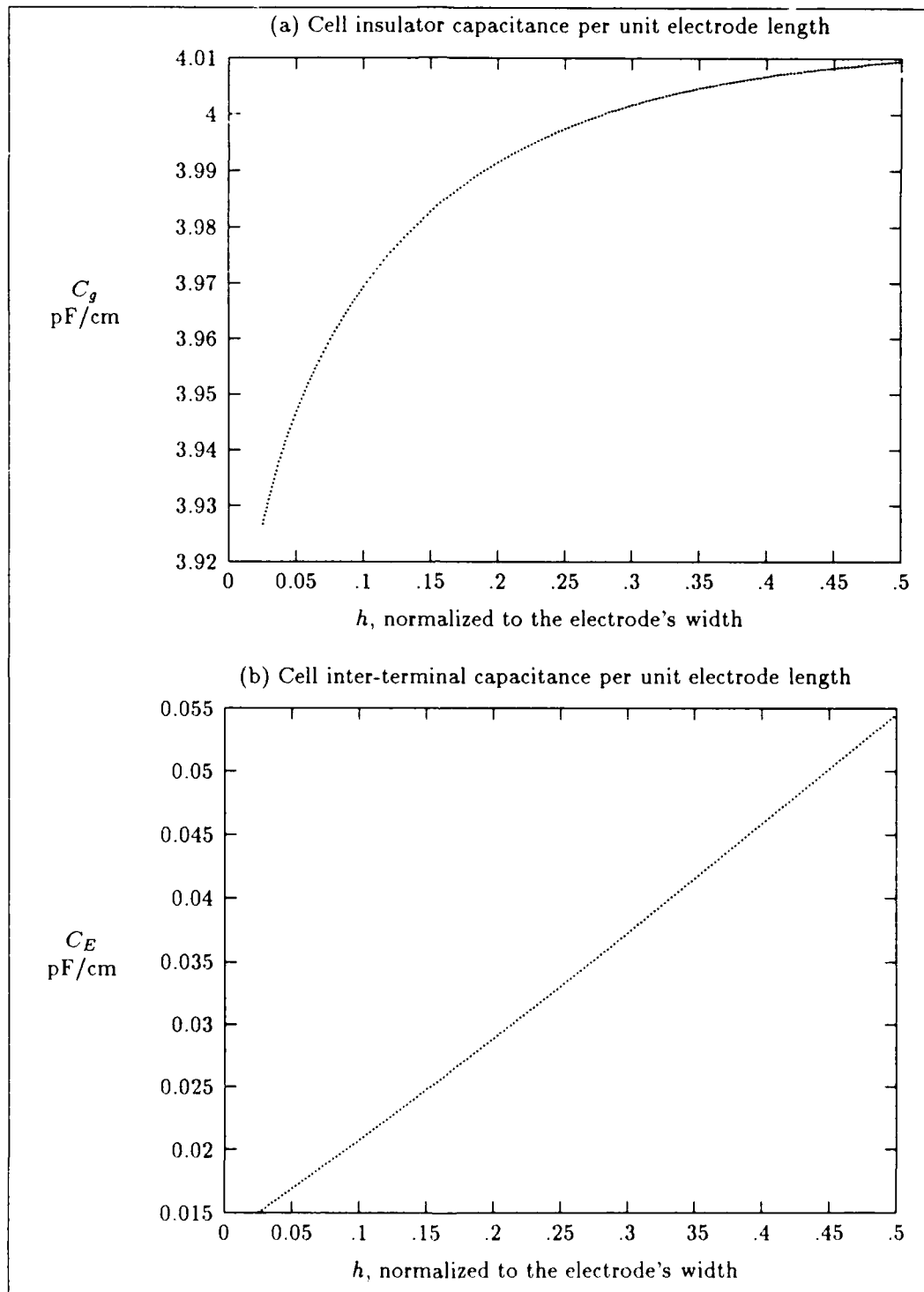


Figure 6.13. Capacitive element graphs for varying h , with air above the electrodes

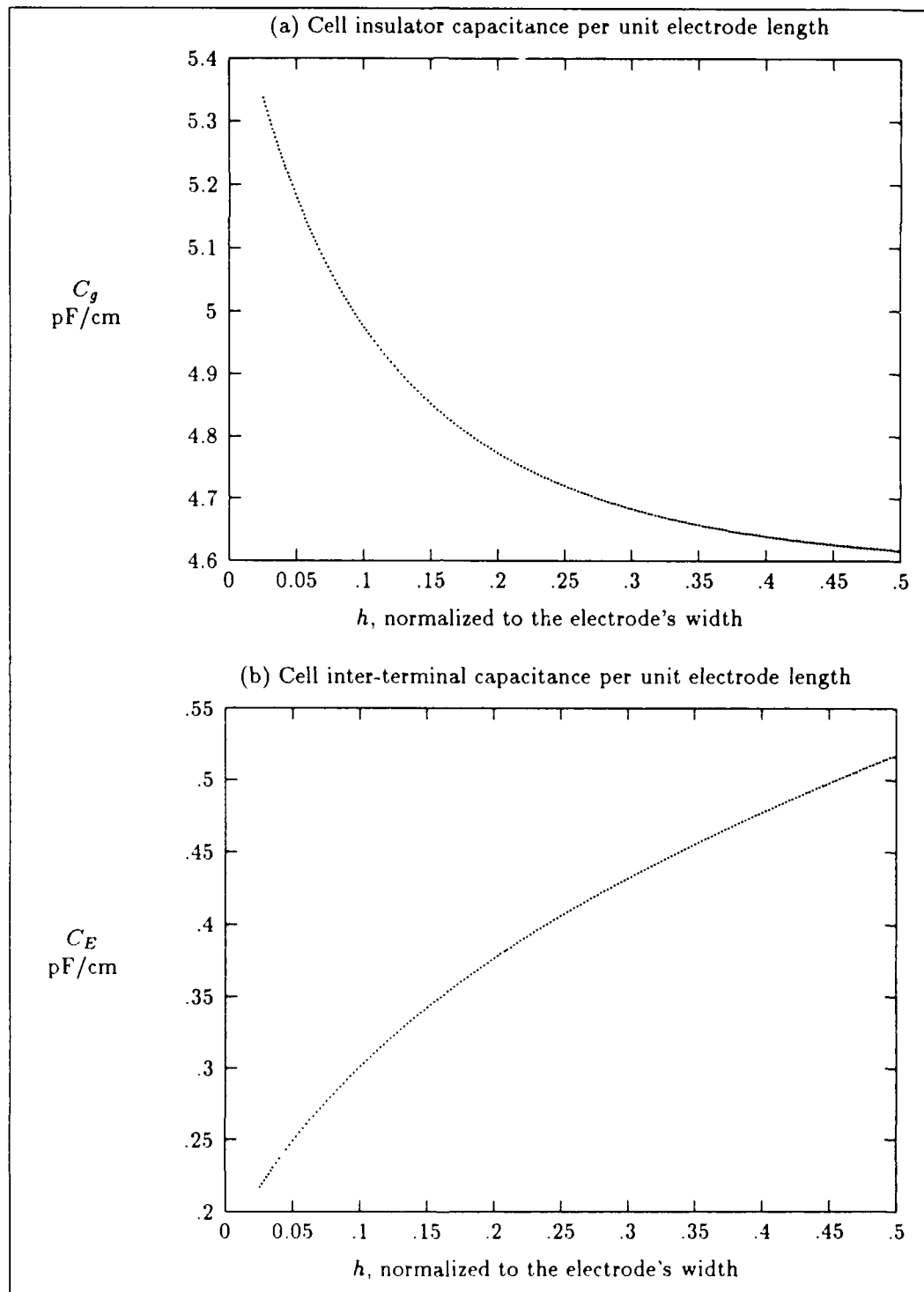


Figure 6.14. Capacitive element graphs for varying h , with the sensor coating considered

Increasing the electrode separation decreases the electric field between the electrodes and this phenomenon magnifies the effect of the ground plane on each conductor. Therefore, the capacitance to ground should increase with more separation until the cell is, effectively, two uncoupled microstrips, while the capacitance between the electrodes should decrease with more separation. In addition, the extreme case of $s = 0$ will result in the cell effectively having only one electrode, with the capacitance to ground becoming, essentially, a parallel plate capacitance.

6.1.3.4 Effects of Sensor Coating Thickness on the Capacitive Elements. Figure 6.17 shows the capacitive elements, C_g and C_E , relative to a range of sensor coating thicknesses, with the remaining cell parameters set to their baseline values. The numerical results show that an increase in sensor coating thickness, p , will increase both C_g and C_E . From the graphs, C_g is more sensitive to changes in the sensor coating thickness compared to C_E when the coating thickness is at the thinner end of the range. However, C_E is more sensitive to changes in the sensor coating's thickness compared to C_g when the coating thickness is at the thicker end of the range. To understand the overall effect of the sensor coating thickness on the capacitance values, an analysis of the cell is necessary.

The sensor coating layer has a large relative permittivity, and its presence was observed to affect the electric flux of the periodic cell (see Figures 6.3 and 6.4). The presence of the sensor coating acts to increase the electric field strength between the electrodes, and it correspondingly reduces the influence of the ground plane on the conductors. Since the insulator is so thin (the electrodes are much closer to the ground plane compared to their separation), some of the electric flux within the sensor coating reaches the ground plane. Therefore, increasing the sensor coating thickness should increase both the capacitance between the electrodes and the capacitance to ground.

6.1.3.5 Effects of Sensor Coating Permittivity on the Capacitive Elements. Figure 6.18 displays the numerical results of the capacitive elements, C_g and C_E , relative to a range of relative permittivities for the sensor coating, with the remaining model parameters set to their baseline val-

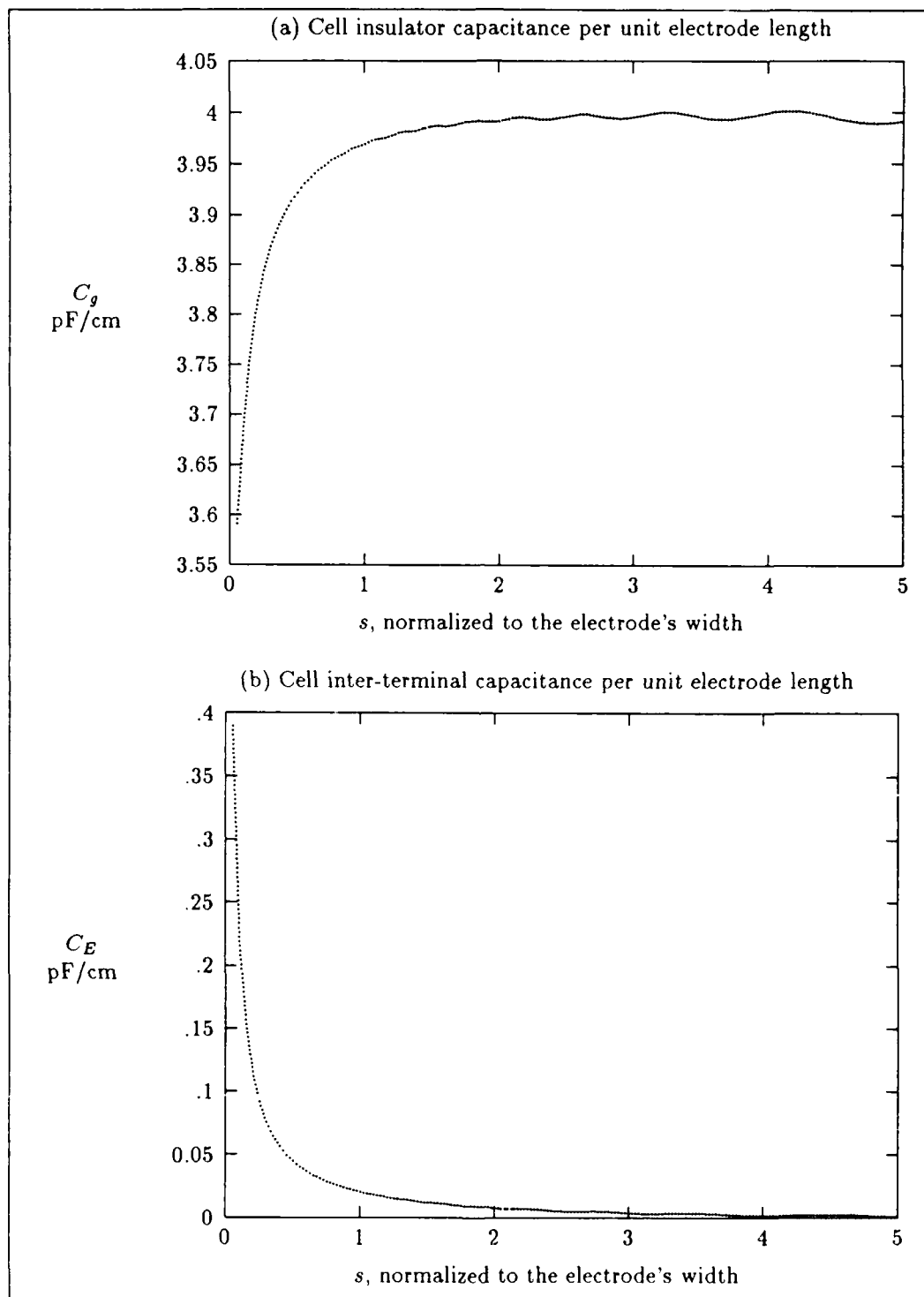


Figure 6.15. Capacitive element graphs for varying s , with air above the electrodes

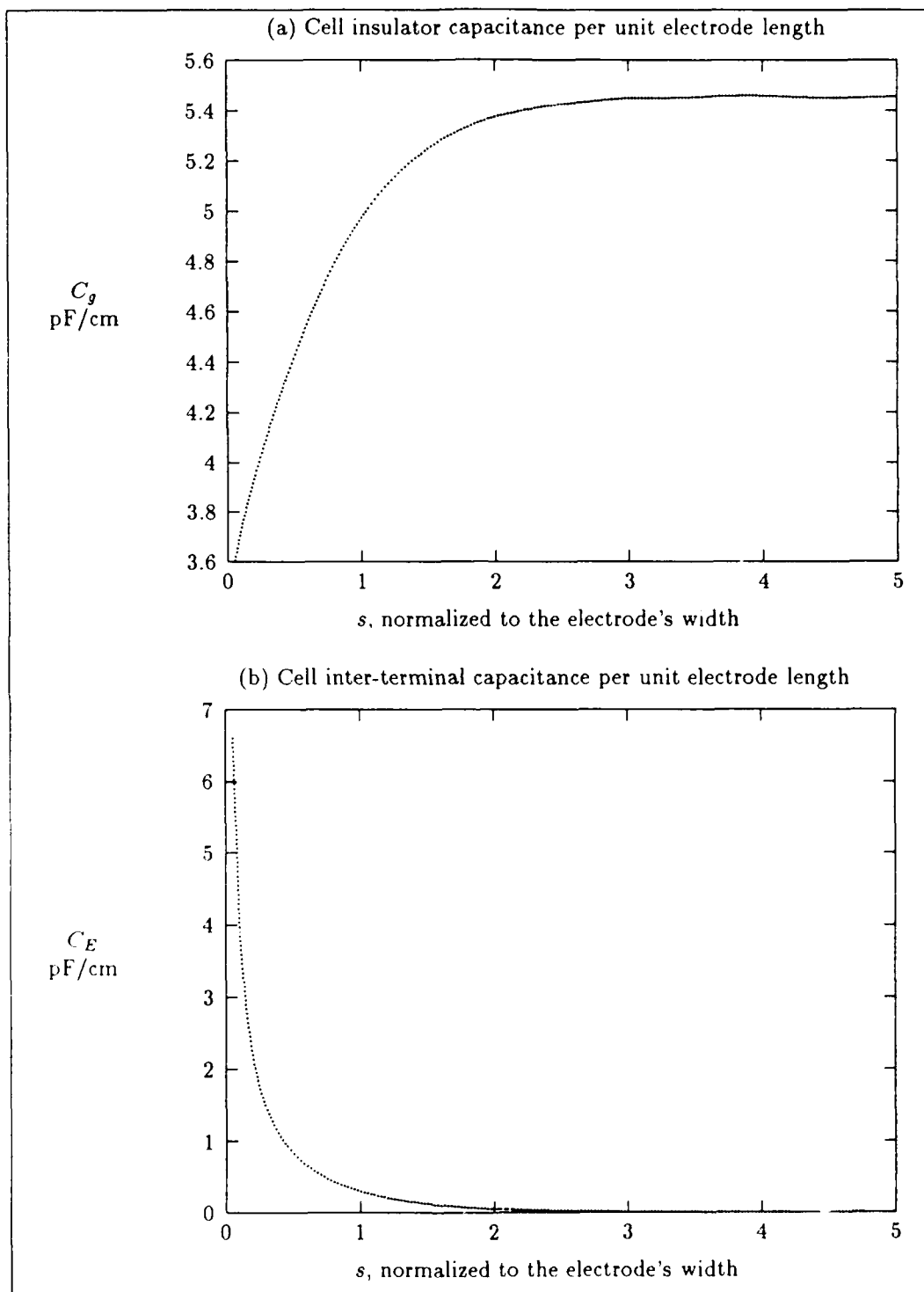


Figure 6.16. Capacitive element graphs for varying h , with the sensor coating considered

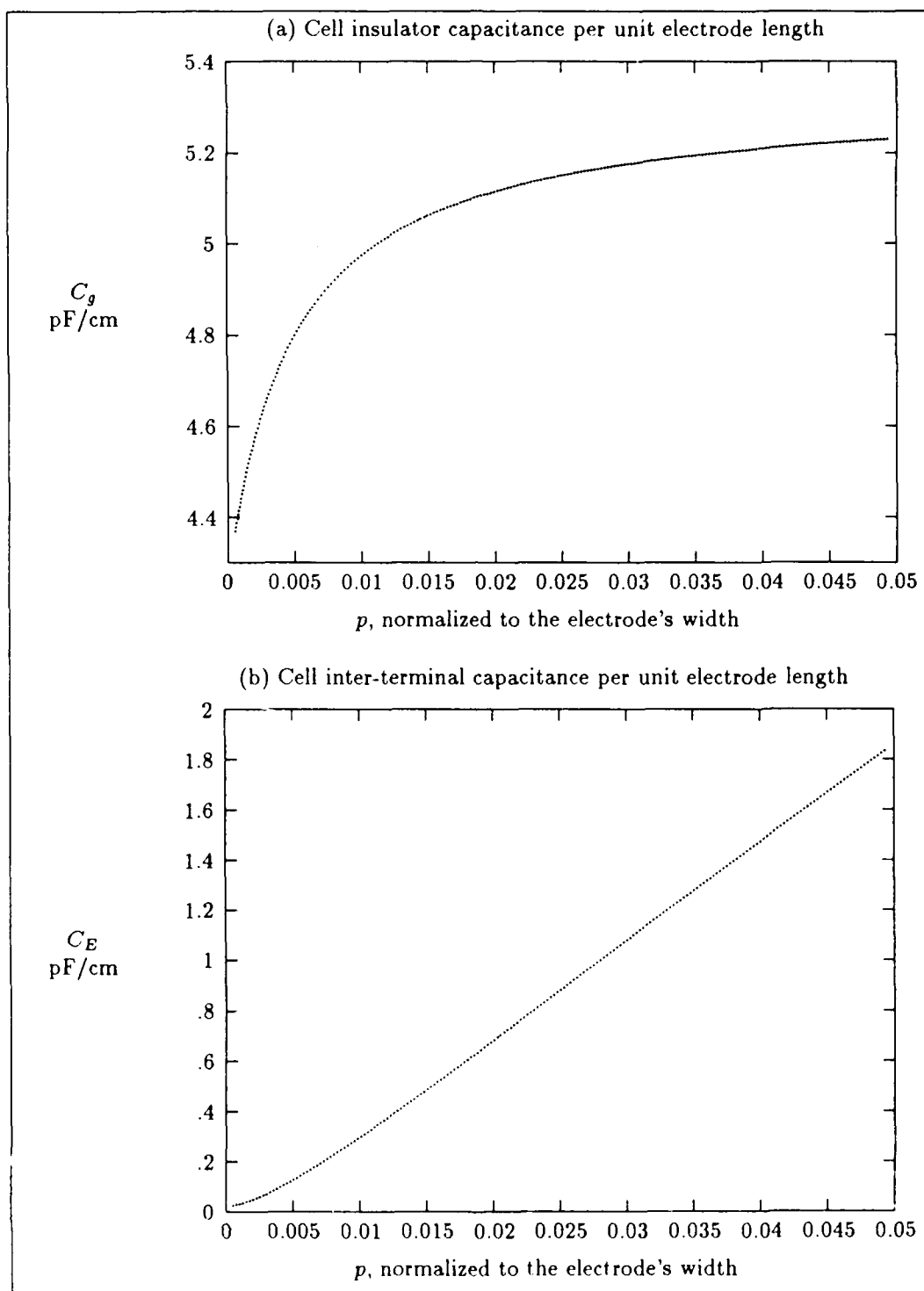


Figure 6.17. Capacitive element graphs for varying p , with the sensor coating considered

ues. The results show that both C_g and C_E increase with an increase in the relative permittivity of the sensor coating ($\epsilon_4 = \epsilon_{r4}\epsilon_o$, where ϵ_o is the permittivity of free space). These results indicate that C_g is strongly dependent on the sensor coating's material properties (this was not expected at the outset of this investigation) and provide evidence that both capacitive elements play a major role in the sensing action of such a device. As discussed in the previous section, the sensor coating layer affects both C_g and C_E . Therefore, an increase in the sensor coating's permittivity should increase both capacitive elements.

6.2 Results of the Resistive Solution

A FORTRAN program was created to solve the matrix equation in section 5.4, and thereby approximate the potential within the resistive layer. The program utilized the IMSL gaussian elimination routine "LSARG" [7:11]. The results were then used to calculate the resistance of the sensor coating layer with varying parametric conditions, using Equation 5.22.

6.2.1 Illustrating the Resistive Potential Solution. To illustrate the solution, the potential along the lower boundary is displayed in Figure 6.19. The displayed potential satisfies the boundary data of the problem; specifically, the potential on the left electrode is +0.5 volts while the potential on the right electrode is -0.5 volts. The potential is essentially linear between the electrodes. To illustrate the potential distribution within the layer, it was calculated at discrete points on a 100 by 50 point grid. The grid spacing in the x direction is $(s+1)/100$, while the spacing in the y direction is $p/50$. A plot of constant voltage contours was created using AFIT's METALIB plotting routines [1]. Figure 6.20 displays the constant voltage contour plot (50 contour levels) with steps of 0.02 volts between curves. Figure 6.21 shows the constant voltage contours of the same grid with 100 contours and steps of 0.01 volt between curves.

6.2.2 Resistive Element Graphs. With estimates for the coefficients of the potential function, the resistance of the layer was determined using Equation 5.22. The behavior of the resistive

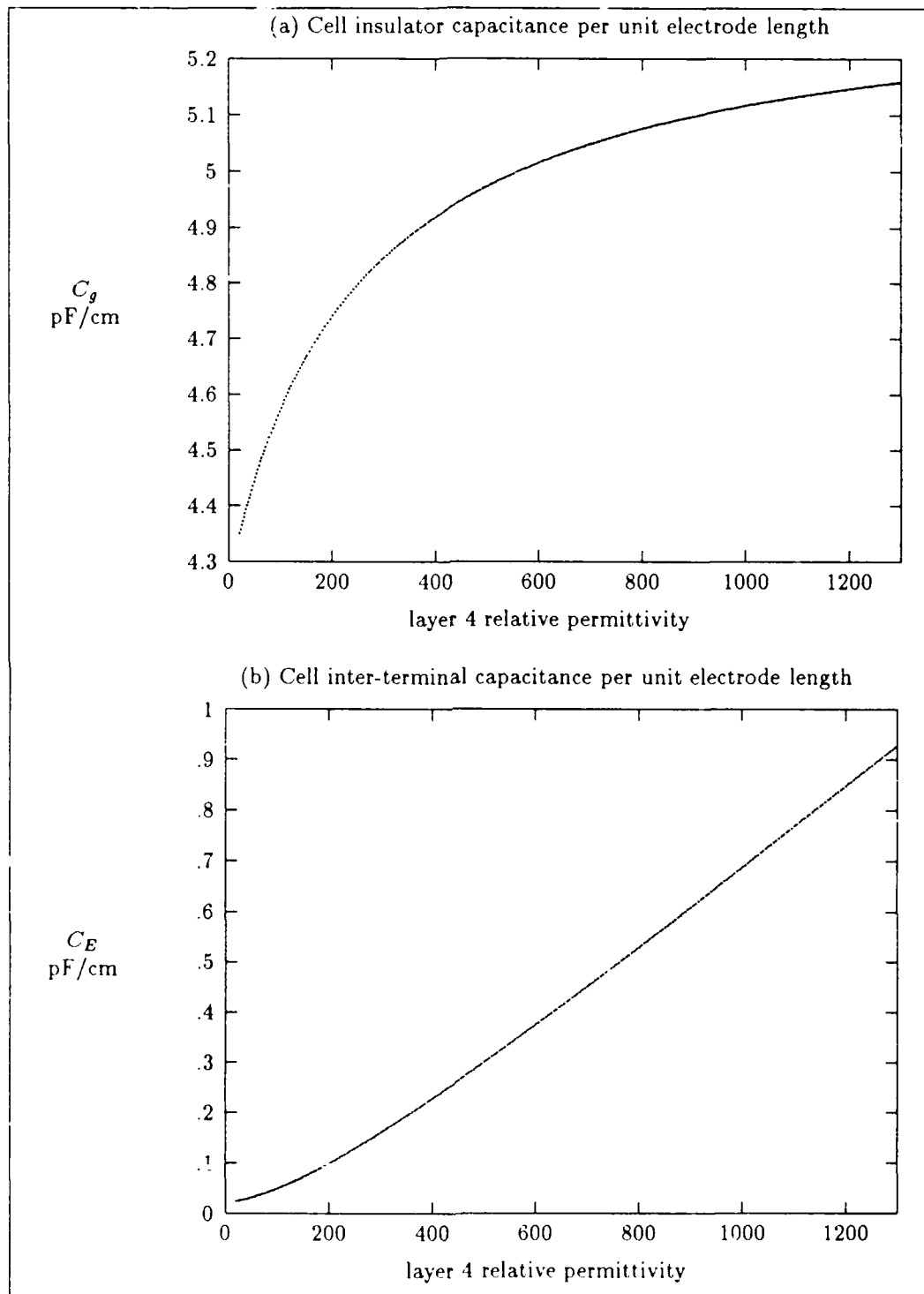


Figure 6.18. Capacitive element graphs for varying permittivity in layer 4

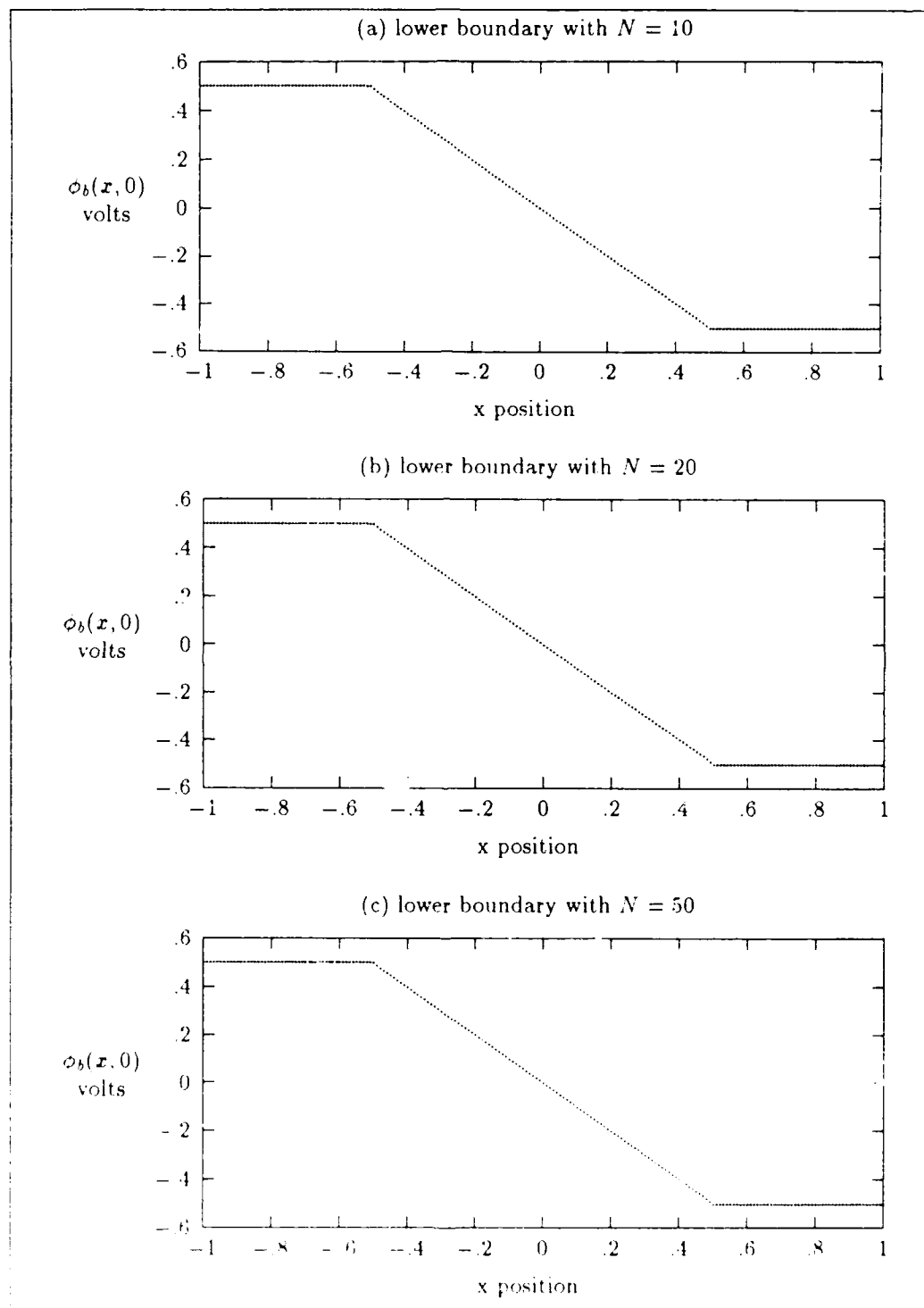


Figure 6.19 Lower boundary of the resistive solution with $N = 10, 20$, and 50

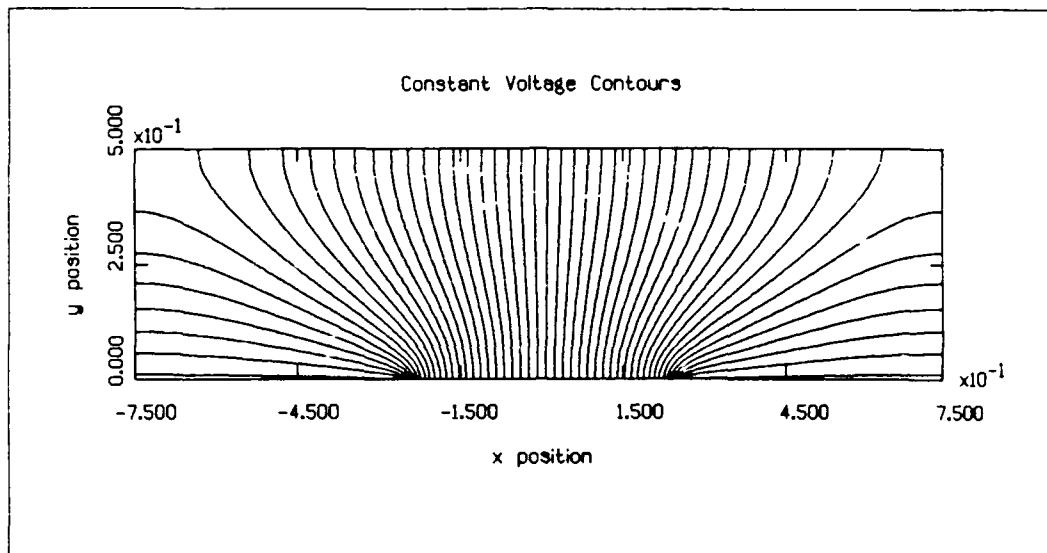


Figure 6.20. Low frequency constant voltage contours (50) in the sensor coating layer

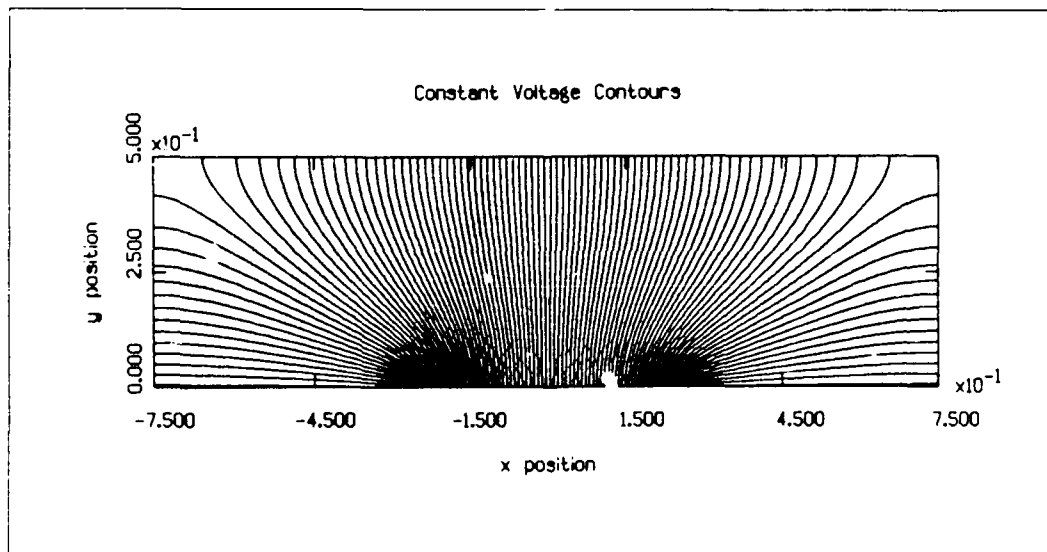


Figure 6.21. Low frequency constant voltage contours (100) in the sensor coating layer

element can be investigated by experimenting with the solutions and results of the resistive solution while varying key parameters of the periodic cell. All resistance values displayed are expressed on a unit length basis, with units of Ohms centimeter ($\Omega\text{-cm}$). The baseline model parameters used to investigate the resistive element are shown in Table 6.5. Again, these cell parameter values were selected using the CHEMFET structure as a guide and the cell dimensions were normalized with respect to the electrode's width.

Table 6.5. Normalized model parameters used as baseline for the resistive calculations

parameter	p	s	σ_4
value	0.01	1	10^{-8}

6.2.2.1 Effects of Sensor Coating Thickness on the Resistive Element. Figure 6.22 shows the behavior of the model resistive element, R_p , relative to a range of values for the sensor coating thickness, with the remaining parameters set to their baseline values. These results show that as the sensor coating's thickness increases, the resistance decreases. With a thicker sensor coating layer, there is more resistive material present; and hence, the resistance through the material should decrease. In the CHEMFET application, the sensor coating is expected to be thin (small relative to the other cell dimensions, including the oxide thickness), since the coating is applied by a vapor deposition process.

6.2.2.2 Effects of Electrode Separation on the Resistive Element. Figure 6.23 displays the behavior of the resistive model element, R_p , relative to a range of the electrode's separation, with the remaining model parameters set to their baseline values. With a thin sensor coating layer ($p = 0.01$), there is a linear relationship between the electrode separation and R_p . This linear relationship permits a comparison with the results obtained from the formula for a parallel plate resistor approximation. With this assumption, the inter-terminal resistance for a unit length, R_p , becomes

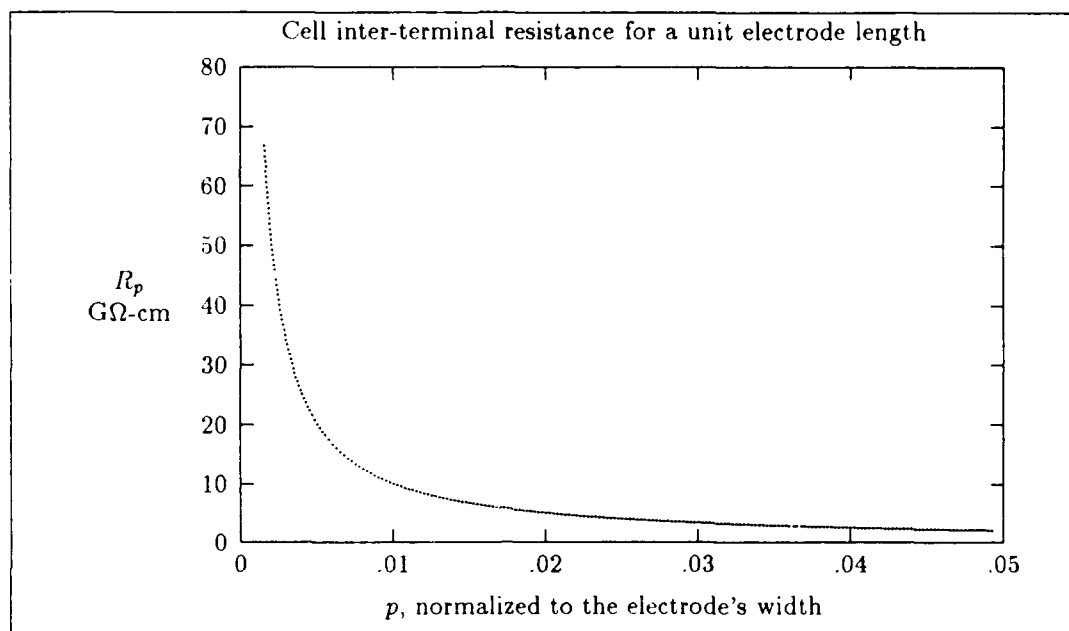


Figure 6.22. Cell resistance graph for varying p

$$R_p = \frac{s}{\sigma p} \quad (6.1)$$

Using the baseline values, the parallel plate approximation yields 1 GΩ-cm, while the numerical solution is 1.01 GΩ-cm. Therefore, the parallel plate approximation matches the numerical solution to within 1% for this one set of calculations, which considered a thin layer ($p \ll s$).

6.2.2.3 Effects of Sensor Coating Conductivity on the Resistive Element. Figure 6.24 shows the effect of the sensor coating's conductivity on the model element R_p . These results demonstrate a strong dependence of the resistance element to the sensor coating's material properties, as expected from the parallel plate estimate. Therefore, any change in the sensor coating's conductivity directly affects the resistance between the electrodes, and suggests that the resistive element is also a major factor in the sensing action of the structure.

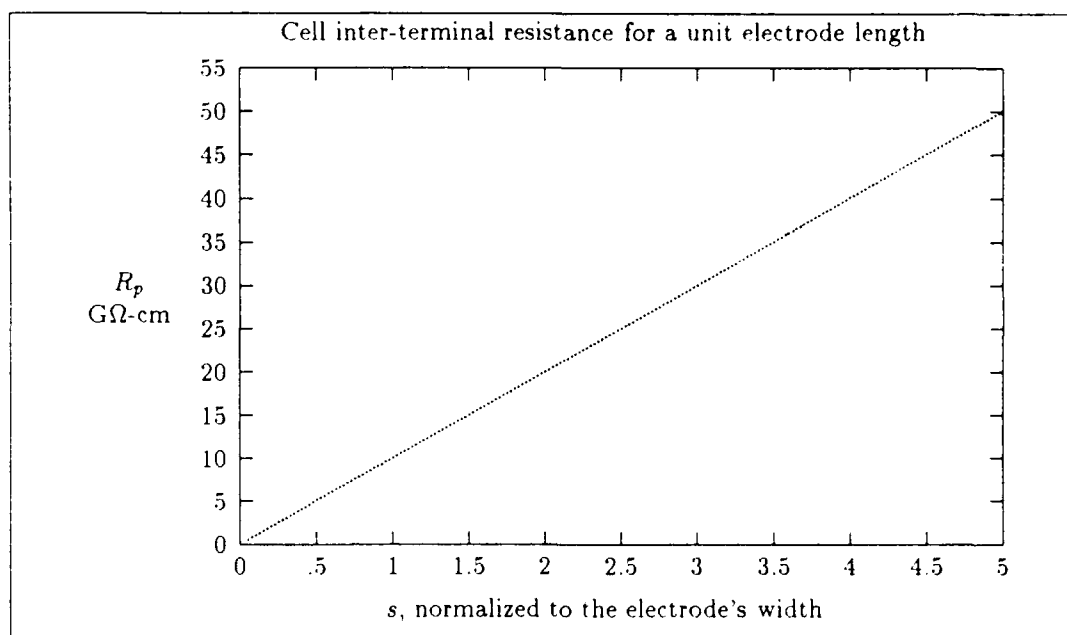


Figure 6.23. Cell resistance graph for varying s

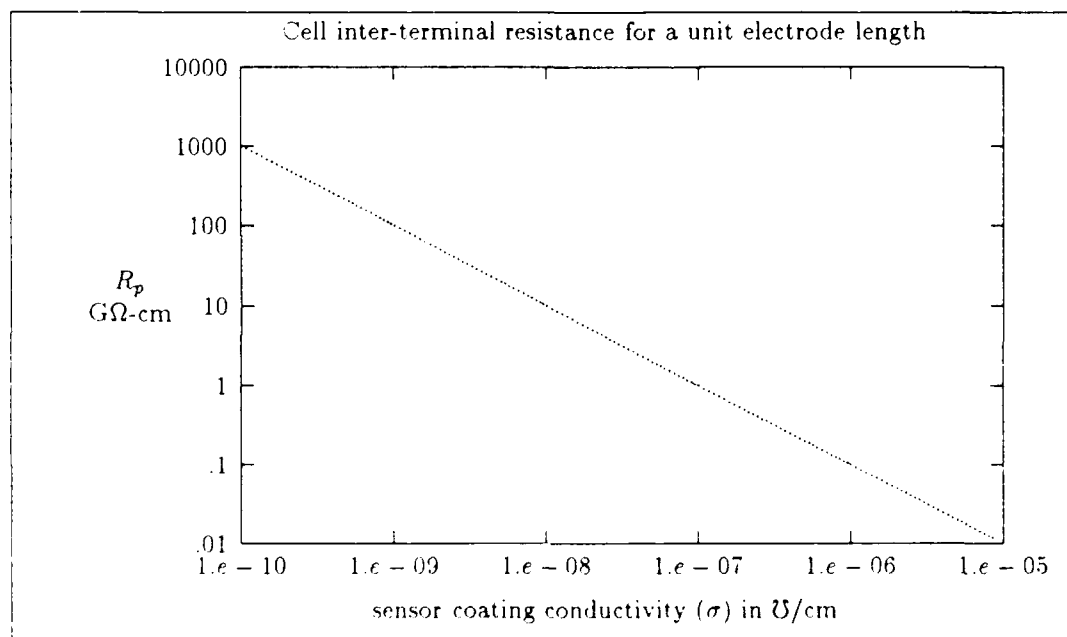


Figure 6.24. Cell resistance graph for varying conductivity in the sensor coating

VII. Frequency Dependence of the Model Elements

In this chapter, an analysis of the complex boundary condition at the interfaces between the material layers is used to determine the frequency dependence of the model elements. Thus far, the analysis leading to the capacitive and resistive elements was based upon the high and low frequency arguments of Equation 3.41. Therefore, the previous results were limited to the high frequency capacitance and DC (direct current) resistance. It would be beneficial to verify the validity of the previous results and determine the frequency dependence of the model elements. Towards this objective, let us consider the complex boundary condition presented in Equation 3.41

$$\left(\epsilon_1 - j\frac{\sigma_1}{\omega}\right) E_{n_1} = \left(\epsilon_2 - j\frac{\sigma_2}{\omega}\right) E_{n_2} \quad (7.1)$$

where ϵ is the permittivity of the material, σ is the conductivity of the material, ω is the angular excitation frequency, and E_{n_k} is the normal component of the electric field in layer k . A dimensionless complex relative permittivity, ϵ^* , can be defined as

$$\epsilon^* = \epsilon_r - j\frac{\sigma}{\omega\epsilon_0} \quad (7.2)$$

where ϵ_0 is the permittivity of free space and ϵ_r is the real relative permittivity of the material ($\epsilon = \epsilon_r\epsilon_0$). Using Equation 7.2 in 7.1 yields

$$\epsilon_1^* E_{n_1} = \epsilon_2^* E_{n_2} \quad (7.3)$$

Using Equation 7.3, the capacitive (or high frequency) problem formulation can be extended to all frequencies by replacing the real relative permittivity with the complex formulation, provided the potential is also complex so as to satisfy the complex boundary conditions.

Using the complex relative permittivity defined in Equation 7.2 and the complex IMSL gaussian elimination routine "LSACG" [7:31], the complex coefficients of the potential in each region can be found. With the potential known, the electric field can be determined which leads to both

the real charge on the electrode, as well as the real current flowing between the terminals. From the charge and current, the capacitance is found using Equations 4.60 and 4.63. The resistance is found using Equations 4.3, 5.14, 5.16 and integrating the resulting current density, as implied in Equation 5.20, which yields

$$R_p = \sigma_4 \Re \left\{ \sum_0^{\infty} d_n \sin \left(\frac{n\pi}{2} \right) \exp(-\lambda_4 l) \left(\mathcal{H}_n^4(h) - \frac{\epsilon_5}{\epsilon_4} \right) \right\} \quad (7.4)$$

where \Re denotes the real part and

$$\lambda_4 = \frac{n\pi}{s+1} \quad (7.5)$$

$$\mathcal{H}_n^4(h) = \sinh[\lambda_4(l-h) + \frac{\epsilon_5}{\epsilon_4} \cosh[\lambda_4(l-h)]] \quad (7.6)$$

Therefore, the model elements can be determined for any given frequency of operation.

Figure 7.1 displays the model elements (C_g , C_E , and R_p) as a function of frequency using the model data shown in Table 7.1. As in the previous chapter, the cell parameters were selected using the CHEMFET structure as a guide, and the cell dimensions were normalized with respect to the electrode's width. In addition, the model elements are all expressed on a unit length basis, with the capacitive elements values in Farads per centimeter (F/cm) and resistance values in ohms-centimeter (Ω -cm).

Table 7.1. Normalized data used for the frequency analysis

parameter	d	h	l	s	ϵ_{r2}	ϵ_{r3}	ϵ_{r4}	ϵ_{r5}	σ_2	σ_3	σ_4	σ_5
value	0.1	0.1	0.11	1	3.9	3.9	500	1	0	0	10^{-8}	0

Throughout the range of frequencies shown, the sensor coating behaves both as a good conductor and as a lossy dielectric. The transition between these two modes is illustrated in Figure 7.1, and it occurs when

$$\frac{\sigma_4}{\omega_p \epsilon_4} = 1 \quad (7.7)$$

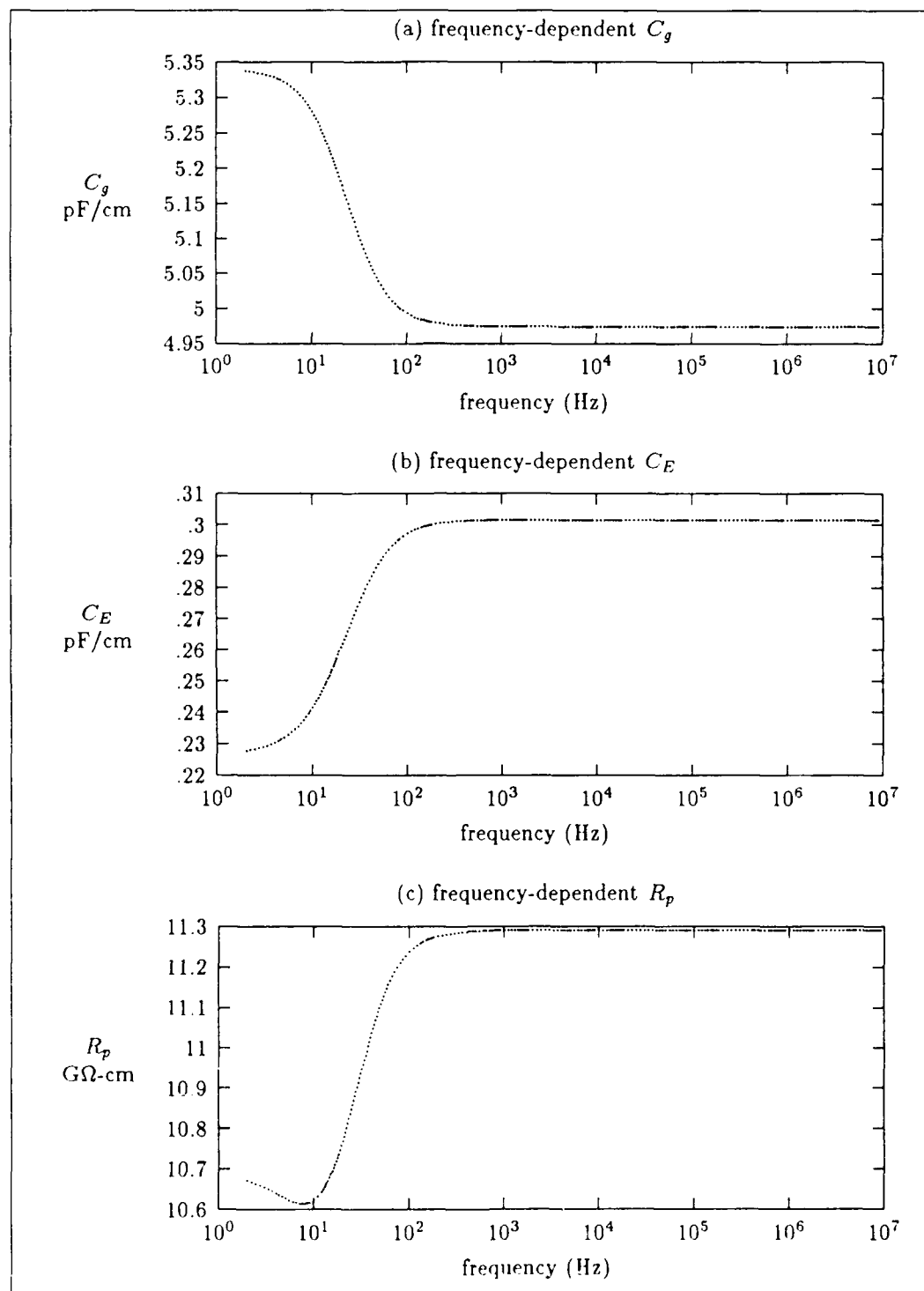


Figure 7.1. Behavior of the model elements versus frequency

where ω_p is the angular transition frequency of the sensor coating, which was discussed in Chapter III and defined as the frequency where the sensor coating transitions from a conductor to a lossy dielectric. From the data in Table 7.1, the angular transition frequency is

$$\omega_p = \frac{\sigma_4}{\epsilon_4} = \frac{10^{-8}}{500\epsilon_o} = 226.2 \text{ rad/sec} \quad (7.8)$$

which leads to an ordinary transition frequency (f_p) of

$$f_p = \frac{\omega_p}{2\pi} = 36 \text{ Hz} \quad (7.9)$$

This result is clearly in agreement with Figure 7.1. Element values far below the transition are suspect. The matrix which leads to the potential coefficients has a large condition number (10^8) at the lowest frequency shown, and the IMSL routine warns of ill-conditioning which suggests that the result may be inaccurate. This warning is given for any frequency of operation below 3 Hz with the data shown in Table 7.1. The ill-conditioning flag is dependent on the numerical precision of the computer. The FORTRAN programs were processed on an ELXSI System 6400 using single precision. The program was also processed using double precision, which resulted in identical output but no warnings.

In addition, the low frequency resistance value shown is approximately 10.6 G Ω -cm, while the calculated value using the resistive solution is 10.1 G Ω -cm. Figure 7.2 displays resistance versus frequency behavior using 50, 70, 100, 150, and 200 coefficients for the potential. Since the potential solution is a convergent infinite series, more coefficients should yield a better approximation to the solution; however, the processing time increases significantly to obtain these additional coefficients (for example it takes 15.7 CPU seconds to determine 50 coefficients, 25.3 sec for 70, 64.1 sec for 100, 194.3 sec for 150, and 423.9 sec for 200). With more coefficients, the low frequency resistance becomes smaller; with 200 coefficients, the low frequency resistance is approximately 10.2 G Ω -cm. However the ill-conditioning warning occurs at slightly higher frequencies when more terms are used, and with 200 coefficients, the IMSL routine provides warnings for frequencies below 15 Hz

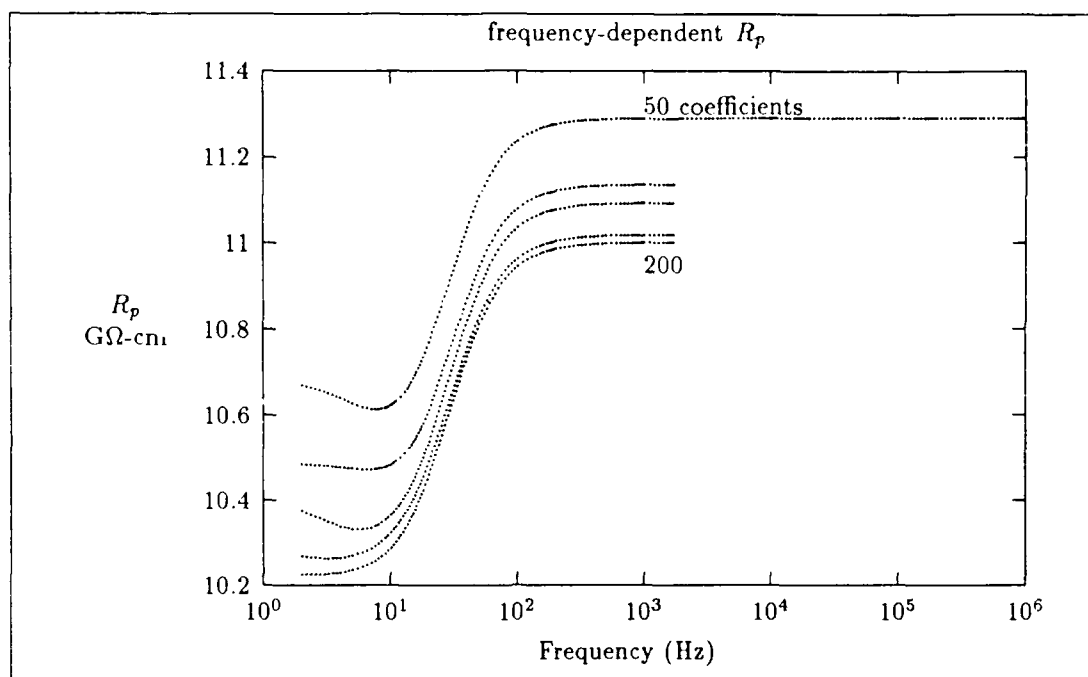


Figure 7.2. R_p versus frequency (50 through 200 coefficients)

(below 4 Hz for 70, 8 Hz for 100, and 11 Hz for 150). Therefore, the data is suspect for frequencies less than f_p . Figures 7.3 and 7.4 provide similar data for the model elements C_g and C_E .

7.1 Effects of Conductivity on the Frequency-Dependent Model Elements

Figure 7.5 displays the model element C_g versus frequency for $\sigma_4 = 10^{-7}$, 10^{-8} , and 10^{-10} Ω/cm , with the other model parameters shown in Table 7.1. Figures 7.6 and 7.7 depict similar results for the model elements C_E and R_p . For each model element, the curves are identical but shifted in frequency, which clearly illustrates the elements' dependence on the sensor coating's conductivity. For each conductivity value, an ill-conditioned warning was returned for the lowest frequency shown, which is consistent with the prior results and suggests a numerical instability at the lower frequencies.

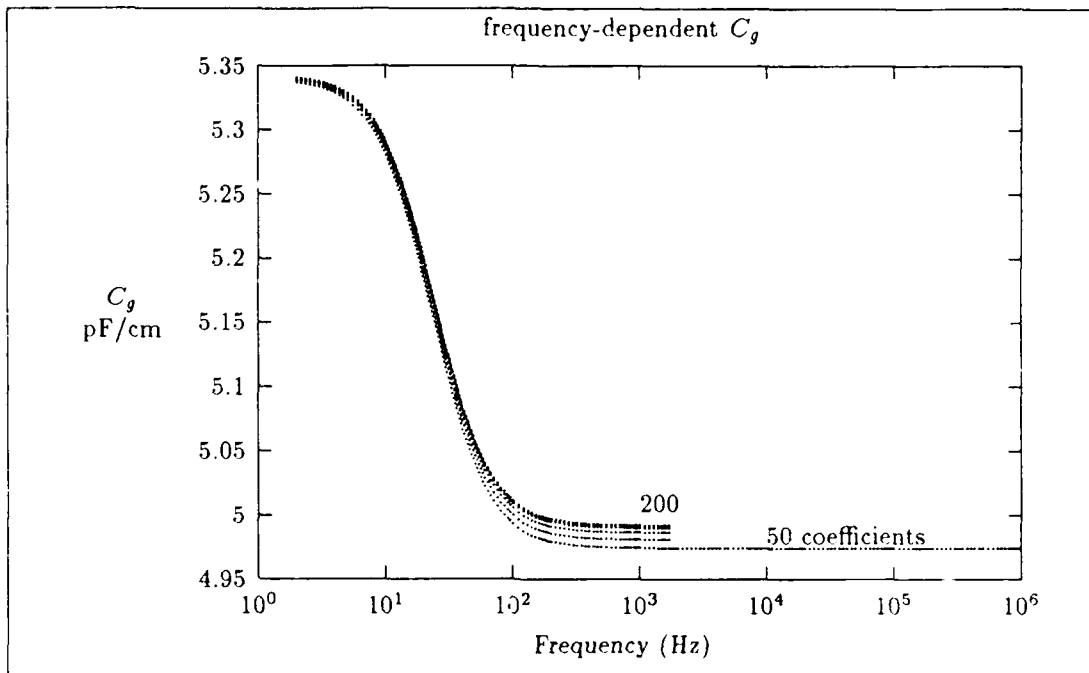


Figure 7.3. C_g versus frequency (50 through 200 coefficients)

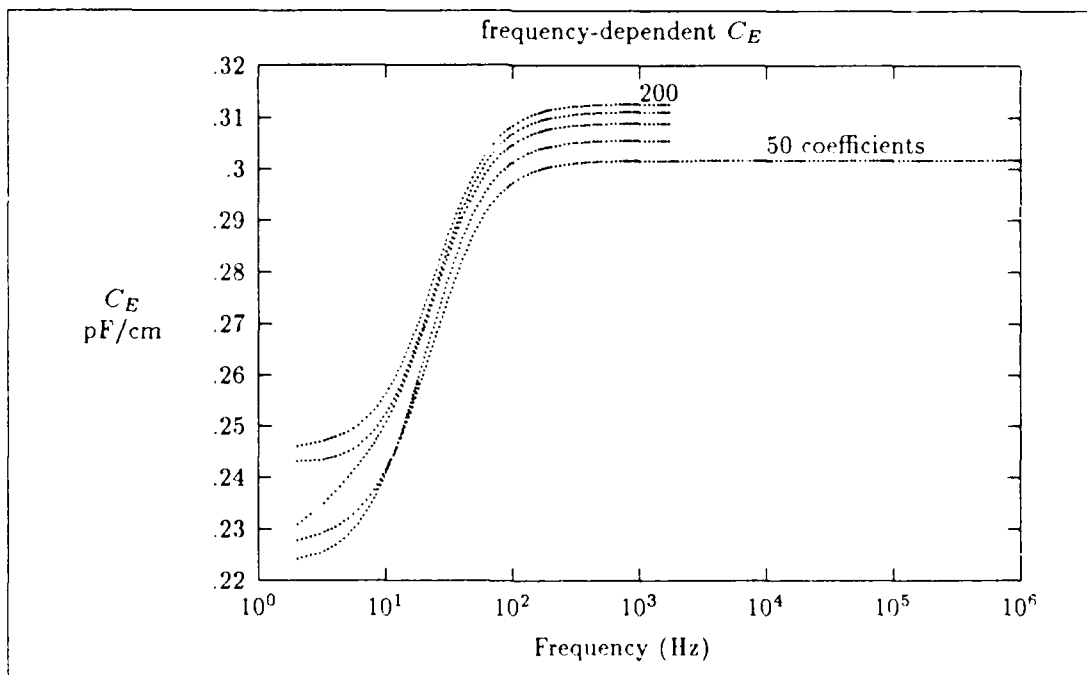


Figure 7.4. C_E versus frequency (50 through 200 coefficients)

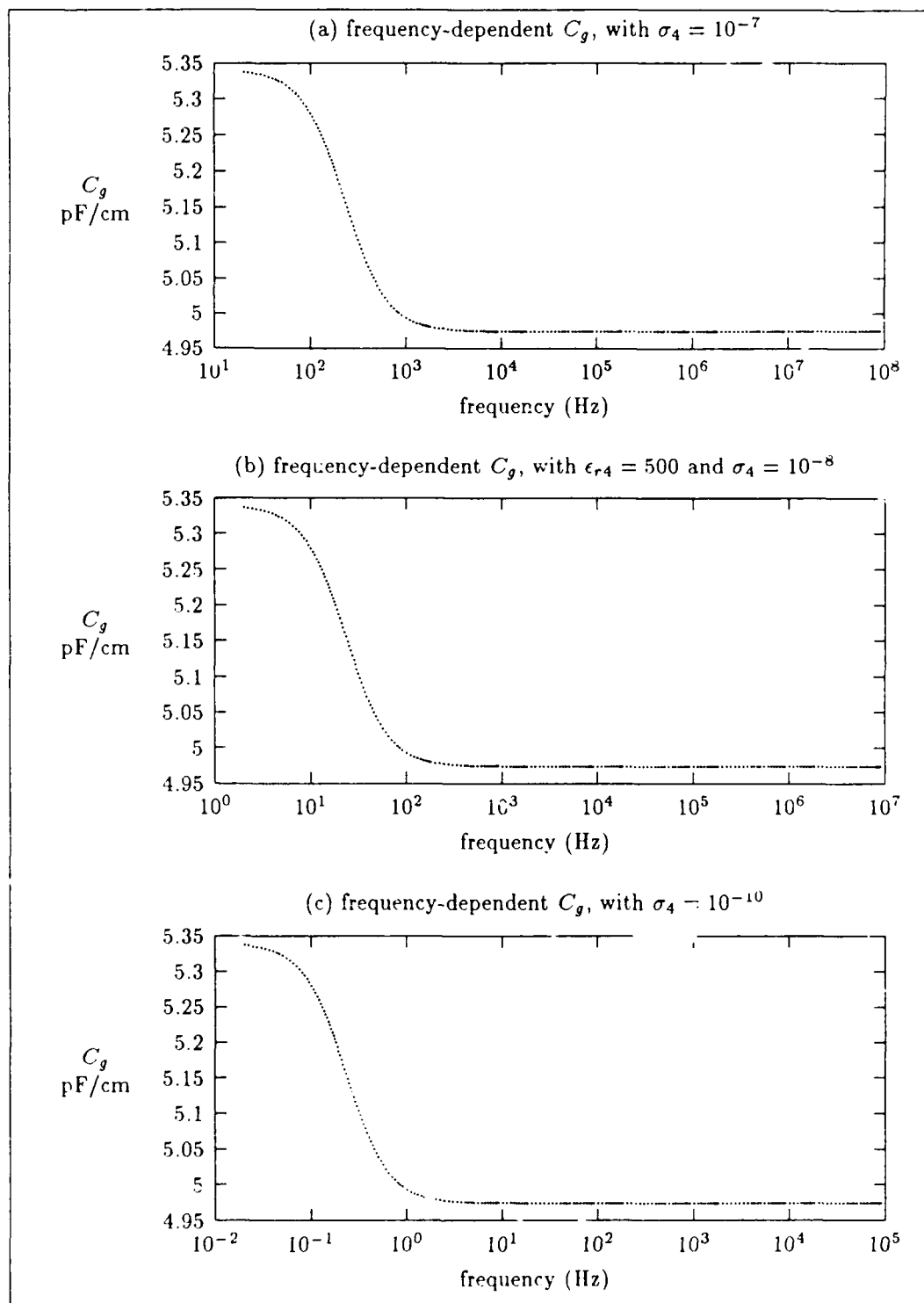


Figure 7.5. C_g versus frequency for $\sigma_4 = 10^{-7}$, 10^{-8} , and 10^{-10}

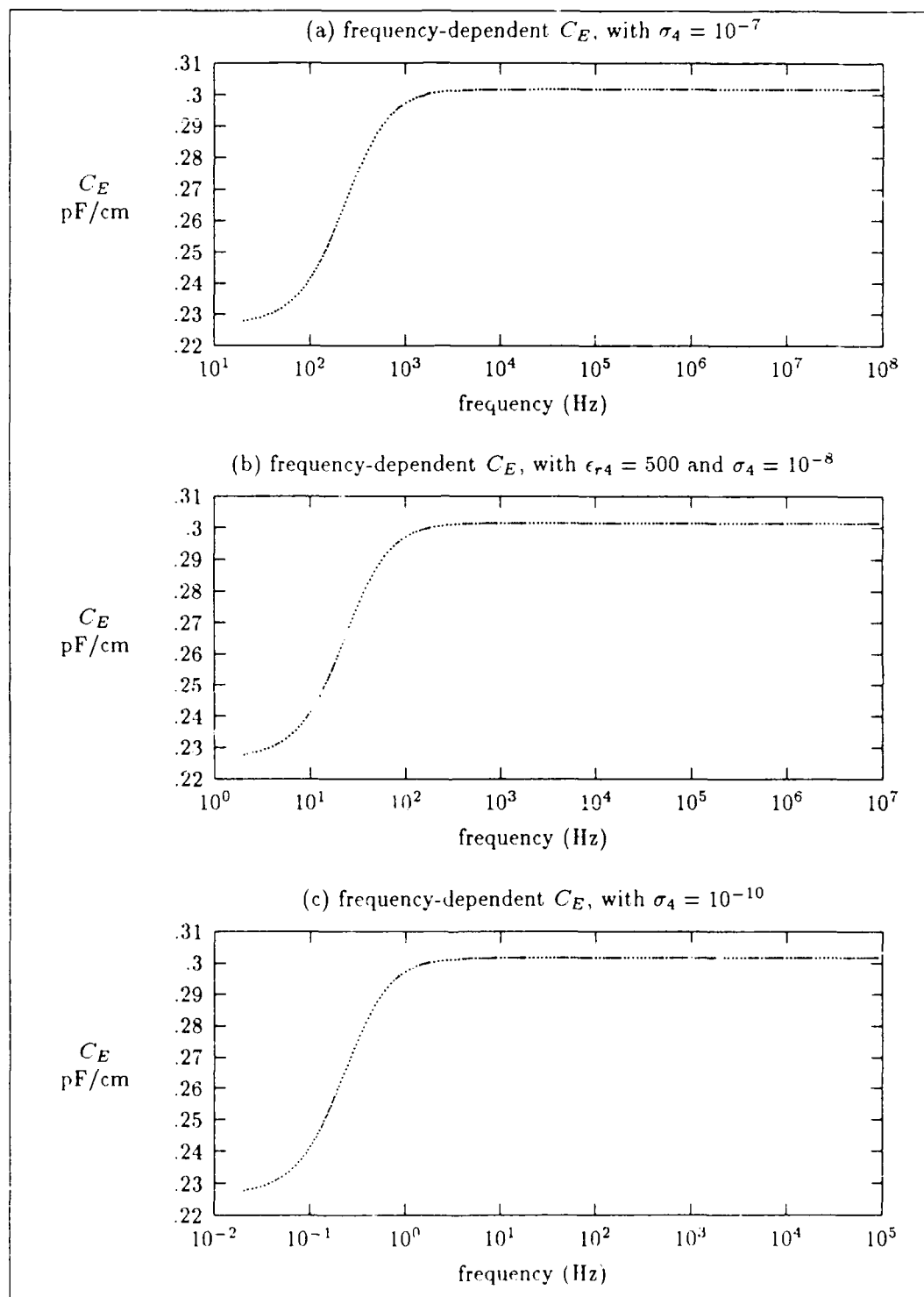


Figure 7.6. C_E versus frequency for $\sigma_4 = 10^{-7}$, 10^{-8} , and 10^{-10}

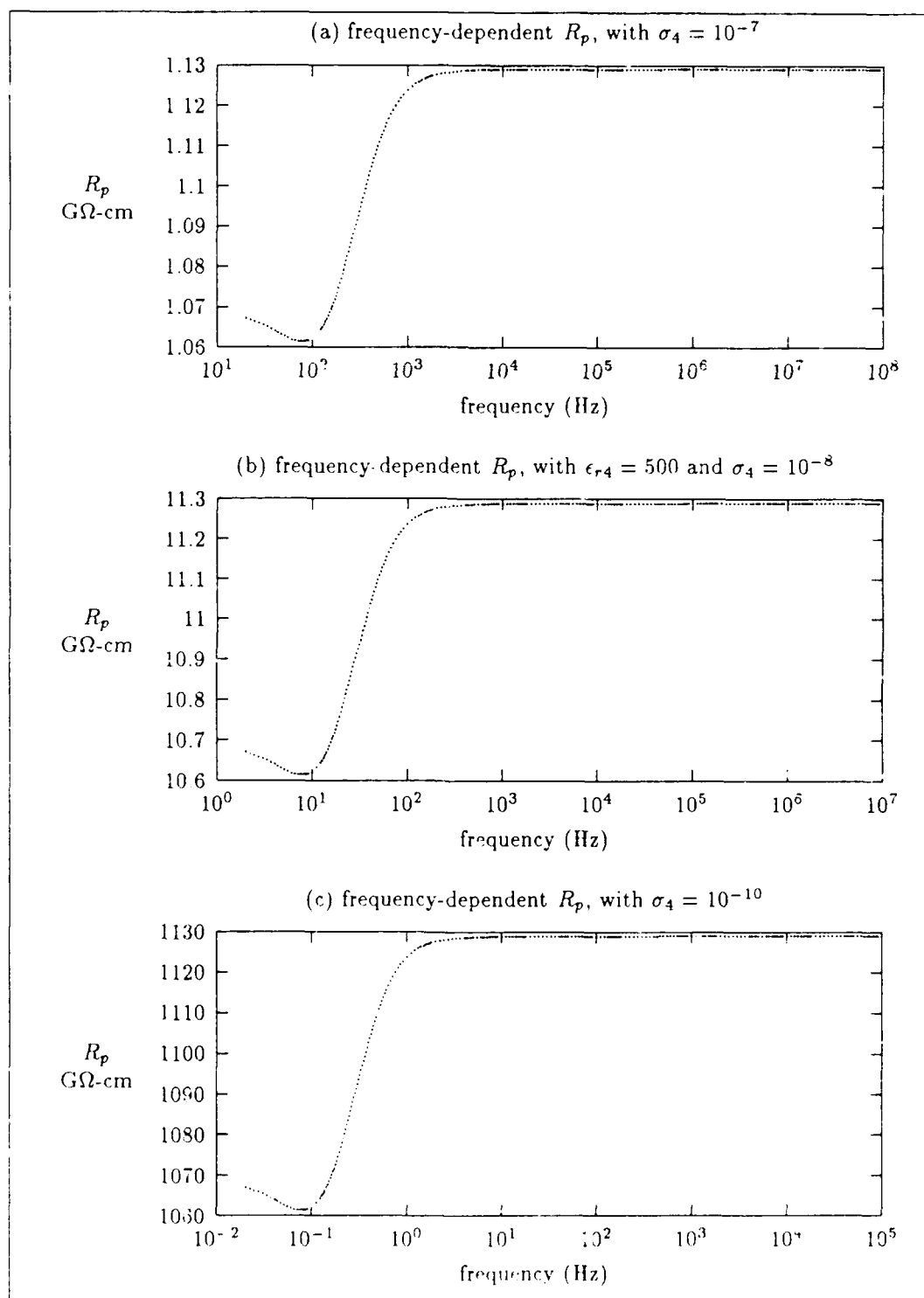


Figure 7.7. R_p versus frequency for $\sigma_4 = 10^{-7}$, 10^{-8} , and 10^{-10}

7.2 Effects of Permittivity on the Frequency-Dependent Model Elements

Figure 7.8 displays C_g for $\epsilon_{r_4} = 20, 500$, and 1300 , with the other model data shown in Table 7.1. Figures 7.9 and 7.10 depict similar graphs for C_E and R_p . While the curves for $\epsilon_{r_4} = 500$ and 1300 appear consistent with the results for the various conductivities considered, this is not the case for $\epsilon_{r_4} = 20$. For C_g , with $\epsilon_{r_4} = 20$, the curves again appear identical but shifted; however, this illusion is incorrect. For $\epsilon_{r_4} = 20$, the sensor coating transition frequency (f_p) is 900 Hz, and the curve should begin to depart from the high frequency value at approximately 6000 Hz (see C_E and R_p graphs for comparison); however, it appears to deviate from the high frequency value at approximately 300 Hz, which is where R_p reaches an intermediate peak between the high and low frequency values. In addition, C_E becomes negative (inductive?) at this same point. For $\epsilon_{r_4} = 20$, no ill-conditioned warnings were received for the frequencies shown, while ill-conditioning warnings were given for the first frequency shown for $\epsilon_{r_4} = 500$ and 1300 .

For $\epsilon_{r_4} = 20$, frequencies below f_p do not behave as expected for both C_E and R_p . While the general shape of C_E versus frequency appears valid (for frequencies above 100 Hz), the capacitance is not expected to become negative. This could be an indication of inductive behavior, or it could also be another indication that the element values predicted for lower frequencies are suspect (possibly invalid). For R_p , the intermediate peak between the low and high frequency values is interesting. It could signify a possible resonance, or again indicate the data is suspect at the lower frequencies. For comparison, graphs of the element values versus frequency are shown for $\epsilon_{r_4} = 100, 75$, and 50 in Figures 7.11, 7.12, and 7.13. For $\epsilon_{r_4} = 100$, an intermediate peak for R_p is observed, and C_E becomes negative for the lower frequencies. As the relative permittivity is reduced, the R_p peak becomes more pronounced, and C_E becomes more negative at the lower frequencies.

For frequencies above f_p , there is good agreement with all the element graphs, and the high frequency capacitance values match exactly the capacitance values found using the capacitive (high frequency) solution. The high frequency resistance can be determined by treating the sensor coating

as a lossy dielectric with the limit taken as $\omega \rightarrow \infty$. The current through the sensor coating layer can be found by integrating the electric field of the capacitive solution as was described for the resistance calculation in Chapter V. The resistance is then calculated from Ohm's law.

7.3 Comparison of the Model Element Values (High Frequency and Frequency-Dependent)

The graphs of the capacitive model elements versus frequency illustrated that the element values attained a high frequency limit; these values agree with the capacitive values found using the high frequency boundary conditions. The high frequency resistance was determined by considering the sensor coating as a lossy dielectric in the limit as $\omega \rightarrow \infty$ (where $\epsilon_4^* = \epsilon_4$), and calculating the current through the layer. While the complex permittivity solution leads to the more correct model element values for any finite frequency, this approach also increases the computational time needed to find the element values. Hence, if we use the high frequency values, we can reduce the computation time and still have reasonably accurate lumped element values for a given frequency range. To compare the high frequency values relative to the frequency-dependent values, the input and inter-terminal impedance are considered.

The inter-terminal impedance, Z_T , is the parallel combination of R_p and C_E . Since admittances in parallel add, the inter-terminal admittance, Y_T , is

$$Y_T = G_p + j\omega C_E \quad (7.10)$$

where $Y_T = 1/Z_T$, $G_p = 1/R_p$, $j = \sqrt{-1}$, and ω is the angular excitation frequency. The admittance to ground, Y_g is

$$Y_g = j\omega C_g \quad (7.11)$$

Let Z_N denote the impedance of the series combination of Z_T and Z_g , where $Z_g = 1/Y_g$. Then

$$Z_N = Z_T + Z_g \quad (7.12)$$

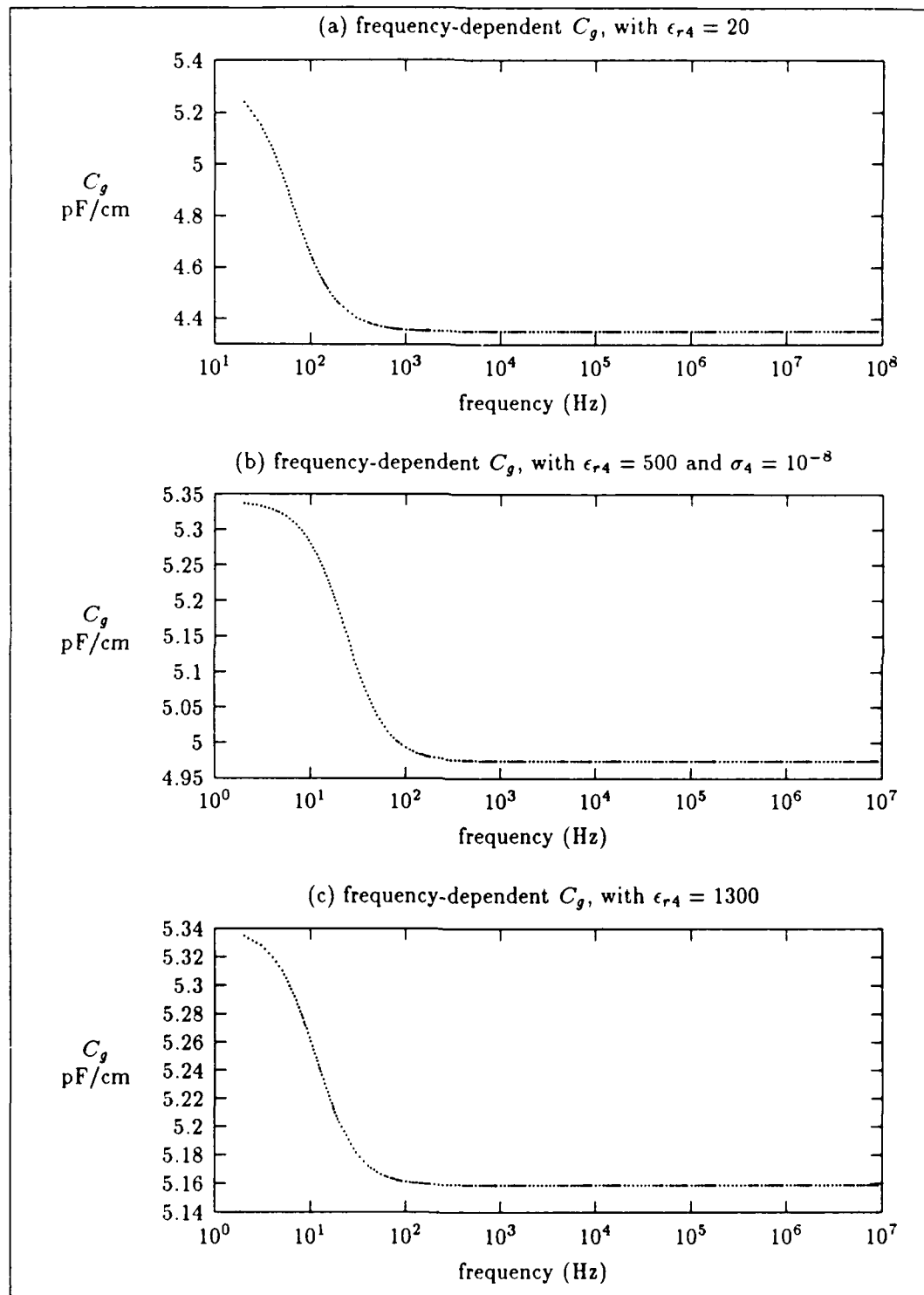


Figure 7.8. C_g versus frequency for $\epsilon_{r4} = 20, 500, 1300$

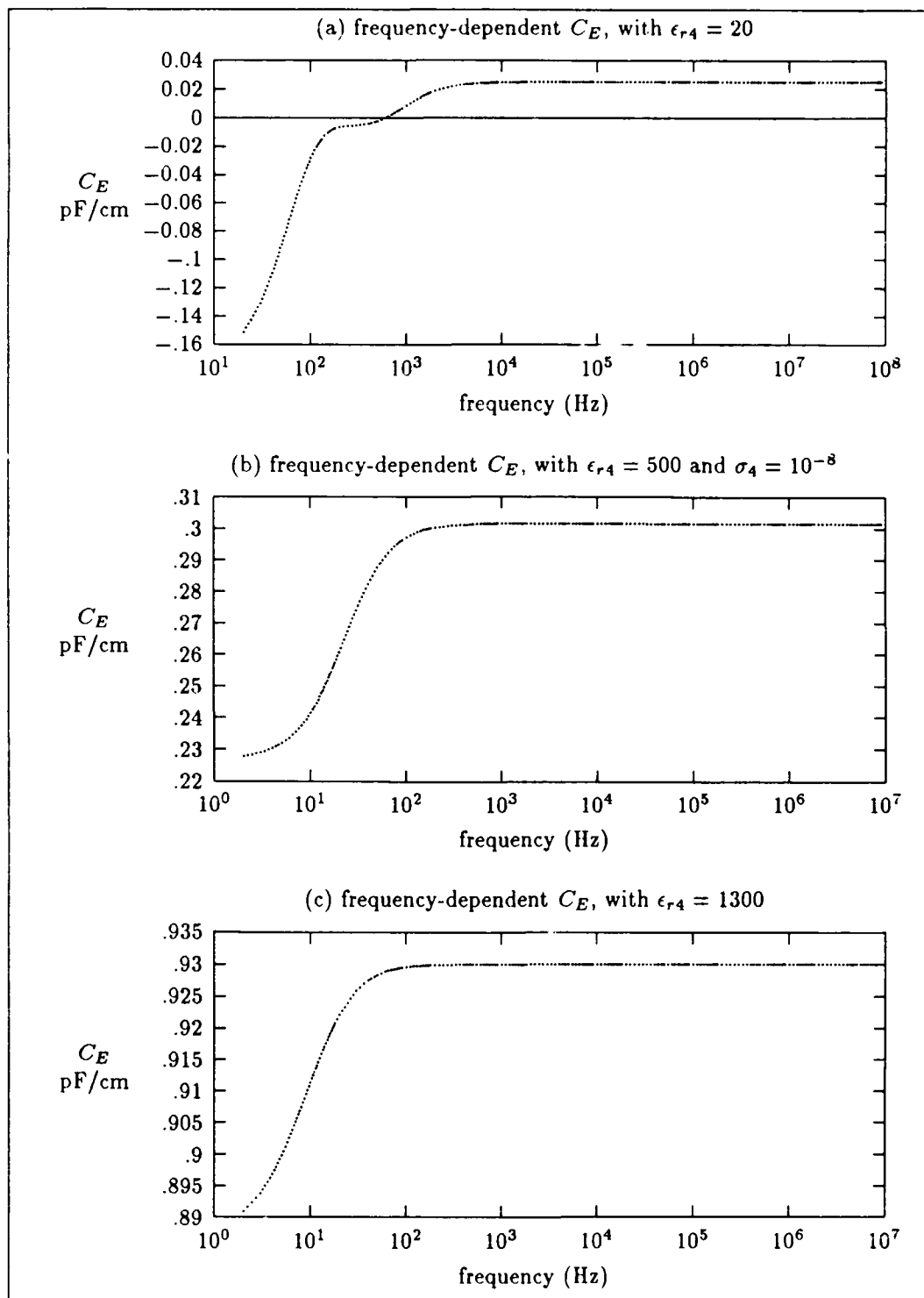


Figure 7.9. C_E versus frequency for $\epsilon_{r4} = 20, 500, 1300$

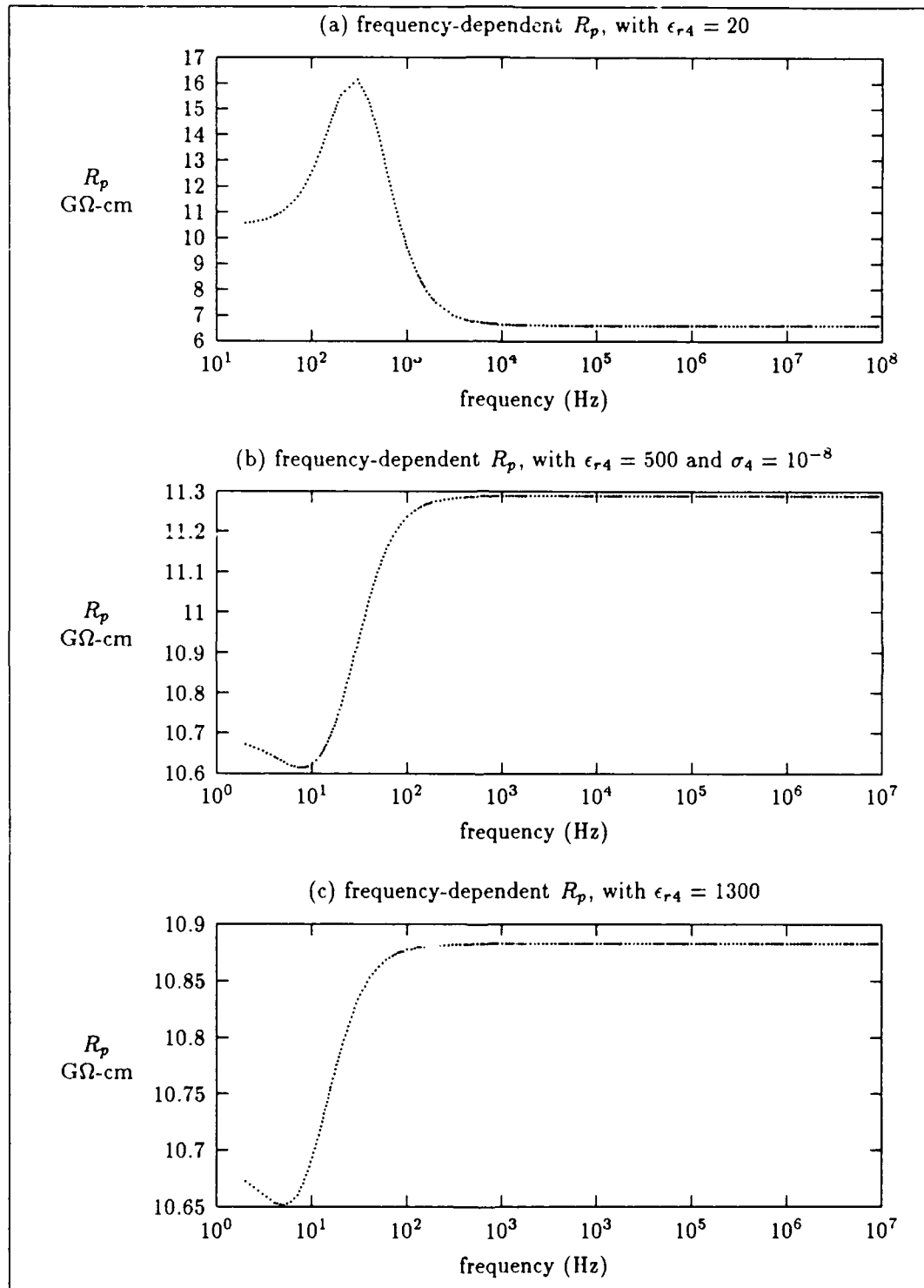


Figure 7.10. R_p versus frequency for $\epsilon_{r4} = 20, 500, 1300$

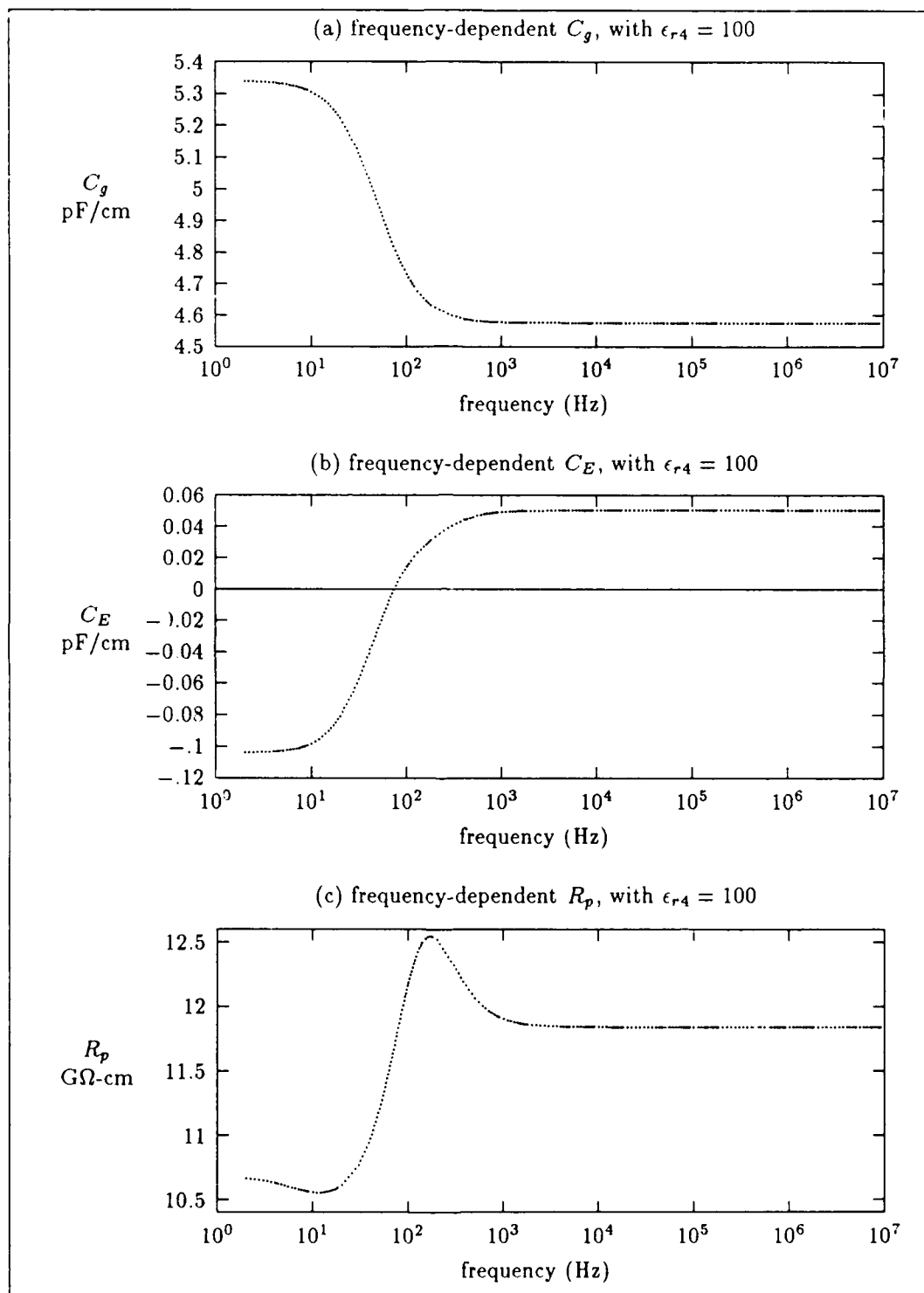


Figure 7.11. Model Elements versus frequency for $\epsilon_{r4} = 100$

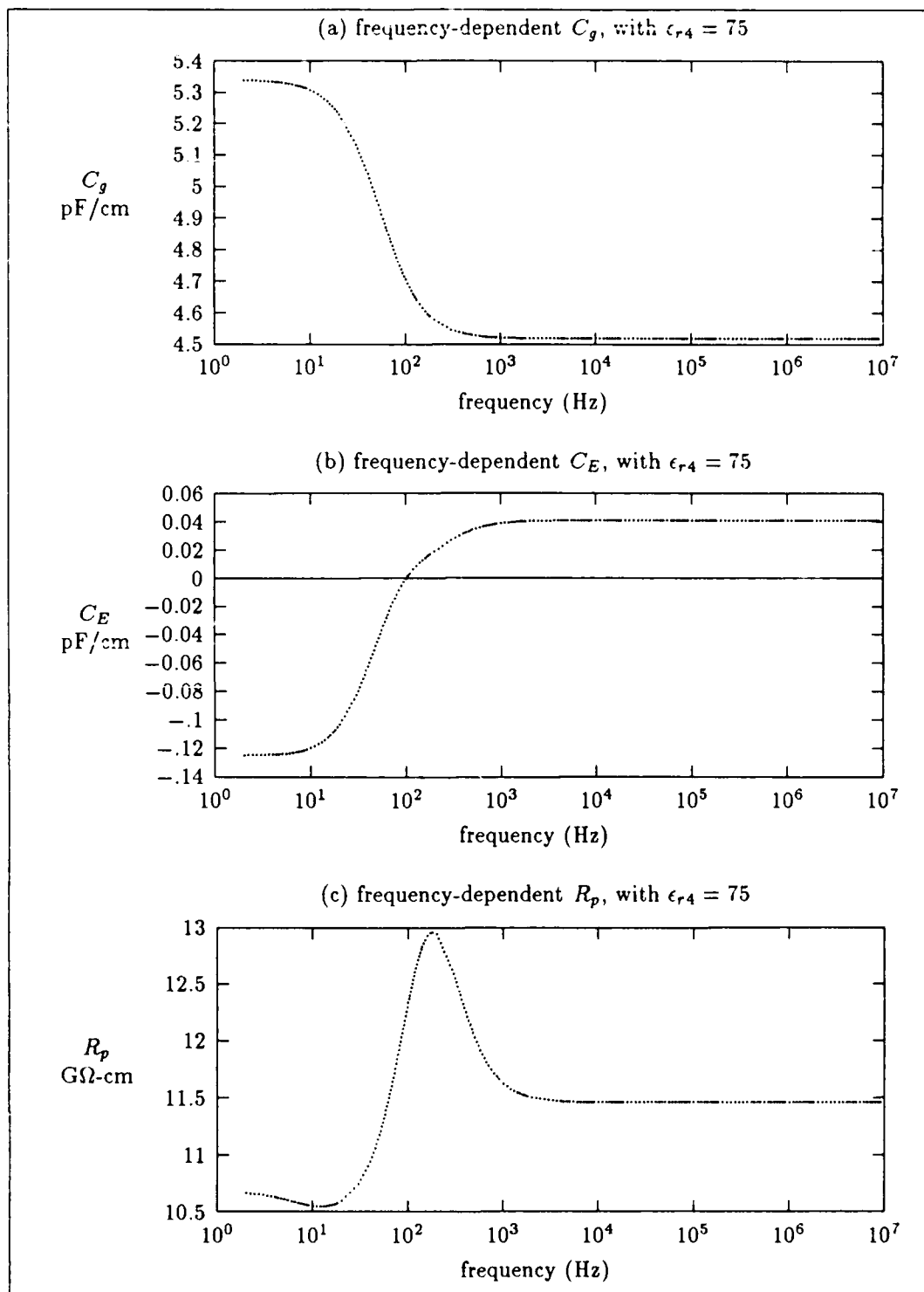


Figure 7.12. Model Elements versus frequency for $\epsilon_{r4} = 75$

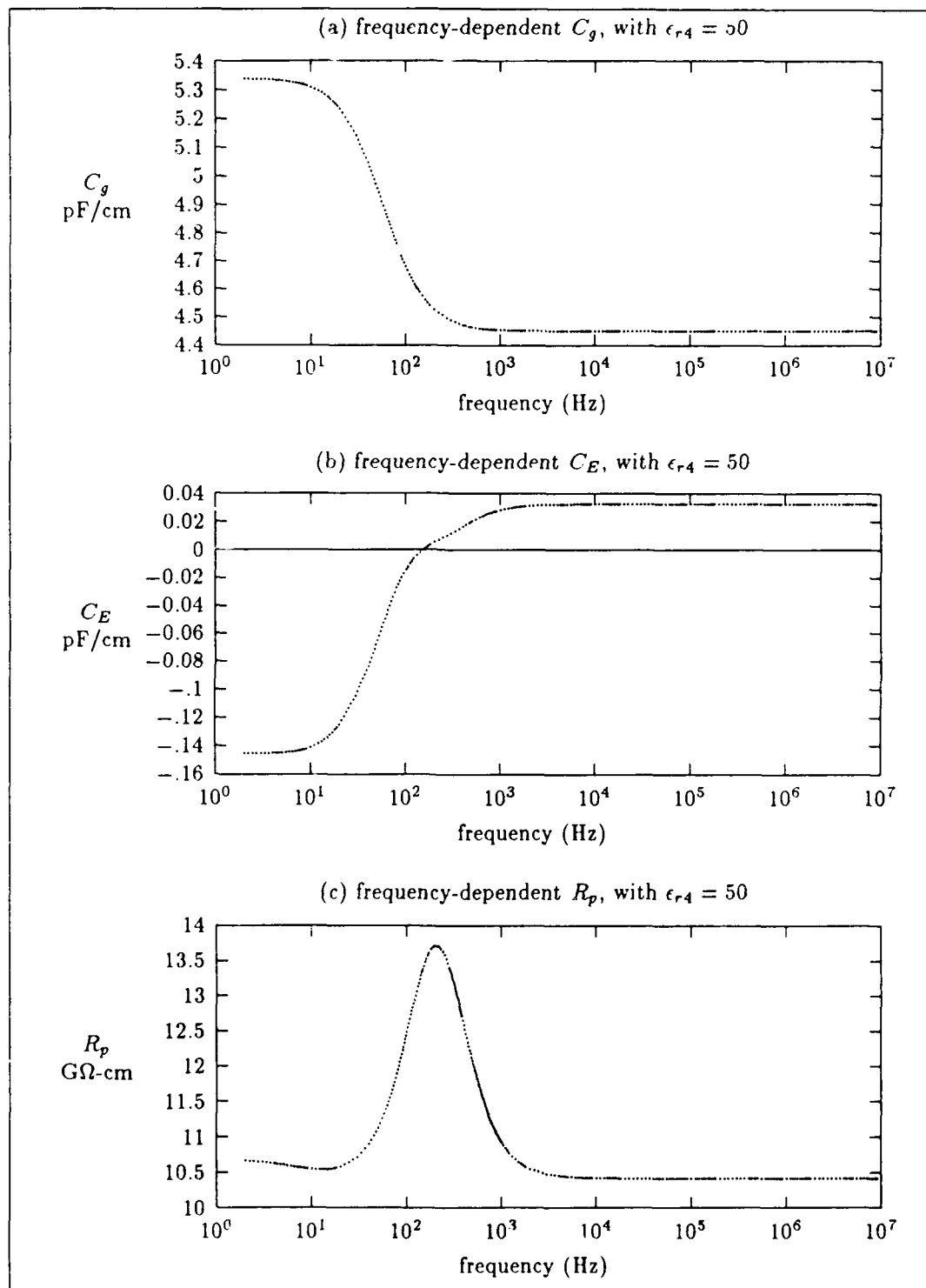


Figure 7.13. Model Elements versus frequency for $\epsilon_{r4} = 50$

The input impedance, Z_{in} , is the impedance at the input terminals of the device, which is the parallel combination of Z_N and Z_g . Using the fact that admittances in parallel add, yields

$$Y_{in} = Y_N + Y_g \quad (7.13)$$

where $Y_{in} = 1/Z_{in}$.

Figure 7.14 displays the input impedance of the interdigitated electrode sensor structure (both magnitude and phase), using both the frequency-dependent model element values and the high frequency values. The two curves are identical at the higher frequencies, and they only deviate at the lower frequencies (as expected). Even at the lower frequencies (near f_p), the input impedance has only a small deviation (in both magnitude and phase) relative to using the different values for the model elements.

Figure 7.15 displays the inter-terminal impedance of the interdigitated electrode sensor structure (both in magnitude and phase), relative to using both the frequency-dependent values and the high frequency values. Again the two curves are nearly identical, with only a relatively small deviation at the lower frequencies.

2.1 Analysis of the Frequency-Dependent Results

In conclusion, the model element values found using the high frequency (capacitive) boundary conditions provide a valid model for $f > f_p$. While more accurate model element values can be obtained using frequency analysis with a complex dielectric constant, the additional computation time may not be beneficial.

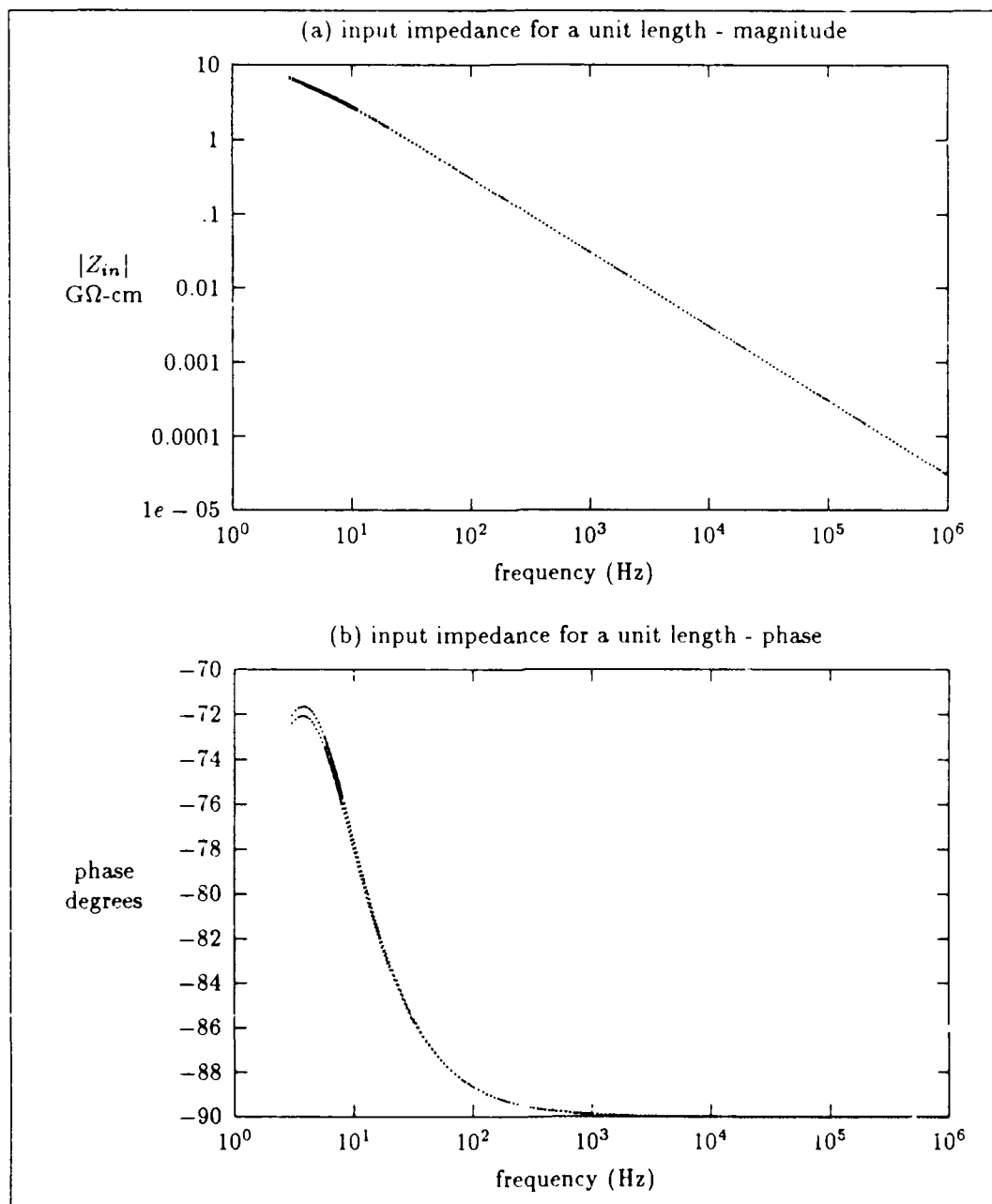


Figure 7.14. Input impedance using frequency-dependent and high frequency elements values

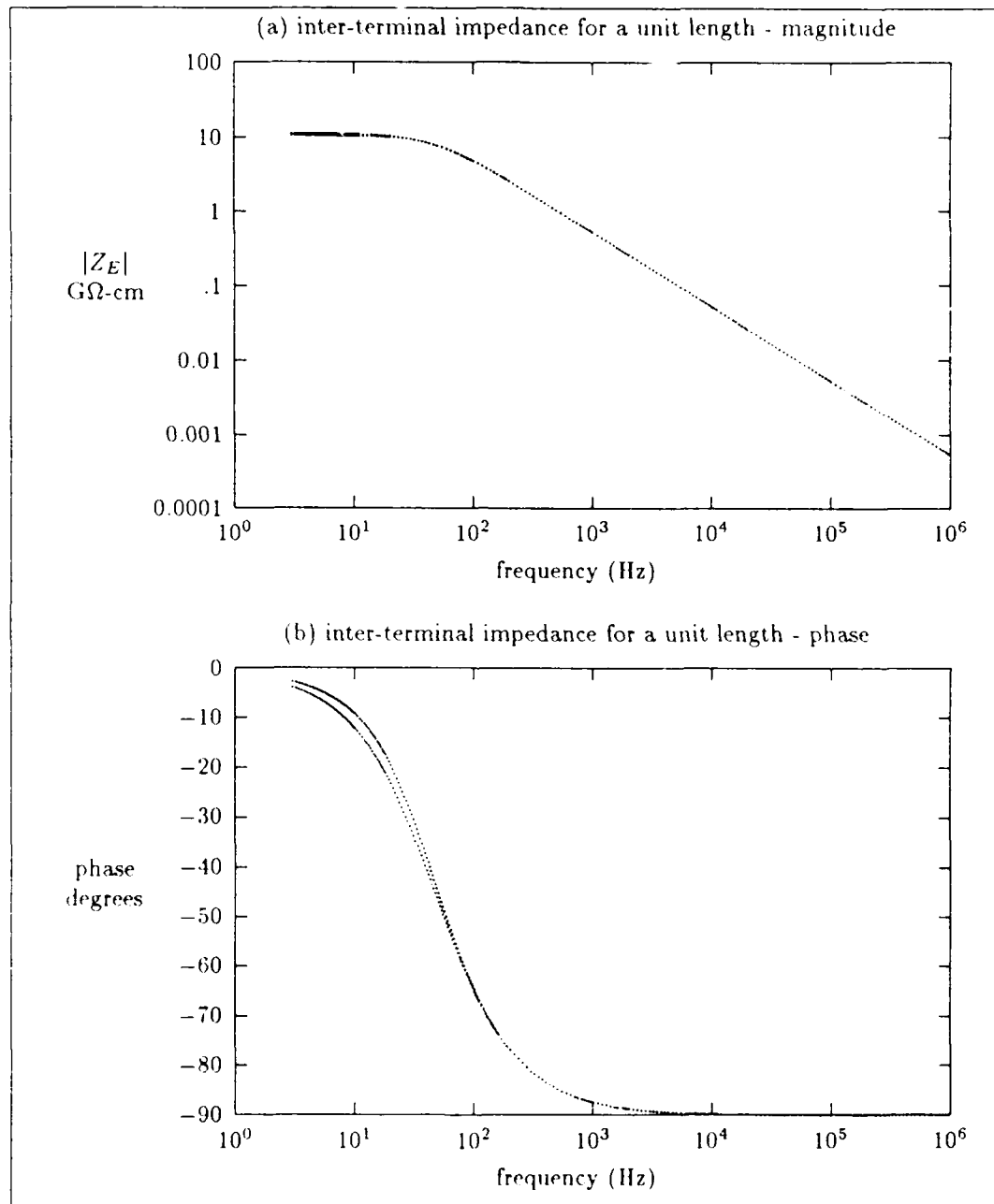


Figure 7.15. Inter-terminal impedance using frequency-dependent and high frequency elements values

VIII. Conclusion

8.1 Summary

A lumped-parameter electrical model for the interdigitated electrode sensor structure has been developed. Three elements have been identified; they are a capacitance from each of the two electrodes relative to ground (C_g), a capacitance between electrodes (C_E), and a resistance through the sensor coating (R_p). The elements were determined from the electric field within the structure by first solving for the potential distribution.

A periodic cell was established to represent the configuration of electrodes, since the interdigitated electrode sensor structure contains a repetitive pattern in the plane transverse to the structure's length. Five layers within the cell were then defined. The interdigitated electrode sensor structure was then reduced to a two-dimensional problem using a transverse electromagnetic (TEM) wave analysis and limiting the model to a frequency range where the potential is essentially constant along the structure's length. This situation also resulted in the potential satisfying Laplace's equation in the transverse plane. Boundary conditions at the interfaces between layers were then developed for the low and high frequency cases, which correspond to the conditions that the sensor coating is either a good conductor, or a lossy dielectric, respectively.

The capacitive elements were determined using boundary conditions on the potential based on the high frequency limit. A Fourier series representation of the potential was established for each layer in the cell, with the Fourier coefficients determined by the boundary conditions. These coefficients were approximated numerically by truncating the infinite Fourier series. From the potential, the electric field was found, along with the charge enclosed on an electrode. The capacitance values were determined from the charge calculations using Weeks' method [17].

The resistive element was determined using boundary conditions for the potential based on a low frequency limit. Again, a Fourier series representation of the potential was established for each region within the layer, and the Fourier coefficients were obtained from the boundary conditions

at the interfaces between regions. These coefficients were also estimated by truncating the infinite Fourier series. From the potential, the electric field and current density were found through the partially conductive sensor coating layer. The resistance was finally calculated using Ohm's law

The capacitive and resistive solutions were illustrated using specific cell parameter values that would highlight certain aspects of the solution. At this point, the investigation shifted from a general nature to a particular case focusing on the dimensional and material values closely related to the chemically-sensitive field-effect transistor (CHEMFET). Then, the capacitive and resistive elements were calculated for a range of structural dimensions, sensor coating permittivities, and sensor coating conductivities. The results were presented, and they revealed that all the model elements were sensitive to the variable electrical properties of the thin sensor coating layer covering the electrodes. In addition the dependence of the model elements on each of the structural dimensions and material properties was illustrated.

Using a complex permittivity, the frequency-dependent lumped parameters were obtained; these results agreed with the high frequency capacitive, and low frequency resistive values in the appropriate limits. From the frequency plots shown in Chapter VII, the transition from the high frequency to the low frequency values was illustrated, corresponding to the sensor coating's transition from a conductor to a lossy dielectric. For frequencies larger than the sensor coating's transition point, the numerical results showed that all element values approach a high frequency value over a range of sensor coating permittivities and conductivities. At frequencies below the transition, the numerical results are suspect due to a possible numerical instability in the solution. In general, the results at the lower frequencies do not behave as expected. The potential solution for the DC (direct current) case must satisfy different boundary conditions at the sensor coating layer interfaces; this leads to a potential solution with a completely different form. Since the sensor coating modelled herein (the CHEMFET's phthalocyanine polymer) has a fairly low transition frequency

(below 1000 Hz), the concerns at the lower frequencies should not represent a significant limitation for the model.

8.2 Significance of the Thesis

While particular values for the interdigitated electrode structure have been calculated and graphically displayed, the main benefit of this research is in the flexibility of the model to handle a variety of model parameters within the investigated limits of the analysis. In this light, the model developed in this thesis becomes a powerful tool to further investigate interdigitated electrode structures and their use in integrated circuit sensors. As both Lee [14] and Wiseman [18] recommend, further research in the integrated circuit sensors requires a rigorous analysis of the interdigitated electrode structure. The model developed in this thesis is intended to help satisfy this need.

8.3 Recommendations for Future Research

The ultimate objective of the integrated sensor is to detect electrical variations caused by an external event. Therefore, any variations due to internal events should be minimized, or negated if possible. The depletion layer capacitance (discussed in Chapter III) caused by a metal-insulator-semiconductor contact presents an undesirable, frequency-dependent internal variation which could hinder the sensor's fundamental objective. Therefore, this unwanted capacitance should be eliminated by introducing a suitable ground plane above the semiconductor substrate. A layer of polysilicon, or other appropriate material, can establish such a ground plane to match the simplified model developed in this thesis. Hence, an integrated circuit sensor using the interdigitated electrode sensor structure should incorporate this additional layer below the structure's insulating layer.

The results presented in this thesis also illustrate the importance of the sensor coating's permittivity and conductivity on the overall results. Unfortunately, these properties for the sensor

coating used in the CHEMFET are not well established. While the electrical properties are variable, the range of this variation should be determined to some reasonable degree of accuracy. Only then, will an acceptable model of the device be available.

In addition, this research considered a particular configuration of the interdigitated electrode structure. Specifically, the thin sensor coating layer was limited to the region above the electrodes. To further model the CHEMFET, a multi-layered combination of P-glass, polymer, and air should be considered between the electrodes. In fact, different configurations of all the layers within the structure should be explored. The solution technique employed in this thesis should be readily adaptable to any rectangular geometry. Alternate methods may have to be used for more complex geometries, such as the finite difference method used by Lee [14].

Finally, the unexpected behavior of the model element values at low frequencies, when complex permittivity is considered, should be further investigated. This thesis attempted to extend the high frequency solution to much lower frequencies. Another possible approach would be to determine the potential everywhere in the periodic cell at DC, and then extend this solution, up in frequency, to the sensor coating's transition frequency. For the DC solution, the potential distribution is determined first within the sensor coating layer, as discussed in Chapter V. The potentials in the other layers are determined using the calculated boundary potential at the sensor coating interfaces as boundary conditions for determining the potential in the dielectric layers. At frequencies below the sensor coating's transition frequency, the potential within the cell can be considered as a perturbation of the DC solution, which will require a new analysis and solution for the perturbation term. This approach should easily model the behavior at the lower frequencies, and, together with the results of this thesis, provide a complete frequency-dependent model of the interdigitated electrode sensor structure.

Appendix A. Detailed Capacitive Potential Solution

To determine the capacitive elements of the model, the potential distribution within the simplified periodic cell is determined for the case when the sensor coating is considered a dielectric (high frequency limit on the boundary conditions for the sensor coating). First, a Fourier series representation of the potential functions of each layer are found using unknown constants. These potential functions satisfy all boundary conditions except those at the interfaces between layers. Then, the Fourier coefficients are determined by enforcing the boundary conditions between the layers within the cell. A diagram of the simplified periodic cell is depicted in Figure A.1.

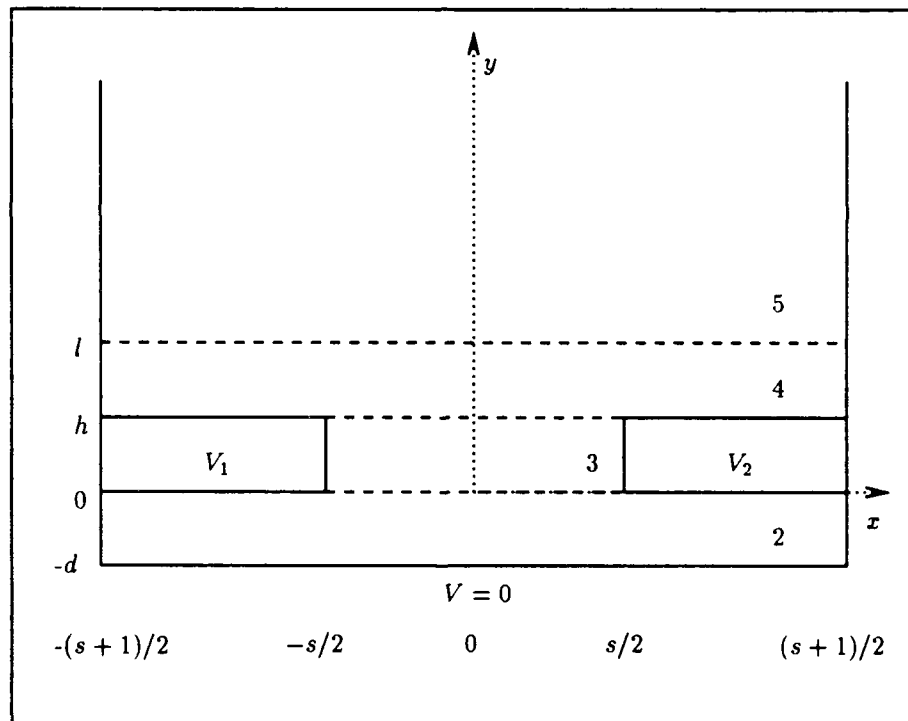


Figure A.1. Problem diagram for the detailed capacitive solution

A.1 Potential in Layer 2

In layer 2, the voltage potential, ϕ_2 , satisfies (see Figure A.1)

$$\nabla^2 \phi_2 = 0 \quad (\text{A.1})$$

$$\frac{\partial \phi_2}{\partial x} \left(\pm \frac{s+1}{2}, y \right) = 0 \quad (\text{A.2})$$

$$\phi_2(x, -d) = 0 \quad (\text{A.3})$$

For ϕ_2 , we seek a solution of the form

$$\phi_2 = \Psi_2(x) \Phi_2(y) \quad (\text{A.4})$$

Using Equation A.4 in Equation A.1 yields

$$\Psi'' \Phi + \Psi \Phi'' = 0 \quad (\text{A.5})$$

where Ψ'' denotes $\partial^2 \Psi / \partial x^2$ and Φ'' denotes $\partial^2 \Phi / \partial y^2$. Dividing by $\Psi \Phi$ (to separate the variables) yields

$$\frac{\Psi''}{\Psi} = -\frac{\Phi''}{\Phi} = -\lambda_2^2 \quad (\text{A.6})$$

where λ_2 is the separation constant or eigenvalue in layer 2. First, let us resolve $\Psi(x)$

$$\Psi'' + \lambda_2^2 \Psi = 0 \quad (\text{A.7})$$

To simplify the formulation, let

$$\tilde{x} = x + \frac{s+1}{2} \quad (\text{A.8})$$

then $\Psi(x) = \tilde{\Psi}(\tilde{x})$, and $\partial^2 \Psi / \partial x^2 = \partial^2 \tilde{\Psi} / \partial \tilde{x}^2$. Thus,

$$\tilde{\Psi}'' + \lambda_2^2 \tilde{\Psi} = 0 \quad (\text{A.9})$$

or, we may write

$$\tilde{\Psi} = A \cos(\lambda_2 \tilde{x}) + B \sin(\lambda_2 \tilde{x}) \quad (\text{A.10})$$

Taking the first derivative yields

$$\tilde{\Psi}' = -A\lambda_2 \sin(\lambda_2 \tilde{x}) + B\lambda_2 \cos(\lambda_2 \tilde{x}) \quad (\text{A.11})$$

Enforcing Equation A.2 on Equation A.11 yields

$$\tilde{\Psi}'(0) = B\lambda_2 = 0 \quad (\text{A.12})$$

or $B = 0$. Also from Equation A.2

$$\tilde{\Psi}'(s+1) = -A\lambda_2 \sin[\lambda_2(s+1)] = 0 \quad (\text{A.13})$$

This condition forces the eigenvalue λ_2 to be

$$\lambda_2 = \frac{n\pi}{s+1}, \text{ for } n = 0, 1, 2, \dots \quad (\text{A.14})$$

Thus,

$$\tilde{\Psi}_n(\tilde{x}) = A_n \cos\left(\frac{n\pi\tilde{x}}{s+1}\right) \quad (\text{A.15})$$

or, using the original x variable, the eigenfunction is

$$\Psi_n(x) = A_n \cos\left[n\pi\left(\frac{x}{s+1} + \frac{1}{2}\right)\right] \quad (\text{A.16})$$

For $\Phi(y)$, the equations can be simplified by letting

$$\tilde{y} = y + d \quad (\text{A.17})$$

Consequently, $\tilde{\Phi}(\tilde{y}) = \Phi(y)$, and $\partial^2 \tilde{\Phi} / \partial \tilde{y}^2 = \partial^2 \Phi / \partial y^2$. Then from Equation A.6

$$\tilde{\Phi}_0'' = 0 \quad \text{for } n = 0 \quad (\text{A.18})$$

$$\tilde{\Phi}_n'' - \lambda_2^2 \tilde{\Phi}_n = 0 \quad \text{for } n \neq 0 \quad (\text{A.19})$$

or

$$\tilde{\Phi}_0 = C_0 y + D_0 \quad (\text{A.20})$$

$$\tilde{\Phi}_n = C_n \cosh(\lambda_2 y) + D_n \sinh(\lambda_2 y) \quad (\text{A.21})$$

Enforcing Equation A.3 yields ($y = -d$ implies that $\tilde{y} = 0$)

$$\tilde{\Phi}_0(0) = D_0 \quad (\text{A.22})$$

$$\tilde{\Phi}_n(0) = C_n \quad (\text{A.23})$$

or, $D_0 = C_n = 0$. Thus,

$$\tilde{\Phi}_0(\tilde{y}) = C_0 \tilde{y} \quad (\text{A.24})$$

$$\tilde{\Phi}_n(\tilde{y}) = D_n \sinh(\lambda \tilde{y}) \quad (\text{A.25})$$

or

$$\Phi(y) = \begin{cases} C_0(y + d) & \text{for } n = 0 \\ D_n \sinh[\lambda_2(y + d)] & \text{for } n \neq 0 \end{cases} \quad (\text{A.26})$$

Using Equations A.16 and A.26 in A.4 yields the final form of the potential in layer 2 as

$$\phi_2 = a_0(y + d) + \sum_{n=1}^{\infty} a_n \sinh[\lambda_2(y + d)] \psi_n^2(x) \quad (\text{A.27})$$

where

$$a_0 = A_0 \cdot C_0 \quad (\text{A.28})$$

$$a_n = A_n \cdot D_n \quad (\text{A.29})$$

$$\lambda_2 = \frac{n\pi}{s+1} \quad (\text{A.30})$$

$$\psi_n^2(x) = \cos \left[n\pi \left(\frac{x}{s+1} + \frac{1}{2} \right) \right] \quad (\text{A.31})$$

The superscript in $\phi_n^2(y)$ denotes layer 2 instead of the conventional squared notation.

A.2 Potential in Layer 3

Layer 3 is located between the two fingers with $(0 < y < h)$ and $(-s/2 < x < s/2)$. Referring to Figure A.1, the potential in layer 3, ϕ_3 , satisfies

$$\nabla^2 \phi_3 = 0 \quad (\text{A.32})$$

$$\phi_3\left(-\frac{s}{2}, y\right) = V_1 \quad (\text{A.33})$$

$$\phi_3\left(+\frac{s}{2}, y\right) = V_2 \quad (\text{A.34})$$

For the potential, we seek a solution of the form

$$\phi_3(x, y) = v_3(x) + \omega_3(x, y) \quad (\text{A.35})$$

where $v_3(x)$ is selected to satisfy Laplace's equation and the left and right boundary conditions.

Let us consider the following function for $v_3(x)$

$$v_3(x) = \frac{V_2 - V_1}{s}x + \frac{V_2 + V_1}{2} \quad (\text{A.36})$$

This function satisfies Equations A.32, A.33 and A.34. Thus, $\omega_3(x, y)$ must satisfy

$$\nabla^2 \omega_3 = 0 \quad (\text{A.37})$$

$$\omega_3(-s/2, y) = 0 \quad (\text{A.38})$$

$$\omega_3(+s/2, y) = 0 \quad (\text{A.39})$$

To solve $\omega_3(x, y)$, we seek a solution of the form

$$\omega_3(x, y) = \Psi_3(x)\Phi_3(y) \quad (\text{A.40})$$

Using Equation A.40 in Equation A.37 yields

$$\Psi''\Phi + \Psi\Phi'' = 0 \quad (\text{A.41})$$

where $\Psi'' = \partial^2 \Psi / \partial x^2$, and $\Phi'' = \partial^2 \Phi / \partial y^2$. Thus,

$$\frac{\Psi''}{\Psi} = -\frac{\Phi''}{\Phi} = -\lambda_3^2 \quad (\text{A.42})$$

where λ_3 is the separation constant or eigenvalue for layer 3. The analysis can be simplified by letting

$$\tilde{x} = x + \frac{s}{2} \quad (\text{A.43})$$

Then $\tilde{\Psi}(\tilde{x}) = \Psi(x)$, and $\partial^2 \tilde{\Psi} / \partial \tilde{x}^2 = \partial^2 \Psi / \partial x^2$, so

$$\tilde{\Psi}'' + \lambda_3^2 \tilde{\Psi} = 0 \quad (\text{A.44})$$

or

$$\tilde{\Psi}(\tilde{x}) = A \cos(\lambda_3 \tilde{x}) + B \sin(\lambda_3 \tilde{x}) \quad (\text{A.45})$$

From Equation A.38

$$\tilde{\Psi}(0) = A = 0 \quad (\text{A.46})$$

From Equation A.39

$$\tilde{\Psi}(s) = B \sin(\lambda_3 s) = 0 \quad (\text{A.47})$$

or

$$\lambda_3 = \frac{n\pi}{s}, \text{ for } n = 0, 1, 2, \dots \quad (\text{A.48})$$

Hence the eigenfunction for layer 3 is

$$\tilde{\Psi}_{3n}(\tilde{x}) = B_n \sin\left(\frac{n\pi \tilde{x}}{s}\right) \quad (\text{A.49})$$

$$\Psi_{3n}(x) = B_n \sin\left[n\pi \left(\frac{x}{s} + \frac{1}{2}\right)\right] \quad (\text{A.50})$$

From $\Phi(y)$, from Equation A.42

$$\Phi'' - \lambda_3^2 \Phi = 0 \quad (\text{A.51})$$

Since we expect some symmetry about $y = \frac{h}{2}$, let

$$\tilde{y} = y - \frac{h}{2} \quad (\text{A.52})$$

Then $\tilde{\Phi}(\tilde{y}) = \Phi(y)$, and $\partial^2 \tilde{\Phi} / \partial \tilde{y}^2 = \partial^2 \Phi / \partial y^2$. Thus,

$$\tilde{\Phi}_3(\tilde{y}) = C_n \cosh(\lambda_3 \tilde{y}) + D_n \sinh(\lambda_3 \tilde{y}) \quad (\text{A.53})$$

Equivalently (since $\Psi_{3_0} = 0$, Φ_{3_0} was not sought),

$$\Phi_3(y) = C_n \cosh \left[\lambda_3 \left(y - \frac{h}{2} \right) \right] + D_n \sinh \left[\lambda_3 \left(y - \frac{h}{2} \right) \right] \quad (\text{A.54})$$

Using Equations A.50 and A.54 in A.40 yields

$$\omega_3(x, y) = \sum_{n=1}^{\infty} \left\{ b_n \cosh \left[\lambda_3 \left(y - \frac{h}{2} \right) \right] + c_n \sinh \left[\lambda_3 \left(y - \frac{h}{2} \right) \right] \right\} \psi_n^3(x) \quad (\text{A.55})$$

where

$$\psi_n^3(x) = \sin \left[n\pi \left(\frac{x}{s} + \frac{1}{2} \right) \right] \quad (\text{A.56})$$

$$b_n = A_n C_n \quad (\text{A.57})$$

$$c_n = A_n D_n \quad (\text{A.58})$$

The superscript in ψ_n^3 denotes layer 3. Finally, from Equation A.35, the potential in layer 3 is

$$\phi_3(x, y) = v_3(x) + \omega_3(x, y) \quad (\text{A.59})$$

with $v_3(x)$ and $\omega_3(x, y)$ defined in Equations A.36 and A.55, respectively.

A.3 Potentials in Layers 4 and 5

Layer 4 is located immediately above the electrodes ($h < y < l$), while layer 5 is above layer 4 ($l < y < \infty$). In each of these layers, the potential, ϕ_4 or ϕ_5 , satisfies (see Figure A.1)

$$\nabla^2 \phi_k = 0 \quad \text{for } k = 4, 5 \quad (\text{A.60})$$

$$\frac{\partial \phi_k}{\partial x} \left(\pm \frac{s+1}{2}, y \right) = 0 \quad \text{for } k = 4, 5 \quad (\text{A.61})$$

The potential also satisfies the boundary conditions developed in Chapter III. From Equations 3.57, 3.66, and 3.72

$$\lim_{y \rightarrow \infty} |\phi_5(x, y)| < \infty \quad (\text{A.62})$$

$$\phi_4(x, l) = \phi_5(x, l) \quad (\text{A.63})$$

$$\epsilon_4 \frac{\partial \phi_4}{\partial y}(x, l) = \epsilon_5 \frac{\partial \phi_5}{\partial y}(x, l) \quad (\text{A.64})$$

Potential in Layer 5. For ϕ_5 , we seek a solution of the form

$$\phi_5 = \Psi_5(x) \Phi_5(y) \quad (\text{A.65})$$

Using Equation A.65 in Equation A.60 yields

$$\Psi'' \Phi + \Psi \Phi'' = 0 \quad (\text{A.66})$$

where Ψ'' denotes $\partial^2 \Psi / \partial x^2$, and Φ'' denotes $\partial^2 \Phi / \partial y^2$. Thus,

$$\frac{\Psi''}{\Psi} = -\frac{\Phi''}{\Phi} = -\lambda^2 \quad (\text{A.67})$$

First $\Psi(x)$, from the previous equation

$$\Psi'' + \lambda_5^2 \Psi = 0 \quad (\text{A.68})$$

where λ_5 is the separation constant or eigenvalue for layer 5. Since this situation is identical to Ψ_n in layer 2, including the boundary conditions, the results of Ψ_{2n} can be used. From Equation A.16

$$\Psi_{5n}(x) = A_n \cos \left[n\pi \left(\frac{x}{s+1} + \frac{1}{2} \right) \right] \quad (\text{A.69})$$

and

$$\lambda_5 = \frac{n\pi}{s+1}, \text{ for } n = 0, 1, 2, \dots \quad (\text{A.70})$$

Now for $\Phi(y)$, from Equation A.67

$$\Phi'' - \lambda_5^2 \Phi = 0 \quad (\text{A.71})$$

or

$$\Phi_0'' = 0 \quad \text{for } n = 0 \quad (\text{A.72})$$

$$\Phi_n'' - \lambda_5^2 \Phi_n = 0 \quad \text{for } n \neq 0 \quad (\text{A.73})$$

Thus,

$$\Phi_0(y) = C_0 y + D_0 \quad (\text{A.74})$$

$$\Phi_n(y) = C_n \exp(\lambda_5 y) + D_n \exp(-\lambda_5 y) \quad (\text{A.75})$$

Enforcing Equation A.62 yields

$$\lim_{y \rightarrow \infty} |C_0 y + D_0| < \infty \quad (\text{A.76})$$

$$\lim_{y \rightarrow \infty} |C_n \exp(\lambda_5 y) + D_n \exp(-\lambda_5 y)| < \infty \quad (\text{A.77})$$

Hence $C_0 = C_n = 0$, and

$$\Phi_n(y) = \begin{cases} D_0 & \text{for } n = 0 \\ D_n \exp(-\lambda_5 y) & \text{for } n \neq 0 \end{cases} \quad (\text{A.78})$$

From Equation A.65

$$\phi_{5_n}(x, y) = \Psi_{5_n}(x)\Phi_{5_n}(y) \quad (\text{A.79})$$

or

$$\phi_5(x, y) = D_0 + \sum_{n=1}^{\infty} \Psi_n(x)D_n \exp(-\lambda_5 y) \quad (\text{A.80})$$

since $\Psi_{5_0}(x) = A_0$ and the constants were combined into D_0 .

Potential in Layer 4. For $\phi_4(x, y)$, we again seek a solution of the form

$$\phi_4 = \Psi_4(x)\Phi_4(y) \quad (\text{A.81})$$

Using Equation A.81 in Equation A.60 yields

$$\Psi''\Phi + \Psi\Phi'' = 0 \quad (\text{A.82})$$

or

$$\frac{\Psi''}{\Psi} = -\frac{\Phi''}{\Phi} = -\lambda_4^2 \quad (\text{A.83})$$

where λ_4 is the separation constant or eigenvalue for layer 4. First determine $\Psi_4(x)$, from the above equation

$$\Psi'' + \lambda_4^2 \Psi = 0 \quad (\text{A.84})$$

Since this situation is identical to $\Psi_5(x)$, including the boundary conditions, then

$$\Psi_{4_n} = \Psi_{5_n} = \Psi_n = A_n \cos \left[n\pi \left(\frac{x}{s+1} + \frac{1}{2} \right) \right] \quad (\text{A.85})$$

and

$$\lambda_4 = \lambda_5 = \frac{n\pi}{s+1}, \text{ for } n = 0, 1, 2, \dots \quad (\text{A.86})$$

Now for Φ_4 , let

$$\tilde{y} = y - l \quad (\text{A.87})$$

which leads to $\tilde{\Phi}(\tilde{y}) = \Phi(y)$, and $\partial^2 \tilde{\Phi} / \partial \tilde{y}^2 = \partial^2 \Phi / \partial y^2$. From Equation A.83

$$\tilde{\Phi}'' - \lambda^2 \tilde{\Phi} = 0 \quad (\text{A.88})$$

or

$$\tilde{\Phi}_0'' = 0 \quad \text{for } n = 0 \quad (\text{A.89})$$

$$\tilde{\Phi}_n'' - \lambda_4^2 \tilde{\Phi}_n = 0 \quad \text{for } n \neq 0 \quad (\text{A.90})$$

Hence

$$\tilde{\Phi}_n(\tilde{y}) = \begin{cases} F_0 y + E_0 & \text{for } n = 0 \\ E_n \cosh(\lambda y) + F_n \sinh(\lambda y) & \text{for } n \neq 0 \end{cases} \quad (\text{A.91})$$

and

$$\tilde{\phi}_4(x, \tilde{y}) = F_0 y + E_0 + \sum_{n=0}^{\infty} \Psi_n [E_n \cosh(\lambda \tilde{y}) + F_n \sinh(\lambda \tilde{y})] \quad (\text{A.92})$$

Applying Boundary Data. Using Equations A.92 and A.80 in A.63 yields

$$D_0 + \sum_{n=1}^{\infty} \Psi_n(x) D_n \exp(-\lambda l) = E_0 + \sum_{n=0}^{\infty} \Psi_n(x) E_n \quad (\text{A.93})$$

Thus,

$$E_0 = D_0 \quad (\text{A.94})$$

$$E_n = D_n \exp(-\lambda l) \quad (\text{A.95})$$

Using Equations A.92 and A.80 in A.64 yields

$$\epsilon_5 \sum_{n=1}^{\infty} \Psi_n(x) [-\lambda D_n] \exp(-\lambda l) = \epsilon_4 \left[F_0 + \sum_{n=0}^{\infty} \Psi_n(x) \lambda F_n \right] \quad (\text{A.96})$$

Thus,

$$F_0 = 0 \quad (\text{A.97})$$

$$F_n = -\frac{\epsilon_5}{\epsilon_4} D_n \exp(-\lambda l) \quad (\text{A.98})$$

Hence,

$$\tilde{\phi}_4(x, \tilde{y}) = D_0 + \sum_{n=1}^{\infty} \Psi_n D_n \exp(-\lambda l) \left[\cosh(\lambda \tilde{y}) - \frac{\epsilon_5}{\epsilon_4} \sinh(\lambda \tilde{y}) \right] \quad (\text{A.99})$$

or the potential in layer 4 can be expressed as

$$\phi_4(x, y) = d_0 + \sum_{n=1}^{\infty} d_n \mathcal{F}_n^4(y) \psi_n^4(x) \quad (\text{A.100})$$

where

$$\mathcal{F}_n^4(y) = \exp(-\lambda_4 l) \left\{ \cosh[\lambda_4(l-y)] + \frac{\epsilon_5}{\epsilon_4} \sinh[\lambda_4(l-y)] \right\} \quad (\text{A.101})$$

$$d_n = A_n D_n \quad (\text{A.102})$$

$$d_0 = D_0 \quad (\text{A.103})$$

$$\psi_n^4(x) = \cos \left[n\pi \left(\frac{x}{s+1} + \frac{1}{2} \right) \right] \quad (\text{A.104})$$

Finally, the potential in layer 5 is

$$\phi_5(x, y) = d_0 + \sum_{n=1}^{\infty} d_n \exp(-\lambda_5 y) \psi_n^5(x) \quad (\text{A.105})$$

where

$$\psi_n^5(x) = \cos \left[n\pi \left(\frac{x}{s+1} + \frac{1}{2} \right) \right] \quad (\text{A.106})$$

The superscripts on ψ_n^4 and ψ_n^5 denote the material layer of interest instead of the conventional power operator notation.

A.4 Boundary Between Layers 2 and 3

Summary of Potential Functions. From Equations A.27 A.36, A.55 and A.54

$$\phi_2(x, y) = a_0(y + d) + \sum_{n=1}^{\infty} a_n \sinh[\lambda_2(y + d)] \psi_n^2(x) \quad (\text{A.107})$$

$$\frac{\partial \phi_2}{\partial y}(x, y) = a_0 + \sum_{n=1}^{\infty} \lambda_2 a_n \cosh[\lambda_2(y + d)] \psi_n^2(x) \quad (\text{A.108})$$

$$\phi_3(x, y) = v_3(x) + \sum_{n=1}^{\infty} \left\{ b_n \cosh \left[\lambda_3 \left(y - \frac{h}{2} \right) \right] + c_n \sinh \left[\lambda_3 \left(y - \frac{h}{2} \right) \right] \right\} \psi_n^3(x) \quad (\text{A.109})$$

$$\frac{\partial \phi_3}{\partial y}(x, y) = \sum_{n=1}^{\infty} \lambda_3 \left\{ b_n \sinh \left[\lambda_3 \left(y - \frac{h}{2} \right) \right] + c_n \cosh \left[\lambda_3 \left(y - \frac{h}{2} \right) \right] \right\} \psi_n^3(x) \quad (\text{A.110})$$

where

$$\psi_n^2(x) = \cos \left[n\pi \left(\frac{x}{s+1} + \frac{1}{2} \right) \right] \quad (\text{A.111})$$

$$\psi_n^3(x) = \sin \left[n\pi \left(\frac{x}{s} + \frac{1}{2} \right) \right] \quad (\text{A.112})$$

$$v_3(x) = \left(\frac{V_2 - V_1}{s} \right) x + \frac{V_2 + V_1}{2} \quad (\text{A.113})$$

$$\lambda_2 = \frac{n\pi}{s+1} \quad (\text{A.114})$$

$$\lambda_3 = \frac{n\pi}{s} \quad (\text{A.115})$$

Boundary Conditions. The boundary conditions for the interfaces between layers were developed in Chapter III. From Equations 3.58, 3.60, 3.64, and 3.70

$$\phi_2(x, 0) = f(x) \quad (\text{A.116})$$

$$\epsilon_2 \frac{\partial \phi_2}{\partial y}(x, 0) = \epsilon_3 \frac{\partial \phi_3}{\partial y}(x, 0) \quad (\text{A.117})$$

where

$$f(x) = \begin{cases} V_1, & \text{for } -\frac{s+1}{2} \leq x \leq -\frac{s}{2} \\ \phi_3(x, 0), & \text{for } -\frac{s}{2} < x < \frac{s}{2} \\ V_2, & \text{for } \frac{s}{2} \leq x \leq \frac{s+1}{2} \end{cases} \quad (\text{A.118})$$

Using Equations A.107 and A.109 in A.116 gives

$$a_0 d + \sum_{n=1}^{\infty} a_n \Theta_n^c \psi_n^2 = f(x) \quad (\text{A.119})$$

where

$$\Theta_n^c = \sinh \left(\frac{n\pi d}{s+1} \right) \quad (\text{A.120})$$

To determine the a_n terms, Equation A.119 is "sifted" by multiplying each side by ψ_m^2 and integrating with respect to x over the interval $-\frac{s+1}{2} \leq x \leq \frac{s+1}{2}$. Accordingly,

$$a_0 d \langle 1, 1 \rangle = \langle f(x), 1 \rangle \quad (\text{A.121})$$

$$\sum_{n=1}^{\infty} a_n \Theta_n^c \langle \psi_n^2, \psi_m^2 \rangle = \langle f(x), \psi_m^2 \rangle \quad (\text{A.122})$$

where "1" denotes the function, ψ_0^2 , which has constant unit value over the interval and

$$\psi_0^2 = 1 \quad \text{for } m = 0 \quad (\text{A.123})$$

$$\langle g(x), h(x) \rangle = \int_{-\frac{s+1}{2}}^{\frac{s+1}{2}} g(x) \cdot h(x) dx \quad (\text{A.124})$$

ψ_n^2 are cosine eigenfunctions which are orthogonal to the constant function. Therefore, only the $m = 0$ term is used for sifting the constant term. First, evaluating $\langle 1, 1 \rangle$ yields

$$\langle 1, 1 \rangle = \int_{-\frac{s+1}{2}}^{\frac{s+1}{2}} dx = (s+1) \quad (\text{A.125})$$

Evaluating $\langle f(x), 1 \rangle$ yields

$$\langle f(x), 1 \rangle = \langle V_1, 1 \rangle_- + \langle \phi_3(x, 0), 1 \rangle_0 + \langle V_2, 1 \rangle_+ \quad (\text{A.126})$$

where

$$\langle V_1, 1 \rangle_- = V_1 \int_{-\frac{s+1}{2}}^{-\frac{s}{2}} dx = \frac{V_1}{2} \quad (\text{A.127})$$

and

$$\langle V_2, 1 \rangle_+ = V_2 \int_{\frac{s}{2}}^{\frac{s+1}{2}} dx = \frac{V_2}{2} \quad (\text{A.128})$$

Next,

$$\langle \phi_3(x, 0), 1 \rangle_0 = \langle v_3(x), 1 \rangle_0 + \sum_{n=1}^{\infty} [b_n \Phi_n^c - c_n \Psi_n^c] \langle \psi_n^3, 1 \rangle_0 \quad (\text{A.129})$$

where

$$\Phi_n^c = \cosh \left(\frac{n\pi h}{2s} \right) \quad (\text{A.130})$$

$$\Psi_n^c = \sinh \left(\frac{n\pi h}{2s} \right) \quad (\text{A.131})$$

$$\begin{aligned} \langle v_3(x), 1 \rangle_0 &= \int_{-\frac{s}{2}}^{\frac{s}{2}} \left(\frac{V_2 - V_1}{s} \right) x dx + \int_{-\frac{s}{2}}^{\frac{s}{2}} \left(\frac{V_1 + V_2}{2} \right) dx \\ &= \frac{s}{2} (V_1 + V_2) \end{aligned} \quad (\text{A.132})$$

$$\langle \psi_n^3, 1 \rangle_0 = \int_{-\frac{s}{2}}^{\frac{s}{2}} \sin \left[n\pi \left(\frac{x}{s} + \frac{1}{2} \right) \right] dx \quad (\text{A.133})$$

Using $\tau = \frac{x}{s} + \frac{1}{2}$ yields

$$\begin{aligned} \langle \psi_n^3, 1 \rangle_0 &= \int_0^1 \sin(n\pi\tau) s d\tau \\ &= -\frac{s}{n\pi} [\cos(n\pi\tau)]_0^1 \\ &= -\frac{s}{n\pi} [\cos(n\pi) - 1] \\ \langle \psi_n^3, 1 \rangle_0 &= \frac{s}{n\pi} [1 - (-1)^n] \end{aligned} \quad (\text{A.134})$$

Using Equations A.125, A.126, A.127, A.128, A.129, A.132, A.134 in Equation A.121 yields

$$a_0 d(s+1) = \frac{V_1}{2} + \frac{V_2}{2} + \frac{s}{2} (V_1 + V_2) + \sum_{n=1}^{\infty} [b_n \Phi_n^c - c_n \Psi_n^c] \frac{s}{n\pi} [1 - (-1)^n] \quad (\text{A.135})$$

or

$$a_0 d(s+1) - \sum_{n=1}^{\infty} [b_n \Phi_n^c - c_n \Psi_n^c] \frac{s}{n\pi} [1 - (-1)^n] = \frac{s+1}{2} (V_1 + V_2) \quad (\text{A.136})$$

Next, evaluating $\langle \psi_n^2, \psi_m^2 \rangle$ yields

$$\langle \psi_n^2, \psi_m^2 \rangle = \int_{-\frac{s+1}{2}}^{\frac{s+1}{2}} \cos \left[n\pi \left(\frac{x}{s+1} + \frac{1}{2} \right) \right] \cdot \cos \left[m\pi \left(\frac{x}{s+1} + \frac{1}{2} \right) \right] dx \quad (\text{A.137})$$

To simplify the algebra, let

$$\tau = \frac{x}{s+1} + \frac{1}{2} \quad (\text{A.138})$$

then

$$x = (s+1)\tau - t \quad (\text{A.139})$$

$$dx = (s+1) d\tau \quad (\text{A.140})$$

Using Equations A.138 and A.140 in A.137 yields

$$\langle \psi_n^2, \psi_m^2 \rangle = (s+1) \int_0^1 \cos(n\pi\tau) \cos(m\pi\tau) d\tau \quad (\text{A.141})$$

$$\langle \psi_n^2, \psi_m^2 \rangle = \frac{s+1}{\pi} \int_0^\pi \cos(n\alpha) \cos(m\alpha) d\alpha \quad (\text{A.142})$$

where $\alpha = \pi\tau$ and $d\alpha = \pi d\tau$. For integers m and n

$$\int_0^\pi \cos(n\alpha) \cdot \cos(m\alpha) d\alpha = \begin{cases} 0, & \text{for } n \neq m \\ \frac{\pi}{2}, & \text{for } n = m \end{cases} \quad (\text{A.143})$$

Thus,

$$\langle \psi_n^2, \psi_m^2 \rangle = \begin{cases} 0, & \text{for } n \neq m \\ \frac{s+1}{2}, & \text{for } n = m \end{cases} \quad (\text{A.144})$$

Evaluating $\langle f(x), \psi_m^2 \rangle$ yields

$$\langle f(x), \psi_m^2 \rangle = \langle V_1, \psi_m^2 \rangle_- + \langle \phi_3, \psi_m^2 \rangle_0 + \langle V_2, \psi_m^2 \rangle_+ \quad (\text{A.145})$$

where

$$\langle V_1, \psi_m^2 \rangle_- = V_1 \int_{-\frac{s+1}{2}}^{-\frac{1}{2}} \psi_m^2 dx \quad (\text{A.146})$$

$$\langle \phi_3, \psi_m^2 \rangle_0 = \int_{-\frac{1}{2}}^{\frac{1}{2}} \phi_3(x, 0) \psi_m^2 dx \quad (\text{A.147})$$

$$\langle V_2, \psi_m^2 \rangle_+ = V_2 \int_{\frac{1}{2}}^{\frac{s+1}{2}} \psi_m^2 dx \quad (\text{A.148})$$

For $\langle V_1, \psi_m^2 \rangle_-$, using Equations A.111, A.138 and A.140 in A.146 yields

$$\langle V_1, \psi_m^2 \rangle_- = (s+1)V_1 \int_{\tau_i^-}^{\tau_f^-} \cos(m\pi\tau) d\tau \quad (\text{A.149})$$

where $\tau_i^- = -\frac{s+1}{2} \frac{1}{s+1} + \frac{1}{2} = 0$ and $\tau_f^- = -\frac{s}{2} \frac{1}{s+1} + \frac{1}{2} = \frac{1}{2s+2}$. Integration yields

$$\langle V_1, \psi_m^2 \rangle_- = V_1(s+1) \left[\frac{1}{m\pi} \sin(m\pi\tau) \right]_0^{\tau_f^-} \quad (\text{A.150})$$

or

$$\langle V_1, \psi_m^2 \rangle_- = \frac{V_1(s+1)}{m\pi} \sin\left(\frac{m\pi}{2s+2}\right) \quad (\text{A.151})$$

For $\langle V_2, \psi_m^2 \rangle_+$, using Equations A.111, A.138 and A.140 in A.148 yields

$$\langle V_2, \psi_m^2 \rangle_+ = (s+1)V_2 \int_{\tau_i^+}^{\tau_f^+} \cos(m\pi\tau) d\tau \quad (\text{A.152})$$

where $\tau_i^+ = \frac{s}{2} \frac{1}{s+1} + \frac{1}{2} = \frac{2s+1}{2s+2}$ and $\tau_f^+ = \frac{s+1}{2} \frac{1}{s+1} + \frac{1}{2} = 1$. Integration yields

$$\langle V_2, \psi_m^2 \rangle_+ = V_2(s+1) \left[\frac{1}{m\pi} \sin(m\pi\tau) \right]_{\tau_i^+}^1 \quad (\text{A.153})$$

or

$$\langle V_2, \psi_m^2 \rangle_+ = -\frac{V_2(s+1)}{m\pi} \sin\left[m\pi\left(\frac{2s+1}{2s+2}\right)\right] \quad (\text{A.154})$$

Since

$$\sin x = -\sin(x - \pi) = \sin(x - 2\pi) = -\sin(x - 3\pi) \quad (\text{A.155})$$

then

$$\sin x = (-1)^m \sin(x - m\pi) = -(-1)^m \sin(m\pi - x) \quad (\text{A.156})$$

Using $x = m\pi \frac{2s+1}{2s+2}$ yields

$$\sin \left(m\pi \frac{2s+1}{2s+2} \right) = -(-1)^m \sin \left(\frac{m\pi}{2s+2} \right) \quad (\text{A.157})$$

and hence,

$$\langle V_2, \psi_m^2 \rangle^+ = (-1)^m \frac{V_2(s+1)}{m\pi} \sin \left(\frac{m\pi}{2s+2} \right) \quad (\text{A.158})$$

For $\langle \phi_3, \psi_m^2 \rangle_0$, using Equation A.109 in A.147 yields

$$\langle \phi_3, \psi_m^2 \rangle_0 = \langle v_3, \psi_m^2 \rangle_0 + \sum_{n=1}^{\infty} (b_n \Phi_n^c - c_n \Psi_n^c) \langle \psi_n^3, \psi_m^2 \rangle_0 \quad (\text{A.159})$$

where

$$\langle v_3, \psi_m^2 \rangle_0 = \int_{-\frac{1}{2}}^{\frac{1}{2}} v_3(x) \cdot \psi_m^2 dx \quad (\text{A.160})$$

$$\langle \psi_n^3, \psi_m^2 \rangle_0 = \int_{-\frac{1}{2}}^{\frac{1}{2}} \psi_n^3 \cdot \psi_m^2 dx \quad (\text{A.161})$$

For simplification, let

$$\langle v_3, \psi_m^2 \rangle_0 = I_m^1 + I_m^2 \quad (\text{A.162})$$

$$\langle \psi_n^3, \psi_m^2 \rangle_0 = I_{mn}^3 \quad (\text{A.163})$$

where

$$I_m^1 = \int_{-\frac{1}{2}}^{\frac{1}{2}} \left(\frac{V_2 - V_1}{s} \right) x \psi_m^2 dx \quad (\text{A.164})$$

$$I_m^2 = \int_{-\frac{1}{2}}^{\frac{1}{2}} \left(\frac{V_2 + V_1}{2} \right) \psi_m^2 dx \quad (\text{A.165})$$

Using Equations A.144, A.145, A.151, A.158, A.159, A.163 in A.122 yields

$$a_m \Theta_m^c \frac{s+1}{2} = \mathcal{I}_m + \sum_{n=1}^{\infty} [b_n \Phi_n^c - c_n \Psi_n^c] I_{mn}^3 \quad (\text{A.166})$$

where

$$\mathcal{I}_m = \langle V_1, \psi_m^2 \rangle_- + \langle V_2, \psi_m^2 \rangle^+ + I_m^1 + I_m^2 \quad (\text{A.167})$$

or

$$a_m \Theta_m^c \frac{s+1}{2} - \sum_{n=1}^{\infty} [b_n \Phi_n^c - c_n \Psi_n^c] I_{mn}^3 = \mathcal{I}_m \quad (\text{A.168})$$

For the jump condition, using Equation A.108, A.110, A.114, and A.115 in A.117 yields

$$\epsilon_2 \left[a_0 + \sum_{n=1}^{\infty} \frac{n\pi}{s+1} a_n \Gamma_n^c \psi_n^2 \right] = \epsilon_3 \sum_{n=1}^{\infty} \frac{n\pi}{s} (-b_n \Psi_n^c + c_n \Phi_n^c) \psi_n^3 \quad (\text{A.169})$$

where

$$\Gamma_n^c = \cosh \left(\frac{n\pi d}{s+1} \right) \quad (\text{A.170})$$

Here, sifting occurs with ψ_m^3 , because the interval over which the jump condition applies is $-s/2 < x < s/2$. Thus,

$$\epsilon_2 a_0 \langle 1, \psi_m^3 \rangle + \sum_{n=1}^{\infty} \frac{\epsilon_2 n\pi}{s+1} a_n \Gamma_n^c \langle \psi_n^2, \psi_m^3 \rangle = \epsilon_3 \sum_{n=1}^{\infty} \frac{n\pi}{s} (-b_n \Phi_n^c + c_n \Psi_n^c) \langle \psi_n^3, \psi_m^3 \rangle \quad (\text{A.171})$$

which leaves $\langle 1, \psi_m^3 \rangle$, $\langle \psi_n^2, \psi_m^3 \rangle$ and $\langle \psi_n^3, \psi_m^3 \rangle$ to be solved. First, $\langle 1, \psi_m^3 \rangle$ can be written as

$$\langle 1, \psi_m^3 \rangle = \int_{-s/2}^{s/2} \sin \left[m\pi \left(\frac{x}{s} + \frac{1}{2} \right) \right] dx \quad (\text{A.172})$$

Using $\tau = \frac{x}{s} + \frac{1}{2}$ and $s d\tau = dx$ yields

$$\begin{aligned} \langle 1, \psi_m^3 \rangle &= s \int_0^1 \sin(m\pi\tau) d\tau = s \left[-\frac{\cos(m\pi\tau)}{m\pi} \right]_0^1 \\ &= \frac{s}{m\pi} [-\cos(m\pi) + 1] = \frac{s}{m\pi} [1 - (-1)^m] \end{aligned} \quad (\text{A.173})$$

Evaluating $\langle \psi_n^2, \psi_m^3 \rangle$ yields (see Equation A.163)

$$\langle \psi_n^2, \psi_m^3 \rangle = \int_{-s/2}^{s/2} \cos \left[n\pi \left(\frac{x}{s+1} + \frac{1}{2} \right) \right] \cdot \sin \left[m\pi \left(\frac{x}{s} + \frac{1}{2} \right) \right] dx \quad (\text{A.174})$$

$$= I_{nm}^3 \quad (\text{A.175})$$

Next $\langle \psi_n^3, \psi_m^3 \rangle$

$$\langle \psi_n^3, \psi_m^3 \rangle = \int_{-s/2}^{s/2} \sin \left[n\pi \left(\frac{x}{s} + \frac{1}{2} \right) \right] \cdot \sin \left[m\pi \left(\frac{x}{s} + \frac{1}{2} \right) \right] dx \quad (\text{A.176})$$

Using $\tau = \frac{x}{s} + \frac{1}{2}$ and $s d\tau = dx$ yields

$$\begin{aligned} \langle \psi_n^3, \psi_m^3 \rangle &= s \int_0^1 \sin(n\pi\tau) \cdot \sin(m\pi\tau) d\tau \\ &= \frac{s}{\pi} \int_0^\pi \sin(n\alpha) \cdot \sin(m\alpha) d\alpha \end{aligned} \quad (\text{A.177})$$

where $\alpha = \pi\tau$. For integers m and n

$$\int_0^\pi \sin(nx) \cdot \sin(mx) dx = \begin{cases} 0, & \text{for } n \neq m \\ \frac{\pi}{2}, & \text{for } n = m \end{cases} \quad (\text{A.178})$$

Thus,

$$\langle \psi_n^3, \psi_m^3 \rangle = \begin{cases} 0, & \text{for } n \neq m \\ \frac{s}{2}, & \text{for } n = m \end{cases} \quad (\text{A.179})$$

Using Equations A.173, A.175, and A.179 in A.169 yields

$$\frac{\epsilon_2 s}{m\pi} [1 - (-1)^m] a_0 + \epsilon_2 \sum_{n=1}^{\infty} \frac{n\pi}{s+1} a_n \Gamma_n^c I_{nm}^3 = \frac{\epsilon_3 m\pi}{s} \frac{s}{2} (-b_m \Psi_m^c + c_m \Phi_m^c) \quad (\text{A.180})$$

Summary of Equations for Layer 2-3 Interface. The results of matching the boundary conditions along the interface between layers 2 and 3 provided the following equations that must be solved to determine the potential coefficients

$$\frac{s+1}{2} (V_1 + V_2) = a_0 d(s+1) - \sum_{n=1}^{\infty} \frac{s}{n\pi} (b_n \Phi_n^c - c_n \Psi_n^c) [1 - (-1)^n] \quad (\text{A.181})$$

$$\mathcal{I}_m = a_m \Theta_m^c \frac{s+1}{2} - \sum_{n=1}^{\infty} (b_n \Phi_n^c - c_n \Psi_n^c) I_{mn}^3 \quad (\text{A.182})$$

$$0 = \frac{\epsilon_2 s}{m\pi} [1 - (-1)^m] a_0 + \sum_{n=1}^{\infty} \frac{\epsilon_2 n\pi}{s+1} a_n \Gamma_n^c I_{nm}^3 + \frac{\epsilon_3 m\pi}{2} (b_m \Psi_m^c - c_m \Phi_m^c) \quad (\text{A.183})$$

A.5 Boundary Between Layers 3 and 4

Summary of Potential Functions. From Equations A.100 and A.109

$$\phi_4(x, y) = d_0 + \sum_{n=1}^{\infty} d_n \mathcal{F}_n^4(y) \psi_n^4(x) \quad (\text{A.184})$$

$$\frac{\partial \phi_4}{\partial y}(x, y) = - \sum_{n=1}^{\infty} \lambda_4 d_n \mathcal{H}_n^4(y) \psi_n^4(x) \quad (\text{A.185})$$

$$\phi_3(x, y) = v_3(x) + \sum_{n=1}^{\infty} \left\{ b_n \cosh \left[\lambda_3 \left(y - \frac{h}{2} \right) \right] + c_n \sinh \left[\lambda_3 \left(y - \frac{h}{2} \right) \right] \right\} \psi_n^3(x) \quad (\text{A.186})$$

$$\frac{\partial \phi_3}{\partial y}(x, y) = \sum_{n=1}^{\infty} \lambda_3 \left\{ b_n \sinh \left[\lambda_3 \left(y - \frac{h}{2} \right) \right] + c_n \cosh \left[\lambda_3 \left(y - \frac{h}{2} \right) \right] \right\} \psi_n^3(x) \quad (\text{A.187})$$

where

$$\mathcal{F}_n^4(y) = \exp(-\lambda_4 l) \left\{ \cosh[\lambda_4(l-y)] + \frac{\epsilon_5}{\epsilon_4} \sinh[\lambda_4(l-y)] \right\} \quad (\text{A.188})$$

$$\mathcal{H}_n^4(y) = \exp(-\lambda_4 l) \left\{ \sinh[\lambda_4(l-y)] + \frac{\epsilon_5}{\epsilon_4} \cosh[\lambda_4(l-y)] \right\} \quad (\text{A.189})$$

$$\psi_n^4(x) = \cos \left[n\pi \left(\frac{x}{s+1} + \frac{1}{2} \right) \right] \quad (\text{A.190})$$

$$\psi_n^3(x) = \sin \left[n\pi \left(\frac{x}{s} + \frac{1}{2} \right) \right] \quad (\text{A.191})$$

$$v_3(x) = \left(\frac{V_2 - V_1}{s} \right) x + \frac{V_2 + V_1}{2} \quad (\text{A.192})$$

$$\lambda_4 = \frac{n\pi}{s+1} \quad (\text{A.193})$$

$$\lambda_3 = \frac{n\pi}{s} \quad (\text{A.194})$$

Boundary Conditions. The boundary conditions for the interfaces between the layers were developed in Chapter III. From Equations 3.59, 3.61, 3.65, and 3.71

$$\phi_4(x, h) = g(x) \quad (\text{A.195})$$

$$\epsilon_4 \frac{\partial \phi_4}{\partial y}(x, h) = \epsilon_3 \frac{\partial \phi_3}{\partial y}(x, h) \quad (\text{A.196})$$

where

$$g(x) = \begin{cases} V_1, & \text{for } -\frac{s+1}{2} \leq x \leq -\frac{s}{2} \\ \phi_3(x, h), & \text{for } -\frac{s}{2} < x < \frac{s}{2} \\ V_2, & \text{for } \frac{s}{2} \leq x \leq \frac{s+1}{2} \end{cases} \quad (\text{A.197})$$

Using Equations A.184 and A.186 in A.195 gives

$$d_0 + \sum_{n=1}^{\infty} d_n \mathcal{F}_n^4(h) \psi_n^4(x) = g(x) \quad (\text{A.198})$$

As at the boundary between layers 2 and 3, the d_n terms are determined by "sifting" Equation A.198. Each side of the equation is multiplied by ψ_m^4 and then integrated with respect to x over the interval $-\frac{s+1}{2} \leq x \leq \frac{s+1}{2}$. Since $\psi_n^4 = \psi_n^2$, the results of Equations A.125, A.126, A.127, A.128, A.129, A.132, and A.134 can be used in Equation A.198 to obtain

$$d_0(s+1) = \frac{s+1}{2} (V_1 + V_2) + \sum_{n=1}^{\infty} [b_n \Phi_n^c + c_n \Psi_n^c] \frac{s}{n\pi} [1 - (-1)^n] \quad (\text{A.199})$$

$$d_m \mathcal{F}_m^4(h) \frac{s+1}{2} = \mathcal{I}_m + \sum_{n=1}^{\infty} [b_n \Phi_n^c + c_n \Psi_n^c] I_{mn}^3 \quad (\text{A.200})$$

For the jump condition, Equations A.185 and A.187 can be substituted into Equation A.196 to obtain

$$-\epsilon_4 \sum_{n=1}^{\infty} \frac{n\pi}{s+1} d_n \mathcal{H}_n^4(h) \psi_n^4 = \epsilon_3 \sum_{n=1}^{\infty} \frac{n\pi}{s} (b_n \Psi_n^c + c_n \Phi_n^c) \psi_n^3 \quad (\text{A.201})$$

Here, as in the lower boundary between layers 2 and 3, sifting is accomplished using the inner eigenfunction ψ_m^3 over the interval $-s/2 < x < s/2$. Since $\psi_n^4 = \psi_n^2$, The results of Equations A.175 and A.179 can be used to obtain

$$-\epsilon_4 \sum_{n=1}^{\infty} \frac{n\pi}{s+1} d_n \mathcal{H}_n^4(h) I_{nm}^3 = \epsilon_3 \frac{m\pi}{s} \frac{s}{2} (b_m \Psi_m^c + c_m \Phi_m^c) \quad (\text{A.202})$$

Summary of Equations for Layer 3-4 Interface. The results of matching boundary conditions at the interface between layers 3 and 4 provides the following equations, which the potential coefficients must satisfy:

$$\frac{s+1}{2} (V_1 + V_2) = d_0(s+1) - \sum_{n=1}^{\infty} \frac{s}{n\pi} (b_n \Phi_n^c + c_n \Psi_n^c) [1 - (-1)^n] \quad (\text{A.203})$$

$$\mathcal{I}_m = d_m \mathcal{F}_m^4(h) \frac{s+1}{2} - \sum_{n=1}^{\infty} (b_n \Phi_n^c + c_n \Psi_n^c) I_{mn}^3 \quad (\text{A.204})$$

$$0 = \sum_{n=1}^{\infty} \frac{\epsilon_4 n\pi}{s+1} d_n \mathcal{H}_n^4(h) I_{nm}^3 + \frac{\epsilon_3 m\pi}{2} (b_m \Psi_m^c + c_m \Phi_m^c) \quad (\text{A.205})$$

A.6 Evaluation of I_m^1

From Equation A.164

$$I_m^1 = \int_{-\frac{s}{2}}^{\frac{s}{2}} \left(\frac{V_2 - V_1}{s} \right) x \cos \left[m\pi \left(\frac{x}{s+1} + \frac{1}{2} \right) \right] dx \quad (\text{A.206})$$

Using $\tau = \frac{x}{s+1} + \frac{1}{2}$, and $dx = (s+1)d\tau$ yields

$$\begin{aligned} I_m^1 &= \frac{V_2 - V_1}{s} \int_{\tau_i}^{\tau_f} (s+1)^2 \left(\tau - \frac{1}{2} \right) \cos(m\pi\tau) d\tau \\ &= \frac{(V_2 - V_1)(s+1)^2}{s} \left[\int_{\tau_i}^{\tau_f} \tau \cos(m\pi\tau) d\tau - \frac{1}{2} \int_{\tau_i}^{\tau_f} \cos(m\pi\tau) d\tau \right] \end{aligned} \quad (\text{A.207})$$

Since

$$\int x(\cos ax) dx = \frac{1}{a^2} \cos ax + \frac{x}{a} \sin ax \quad (\text{A.208})$$

then

$$\begin{aligned}
\frac{I_m^1 s}{(V_2 - V_1)(s+1)^2} &= \left[\frac{\cos(m\pi\tau)}{m^2\pi^2} + \frac{\tau \sin(m\pi\tau)}{m\pi} - \frac{\sin(m\pi\tau)}{2m\pi} \right]_{\tau_1}^{\tau_2} \\
&= \frac{1}{m^2\pi^2} \left[\cos\left(m\pi \frac{2s+1}{2s+2}\right) - \cos\left(\frac{m\pi}{2s+2}\right) \right] \\
&\quad + \frac{1}{m\pi} \frac{2s+1}{2s+2} \sin\left(m\pi \frac{2s+1}{2s+2}\right) - \frac{1}{m\pi(2s+2)} \sin\left(\frac{m\pi}{2s+2}\right) \\
&\quad - \frac{1}{2m\pi} \sin\left(m\pi \frac{2s+1}{2s+2}\right) + \frac{1}{2m\pi} \sin\left(\frac{m\pi}{2s+2}\right)
\end{aligned} \tag{A.209}$$

Since $\cos(x) = (-1)^m \cos(m\pi - x)$, and $\sin(x) = (-1)^m \sin(x - m\pi)$, then

$$\cos\left(m\pi \frac{2s+1}{2s+2}\right) = (-1)^m \cos\left(\frac{m\pi}{2s+2}\right) \tag{A.210}$$

$$\sin\left(m\pi \frac{2s+1}{2s+2}\right) = -(-1)^m \sin\left(\frac{m\pi}{2s+2}\right) \tag{A.211}$$

and

$$\begin{aligned}
\frac{I_m^1 s m \pi}{(V_2 - V_1)(s+1)^2} &= \frac{1}{m\pi} \cos\left(\frac{m\pi}{2s+2}\right) [(-1)^m - 1] \\
&\quad + \sin\left(\frac{m\pi}{2s+2}\right) \left[-(-1)^m \frac{2s+1-(s+1)}{2s+2} + \frac{s+1-1}{2s+2} \right] \\
&= \frac{1}{m\pi} \cos\left(\frac{m\pi}{2s+2}\right) [(-1)^m - 1] \\
&\quad + \frac{s}{2s+2} \sin\left(\frac{m\pi}{2s+2}\right) [1 - (-1)^m]
\end{aligned} \tag{A.212}$$

Finally,

$$\begin{aligned}
I_m^1 &= \frac{(V_2 - V_1)(s+1)^2}{s m^2 \pi^2} \cos\left(\frac{m\pi}{2s+2}\right) [(-1)^m - 1] \\
&\quad + \frac{(V_2 - V_1)(s+1)}{2m\pi} \sin\left(\frac{m\pi}{2s+2}\right) [1 - (-1)^m]
\end{aligned} \tag{A.213}$$

A.7 Evaluation of I_m^2

From Equation A.165

$$I_m^2 = \frac{V_2 + V_1}{2} \int_{-\frac{1}{2}}^{\frac{1}{2}} \cos \left[m\pi \left(\frac{x}{s+1} + \frac{1}{2} \right) \right] dx \quad (\text{A.214})$$

To simplify the algebra, let $\tau = \frac{x}{s+1} + \frac{1}{2}$. Then $(s+1)d\tau = dx$ and

$$I_m^2 = \frac{V_2 + V_1}{2} \int_{\tau_i}^{\tau_f} \cos(m\pi\tau)(s+1)d\tau \quad (\text{A.215})$$

where $\tau_i = \frac{1}{2s+2}$, and $\tau_f = \frac{2s+1}{2s+2}$. Integration yields

$$\begin{aligned} I_m^2 &= \frac{1}{2}(V_2 + V_1)(s+1) \left[\frac{1}{m\pi} \sin(m\pi\tau) \right]_{\tau_i}^{\tau_f} \\ &= \frac{(V_2 + V_1)(s+1)}{2m\pi} \left[\sin \left(m\pi \frac{2s+1}{2s+2} \right) - \sin \left(\frac{m\pi}{2s+2} \right) \right] \end{aligned} \quad (\text{A.216})$$

Since

$$\sin \left(m\pi \frac{2s+1}{2s+2} \right) = -(-1)^m \sin \left(\frac{m\pi}{2s+2} \right) \quad (\text{A.217})$$

then

$$I_m^2 = -[1 + (-1)^m] \frac{(V_2 + V_1)(s+1)}{2m\pi} \sin \left(\frac{m\pi}{2s+2} \right) \quad (\text{A.218})$$

A.8 Evaluation of I_{mn}^3

From Equation A.163

$$I_{mn}^3 = \int_{-\frac{1}{2}}^{\frac{1}{2}} \sin \left[n\pi \left(\frac{x}{s} + \frac{1}{2} \right) \right] \cos \left[m\pi \left(\frac{x}{s+1} + \frac{1}{2} \right) \right] dx \quad (\text{A.219})$$

To simplify the algebra, let

$$\tau = \frac{x}{s} + \frac{1}{2} \quad (\text{A.220})$$

then $x = s\tau - \frac{s}{2}$, and $dx = s d\tau$. Hence,

$$\begin{aligned} I_{mn}^3 &= \int_0^1 \sin(n\pi\tau) \cos \left[m\pi \left(\frac{s\tau}{s+1} - \frac{s}{2s+2} + \frac{1}{2} \right) \right] s d\tau \\ &= s \int_0^1 \sin(n\pi\tau) \cos \left[m\pi \left(\frac{2s\tau+1}{2s+2} \right) \right] d\tau \end{aligned} \quad (\text{A.221})$$

Since $\cos(\alpha + \beta) = \cos \alpha \cos \beta - \sin \alpha \sin \beta$, then

$$\begin{aligned} I_{mn}^3 &= s \int_0^1 \left[\cos \left(\frac{m\pi 2s\tau}{2s+2} \right) \cos \left(\frac{n\pi}{2s+2} \right) - \sin \left(\frac{m\pi 2s\tau}{2s+2} \right) \sin \left(\frac{n\pi}{2s+2} \right) \right] \sin(n\pi\tau) d\tau \\ &= s \cos \left(\frac{m\pi}{2s+2} \right) I_{mn}^{3a} - s \sin \left(\frac{m\pi}{2s+2} \right) I_{mn}^{3b} \end{aligned} \quad (\text{A.222})$$

where

$$I_{mn}^{3a} = \int_0^1 \cos \left(\frac{m\pi s\tau}{s+1} \right) \sin(n\pi\tau) d\tau \quad (\text{A.223})$$

$$I_{mn}^{3b} = \int_0^1 \sin \left(\frac{m\pi s\tau}{s+1} \right) \sin(n\pi\tau) d\tau \quad (\text{A.224})$$

To evaluate I_{mn}^{3a} , let $\alpha = \pi\tau$. Then $d\tau = \frac{d\alpha}{\pi}$, and

$$I_{mn}^{3a} = \int_0^\pi \cos \left(\frac{ms\alpha}{s+1} \right) \sin(n\alpha) \frac{d\alpha}{\pi} \quad (\text{A.225})$$

To further simplify the formulation, let $\tilde{m} = \frac{ms}{s+1}$. If $n = \tilde{m}$, then

$$I_{mn}^{3a} = \frac{1}{\pi} \int_0^\pi \cos(n\alpha) \sin(n\alpha) d\alpha \quad (\text{A.226})$$

Since

$$\int_0^\pi \cos ax \cdot \sin ax dx = 0 \quad (\text{A.227})$$

then

$$I_{mn}^{3a} = 0, \text{ for } n = \frac{ms}{s+1} \quad (\text{A.228})$$

For $n \neq \tilde{m}$

$$\int (\cos \alpha x) (\sin \beta x) dx = -\frac{\cos(\beta - \alpha)x}{2(\beta - \alpha)} - \frac{\cos(\beta + \alpha)x}{2(\beta + \alpha)} \quad (\text{A.229})$$

then

$$I_{mn}^{3a} = \frac{1}{\pi} \int_0^\pi \cos(\tilde{m}\alpha) \sin(n\alpha) d\alpha$$

$$\begin{aligned}
&= \frac{1}{\pi} \left[-\frac{\cos(n-\tilde{m})\alpha}{2(n-\tilde{m})} - \frac{\cos(n+\tilde{m})\alpha}{2(n+\tilde{m})} \right]_0^\pi \\
&= \frac{1}{\pi} \left\{ -\frac{\cos[(n-\tilde{m})\pi]}{2(n-\tilde{m})} - \frac{\cos[(n+\tilde{m})\pi]}{2(n+\tilde{m})} + \frac{1}{2(n-\tilde{m})} + \frac{1}{2(n+\tilde{m})} \right\} \quad (\text{A.230})
\end{aligned}$$

Since $\cos(\alpha + \beta) = \cos \alpha \cos \beta - \sin \alpha \sin \beta$, then

$$\begin{aligned}
\pi I_{mn}^{3a} &= \frac{n + \tilde{m} + n - \tilde{m}}{2(n^2 - \tilde{m}^2)} - \frac{1}{2(n - \tilde{m})} [\cos(n\pi) \cos(\tilde{m}\pi) + \sin(n\pi) \sin(\tilde{m}\pi)] \\
&\quad - \frac{1}{2(n + \tilde{m})} [\cos(n\pi) \cos(\tilde{m}\pi) + \sin(n\pi) \sin(\tilde{m}\pi)] \quad (\text{A.231})
\end{aligned}$$

Using $\sin(n\pi) = 0$ and $\cos(n\pi) = (-1)^n$ yields

$$I_{mn}^{3a} = \frac{1}{\pi} \left[\frac{n}{n^2 - \tilde{m}^2} - (-1)^n \cos(\tilde{m}\pi) \left(\frac{n}{n^2 - \tilde{m}^2} \right) \right] \quad (\text{A.232})$$

or

$$I_{mn}^{3a} = \frac{n}{\pi \left[n^2 - \left(\frac{ms}{s+1} \right)^2 \right]} \left[1 - (-1)^n \cos \left(\frac{ms\pi}{s+1} \right) \right], \text{ for } n \neq \frac{ms}{s+1} \quad (\text{A.233})$$

For I_{mn}^{3b} , from Equation A.224

$$I_{mn}^{3b} = \int_0^1 \sin \left(\frac{m\pi s\tau}{s+1} \right) \sin(n\pi\tau) d\tau \quad (\text{A.234})$$

Again, for simplification, let $\alpha = \pi\tau$. Then $d\tau = \frac{d\alpha}{\pi}$, and

$$I_{mn}^{3b} = \frac{1}{\pi} \int_0^\pi \sin \left(\frac{ms\alpha}{s+1} \right) \sin(n\alpha) d\alpha \quad (\text{A.235})$$

Using $\tilde{m} = \frac{ms}{s+1}$ yields

$$I_{mn}^{3b} = \frac{1}{\pi} \int_0^\pi \sin(\tilde{m}\alpha) \sin(n\alpha) d\alpha \quad (\text{A.236})$$

If $n = \tilde{m}$, then

$$\begin{aligned}
I_{mn}^{3b} &= \frac{1}{\pi} \int_0^\pi \sin^2(n\alpha) d\alpha = \frac{1}{2\pi} \int_0^\pi [1 - \cos(2n\alpha)] d\alpha \\
&= \frac{1}{2\pi} \left[\alpha - \frac{1}{2n} \sin(2n\alpha) \right]_0^\pi = \frac{1}{2\pi} (\pi - 0 - 0 + 0) \quad (\text{A.237})
\end{aligned}$$

Thus,

$$I_{mn}^{3b} = \frac{1}{2}, \text{ for } n = \frac{ms}{s+1} \quad (\text{A.238})$$

For $n \neq \tilde{m}$

$$\int (\sin \alpha x) (\sin \beta x) dx = \frac{\sin(\alpha - \beta)x}{2(\alpha - \beta)} - \frac{\sin(\alpha + \beta)x}{2(\alpha + \beta)} \quad (\text{A.239})$$

Hence,

$$\begin{aligned} I_{mn}^{3b} &= \frac{1}{\pi} \int_0^\pi \sin(n\alpha) \sin(\tilde{m}\alpha) d\alpha \\ &= \frac{1}{\pi} \left[\frac{\sin(n - \tilde{m})\alpha}{2(n - \tilde{m})} - \frac{\sin(n + \tilde{m})\alpha}{2(n + \tilde{m})} \right]_0^\pi \\ &= \frac{1}{\pi} \left\{ \frac{\sin[(n - \tilde{m})\pi]}{2(n - \tilde{m})} - \frac{\sin[(n + \tilde{m})\pi]}{2(n + \tilde{m})} \right\} \end{aligned} \quad (\text{A.240})$$

Since $\sin(\alpha + \beta) = \sin \alpha \cos \beta + \cos \alpha \sin \beta$, then

$$\pi I_{mn}^{3b} = \frac{\sin(n\pi) \cos(\tilde{m}\pi) - \cos(n\pi) \sin(\tilde{m}\pi)}{2(n - \tilde{m})} - \frac{\sin(n\pi) \cos(\tilde{m}\pi) + \cos(n\pi) \sin(\tilde{m}\pi)}{2(n + \tilde{m})} \quad (\text{A.241})$$

Using $\sin(n\pi) = 0$, and $\cos(n\pi) = (-1)^n$, yields

$$I_{mn}^{3b} = -\frac{1}{2\pi} \left[(-1)^n \sin(\tilde{m}\pi) \left(\frac{1}{n - \tilde{m}} + \frac{1}{n + \tilde{m}} \right) \right] \quad (\text{A.242})$$

or

$$I_{mn}^{3b} = -\frac{(-1)^n n}{\pi \left[n^2 - \left(\frac{ms}{s+1} \right)^2 \right]} \sin \left(\frac{ms\pi}{s+1} \right), \text{ for } n \neq \frac{ms}{s+1} \quad (\text{A.243})$$

Now for $n = \frac{ms}{s+1}$, using Equations A.228 and A.238 in A.222 yields

$$I_{mn}^3 = -\frac{s}{2} \sin \left(\frac{m\pi}{2s+2} \right), \text{ for } n = \frac{ms}{s+1} \quad (\text{A.244})$$

For $n \neq \frac{ms}{s+1}$, using Equations A.233 A.243 in A.222 yields

$$\begin{aligned}
I_{mn}^3 &= s \cos\left(\frac{m\pi}{2s+2}\right) \frac{n}{\pi \left[n^2 - \left(\frac{ms}{s+1}\right)^2\right]} \left[1 - (-1)^n \cos\left(\frac{ms\pi}{s+1}\right)\right] \\
&\quad + (-1)^n s \sin\left(\frac{m\pi}{2s+2}\right) \frac{n}{\pi \left[n^2 - \left(\frac{ms}{s+1}\right)^2\right]} \sin\left(\frac{ms\pi}{s+1}\right) \\
&= \frac{sn}{\pi \left[n^2 - \left(\frac{ms}{s+1}\right)^2\right]} \cos\left(\frac{m\pi}{2s+2}\right) - \frac{(-1)^n sn}{\pi \left[n^2 - \left(\frac{ms}{s+1}\right)^2\right]} \\
&\quad \cdot \left[\cos\left(\frac{m\pi}{2s+2}\right) \cos\left(\frac{ms\pi}{s+1}\right) - \sin\left(\frac{m\pi}{2s+2}\right) \sin\left(\frac{ms\pi}{s+1}\right) \right]
\end{aligned} \tag{A.245}$$

Using $\cos(\alpha + \beta) = \cos \alpha \cos \beta - \sin \alpha \sin \beta$ yields

$$\begin{aligned}
I_{mn}^3 &= \frac{sn}{\pi \left[n^2 - \left(\frac{ms}{s+1}\right)^2\right]} \left[\cos\left(\frac{m\pi}{2s+2}\right) - (-1)^n \cos\left(\frac{m\pi}{2s+2} + \frac{ms\pi}{s+1}\right) \right] \\
&= \frac{sn}{\pi \left[n^2 - \left(\frac{ms}{s+1}\right)^2\right]} \left[\cos\left(\frac{m\pi}{2s+2}\right) - (-1)^n \cos\left(m\pi \frac{2s+1}{2s+2}\right) \right]
\end{aligned} \tag{A.246}$$

Using $\cos\left(m\pi \frac{2s+1}{2s+2}\right) = (-1)^m \cos\left(\frac{m\pi}{2s+2}\right)$ yields

$$I_{mn}^3 = \frac{sn}{\pi \left[n^2 - \left(\frac{ms}{s+1}\right)^2\right]} \cos\left(\frac{m\pi}{2s+2}\right) [1 - (-1)^{n+m}], \text{ for } n \neq \frac{ms}{s+1} \tag{A.247}$$

Finally,

$$I_{mn}^3 = \begin{cases} -\frac{s}{2} \sin\left(\frac{m\pi}{2s+2}\right) & \text{for } n = \frac{ms}{s+1} \\ \frac{sn}{\pi \left[n^2 - \left(\frac{ms}{s+1}\right)^2\right]} \cos\left(\frac{m\pi}{2s+2}\right) [1 - (-1)^{n+m}] & \text{for } n \neq \frac{ms}{s+1} \end{cases} \tag{A.248}$$

A.9 Summary of Linear Equations

To determine the potential coefficients, the results of matching the boundary conditions at the interfaces between layers 2-3 and 3-4 can be consolidated by combining the resulting equations at each interface. This will establish a final set of equations that the potential coefficients must satisfy to fulfill all boundary conditions. Adding Equations A.181 and A.203 yields

$$a_0 d(s+1) - \sum_{n=1}^{\infty} \frac{2s}{n\pi} b_n \Phi_n^c [1 - (-1)^n] + d_0(s+1) = (s+1)(V_1 + V_2) \quad (\text{A.249})$$

Subtracting Equation A.203 from A.181 yields

$$a_0 d(s+1) + \sum_{n=1}^{\infty} \frac{2s}{n\pi} c_n \Psi_n^c [1 - (-1)^n] - d_0(s+1) = 0 \quad (\text{A.250})$$

Adding Equations A.182 and A.204 yields

$$a_m \Theta_m^c \frac{s+1}{2} - 2 \sum_{n=1}^{\infty} b_n \Phi_n^c I_{mn}^3 + d_m \mathcal{F}_m^4(h) \frac{s+1}{2} = 2\mathcal{I}_m \quad (\text{A.251})$$

Subtracting Equation A.204 from A.182 yields

$$a_m \Theta_m^c \frac{s+1}{2} + 2 \sum_{n=1}^{\infty} c_n \Psi_n^c I_{mn}^3 - d_m \mathcal{F}_m^4(h) \frac{s+1}{2} = 0 \quad (\text{A.252})$$

Adding Equations A.183 and A.205 yields

$$\frac{\epsilon_2 s}{m\pi} [1 - (-1)^m] a_0 + \sum_{n=1}^{\infty} \frac{\epsilon_2 n\pi}{s+1} a_n \Gamma_n^c I_{nm}^3 + \epsilon_3 m\pi b_m \Psi_m^c + \sum_{n=1}^{\infty} \frac{\epsilon_4 n\pi}{s+1} d_n \mathcal{H}_n^4(h) I_{nm}^3 = 0 \quad (\text{A.253})$$

Subtracting Equation A.205 from A.183 yields

$$\frac{\epsilon_2 s}{m\pi} [1 - (-1)^m] a_0 + \sum_{n=1}^{\infty} \frac{\epsilon_2 n\pi}{s+1} a_n \Gamma_n^c I_{nm}^3 - \epsilon_3 m\pi c_m \Phi_m^c - \sum_{n=1}^{\infty} \frac{\epsilon_4 n\pi}{s+1} d_n \mathcal{H}_n^4(h) I_{nm}^3 = 0 \quad (\text{A.254})$$

A.10 Glossary of Variable Quantities

The following Quantities were used to simplify the final expressions:

$$\Theta_m^c = \sinh \left(\frac{m\pi d}{s+1} \right) \quad (\text{A.255})$$

$$\Gamma_n^c = \cosh \left(\frac{n\pi d}{s+1} \right) \quad (\text{A.256})$$

$$\mathcal{F}_m^4(h) = \exp(-\lambda_m l) \left\{ \cosh[\lambda_m(l-h)] + \frac{\epsilon_5}{\epsilon_4} \sinh[\lambda_m(l-h)] \right\} \quad (\text{A.257})$$

$$\mathcal{H}_n^4(h) = \exp(-\lambda_n l) \left\{ \sinh[\lambda_n(l-h)] + \frac{\epsilon_5}{\epsilon_4} \cosh[\lambda_n(l-h)] \right\} \quad (\text{A.258})$$

$$\Phi_n^c = \cosh \left(\frac{n\pi h}{2s} \right) \quad (\text{A.259})$$

$$\Psi_n^c = \sinh\left(\frac{n\pi h}{2s}\right) \quad (\text{A.260})$$

$$\lambda_n = \frac{n\pi}{s+1} \quad (\text{A.261})$$

$$\mathcal{I}_m = \langle V_1, \psi_m^2 \rangle^- + \langle V_2, \psi_m^2 \rangle^+ + I_m^1 + I_m^2 \quad (\text{A.262})$$

$$\langle V_1, \psi_m^2 \rangle^- = \frac{V_1(s+1)}{m\pi} \sin\left(\frac{m\pi}{2s+2}\right) \quad (\text{A.263})$$

$$\langle V_2, \psi_m^2 \rangle^+ = (-1)^m \frac{V_2(s+1)}{m\pi} \sin\left(\frac{m\pi}{2s+2}\right) \quad (\text{A.264})$$

$$\begin{aligned} I_m^1 &= \frac{(V_2 - V_1)(s+1)^2}{sm^2\pi^2} \cos\left(\frac{m\pi}{2s+2}\right) [(-1)^m - 1] \\ &\quad + \frac{(V_2 - V_1)(s+1)}{2m\pi} \sin\left(\frac{m\pi}{2s+2}\right) [1 - (-1)^m] \end{aligned} \quad (\text{A.265})$$

$$I_m^2 = -[1 + (-1)^m] \frac{(V_2 + V_1)(s+1)}{2m\pi} \sin\left(\frac{m\pi}{2s+2}\right) \quad (\text{A.266})$$

$$I_{mn}^3 = \begin{cases} -\frac{s}{2} \sin\left(\frac{m\pi}{2s+2}\right) & \text{for } n = \frac{ms}{s+1} \\ \frac{sn}{\pi[n^2 - (\frac{ms}{s+1})^2]} \cos\left(\frac{m\pi}{2s+2}\right) [1 - (-1)^{n+m}] & \text{for } n \neq \frac{ms}{s+1} \end{cases} \quad (\text{A.267})$$

where the superscript c denotes the capacitive potential solution. In addition, m and n are integers.

Appendix B. Detailed Charge Calculations

To find the total charge on either microstrip, the normal electric flux density is integrated around a contour, which encloses the microstrip. A diagram of the simplified periodic cell is depicted in Figure B.1, which also shows the contour used for the charge calculations.

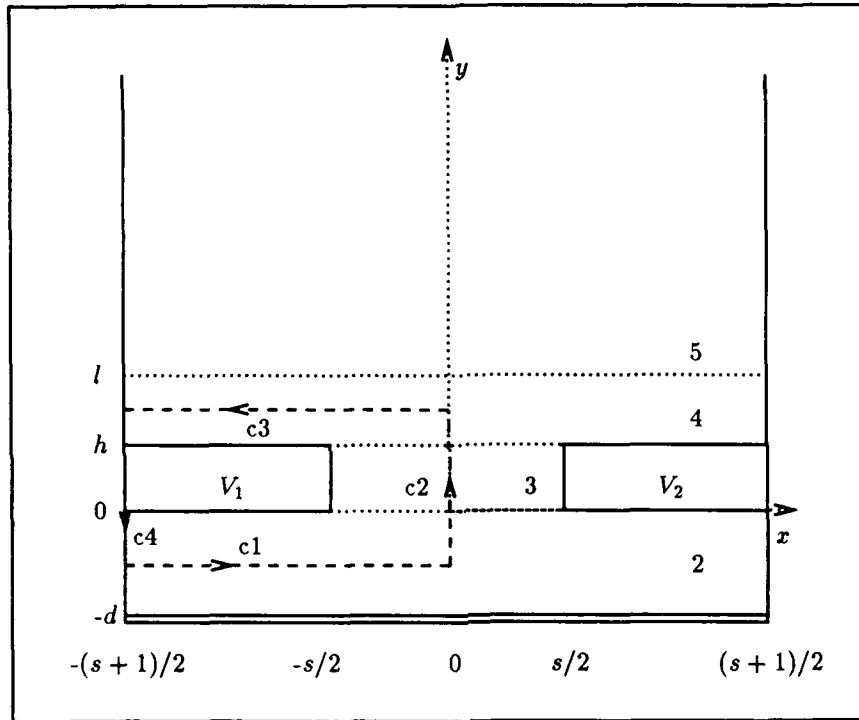


Figure B.1. Contour for Charge Integration

Thus, the charge on the left electrode is

$$Q = \epsilon \oint_{\gamma} E_n dl \quad (\text{B.1})$$

where $\gamma = c1 + c2 + c3 + c4$, which is shown in Figure B.1. This yields

$$\begin{aligned} Q = & \epsilon_2 \int_{-\frac{s+1}{2}}^0 (-E_y) dx + \epsilon_2 \int_{-\frac{s}{2}}^0 E_x dy + \epsilon_3 \int_0^h E_x dy \\ & + \epsilon_4 \int_h^{\frac{l-h}{2}} E_x dy + \epsilon_4 \int_0^{-\frac{s+1}{2}} E_y (-dx) \end{aligned} \quad (\text{B.2})$$

Since $E_x = -\partial\phi/\partial x$, and $E_y = -\partial\phi/\partial y$, then with substitution

$$Q = \epsilon_2 \int_{-\frac{s+1}{2}}^0 \frac{\partial\phi_2}{\partial y} dx - \epsilon_2 \int_{-\frac{s}{2}}^0 \frac{\partial\phi_2}{\partial x} dy - \epsilon_3 \int_0^h \frac{\partial\phi_3}{\partial x} dy - \epsilon_4 \int_h^{\frac{l-h}{2}} \frac{\partial\phi_4}{\partial x} dy - \epsilon_4 \int_{-\frac{s+1}{2}}^0 \frac{\partial\phi_4}{\partial y} dx \quad (B.3)$$

or

$$Q = Q_2^a + Q_2^b + Q_3 + Q_4^a + Q_4^b \quad (B.4)$$

where each integral in order has been assigned a corresponding label. From Equations A.27, A.108, A.109, A.100, A.185, A.188, and A.189

$$\frac{\partial\phi_2}{\partial y} = a_0 + \sum_{n=1}^{\infty} \left(\frac{n\pi}{s+1} \right) a_n \Gamma_n^c(y) \cos \left[n\pi \left(\frac{x}{s+1} + \frac{1}{2} \right) \right] \quad (B.5)$$

$$\frac{\partial\phi_2}{\partial x} = - \sum_{n=1}^{\infty} \left(\frac{n\pi}{s+1} \right) a_n \Theta_n^c(y) \sin \left[n\pi \left(\frac{x}{s+1} + \frac{1}{2} \right) \right] \quad (B.6)$$

$$\begin{aligned} \frac{\partial\phi_3}{\partial x} = & \left(\frac{V_2 - V_1}{s} \right) + \sum_{n=1}^{\infty} \left(\frac{n\pi}{s} \right) \\ & \cdot \left\{ b_n \cosh \left[\frac{n\pi}{s} \left(y - \frac{h}{2} \right) \right] + c_n \sinh \left[\frac{n\pi}{s} \left(y - \frac{h}{2} \right) \right] \right\} \cos \left[n\pi \left(\frac{x}{s} + \frac{1}{2} \right) \right] \end{aligned} \quad (B.7)$$

$$\frac{\partial\phi_4}{\partial x} = - \sum_{n=1}^{\infty} \left(\frac{n\pi}{s+1} \right) d_n \mathcal{F}_n^4(y) \sin \left[n\pi \left(\frac{x}{s+1} + \frac{1}{2} \right) \right] \quad (B.8)$$

$$\frac{\partial\phi_4}{\partial y} = \sum_{n=1}^{\infty} \left(\frac{n\pi}{s+1} \right) d_n \mathcal{H}_n^4(y) \cos \left[n\pi \left(\frac{x}{s+1} + \frac{1}{2} \right) \right] \quad (B.9)$$

where

$$\Gamma_n^c(y) = \cosh[\lambda(y+d)] \quad (B.10)$$

$$\Theta_n^c(y) = \sinh[\lambda(y+d)] \quad (B.11)$$

$$\mathcal{F}_n^4(y) = \exp(-\lambda l) \left\{ \cosh[\lambda(l-y)] + \frac{\epsilon_1}{\epsilon_2} \sinh[\lambda(l-y)] \right\} \quad (B.12)$$

$$\mathcal{H}_n^4(y) = \exp(-\lambda l) \left\{ \sinh[\lambda(l-y)] + \frac{\epsilon_1}{\epsilon_2} \cosh[\lambda(l-y)] \right\} \quad (B.13)$$

$$\lambda = \frac{n\pi}{s+1} \quad (B.14)$$

First Q_2^a , from Equations B.3 and B.4

$$Q_2^a = \epsilon_2 \int_{-\frac{s+1}{2}}^0 a_0 dx + \epsilon_2 \int_{-\frac{s+1}{2}}^0 \sum_{n=1}^{\infty} \left(\frac{n\pi}{s+1} \right) a_n \Gamma_n^c \left(-\frac{d}{2} \right) \cos \left[n\pi \left(\frac{x}{s+1} + \frac{1}{2} \right) \right] dx \quad (\text{B.15})$$

$$Q_2^a = Q_2^{a1} + Q_2^{a2} \quad (\text{B.16})$$

For Q_2^{a1}

$$\begin{aligned} Q_2^{a1} &= \epsilon_2 \int_{-\frac{s+1}{2}}^0 a_0 dx \\ &= \epsilon_2 a_0 \left[0 - \left(-\frac{s+1}{2} \right) \right] \\ Q_2^{a1} &= \frac{1}{2} \epsilon_2 a_0 (s+1) \end{aligned} \quad (\text{B.17})$$

For Q_2^{a2}

$$\begin{aligned} Q_2^{a2} &= \epsilon_2 \int_{-\frac{s+1}{2}}^0 \sum_{n=1}^{\infty} \left(\frac{n\pi}{s+1} \right) a_n \Gamma_n^c \left(-\frac{d}{2} \right) \cos \left[n\pi \left(\frac{x}{s+1} + \frac{1}{2} \right) \right] dx \\ &= \epsilon_2 \sum_{n=1}^{\infty} \left(\frac{n\pi}{s+1} \right) a_n \Gamma_n^c \left(-\frac{d}{2} \right) \int_{-\frac{s+1}{2}}^0 \cos \left[n\pi \left(\frac{x}{s+1} + \frac{1}{2} \right) \right] dx \\ &= \epsilon_2 \sum_{n=1}^{\infty} \left(\frac{n\pi}{s+1} \right) a_n \Gamma_n^c \left(-\frac{d}{2} \right) \left[\frac{s+1}{n\pi} \sin \left[n\pi \left(\frac{x}{s+1} + \frac{1}{2} \right) \right] \right]_{-\frac{s+1}{2}}^0 \\ &= \epsilon_2 \sum_{n=1}^{\infty} a_n \Gamma_n^c \left(-\frac{d}{2} \right) \left[\sin \left(\frac{n\pi}{2} \right) - \sin(0) \right] \\ Q_2^{a2} &= \epsilon_2 \sum_{n=1}^{\infty} a_n \Gamma_n^c \left(-\frac{d}{2} \right) \sin \left(\frac{n\pi}{2} \right) \end{aligned} \quad (\text{B.18})$$

Using Equations B.17 and B.18 in B.16 yields

$$Q_2^a = \frac{1}{2} \epsilon_2 a_0 (s+1) + \epsilon_2 \sum_{n=1}^{\infty} a_n \Gamma_n^c \left(-\frac{d}{2} \right) \sin \left(\frac{n\pi}{2} \right) \quad (\text{B.19})$$

For Q_2^b

$$Q_2^b = \epsilon_2 \int_{-\frac{s+1}{2}}^0 \sum_{n=1}^{\infty} \left(\frac{n\pi}{s+1} \right) a_n \Theta_n^c(y) \sin \left(\frac{n\pi}{2} \right) dy$$

$$= \epsilon_2 \sum_{n=1}^{\infty} \left(\frac{n\pi}{s+1} \right) a_n \sin \left(\frac{n\pi}{2} \right) \int_{-\frac{d}{2}}^0 \Theta_n^c(y) dy \quad (\text{B.20})$$

Evaluating the integral separately yields

$$\begin{aligned} \int_{-\frac{d}{2}}^0 \Theta_n^c(y) dy &= \int_{-\frac{d}{2}}^0 \sinh[\lambda(y+d)] dy \\ &= \left[\frac{s+1}{n\pi} \cosh[\lambda(y+d)] \right]_{-\frac{d}{2}}^0 \\ \int_{-\frac{d}{2}}^0 \Theta_n^c(y) dy &= \frac{s+1}{n\pi} \left[\Gamma_n^c(0) - \Gamma_n^c\left(-\frac{d}{2}\right) \right] \end{aligned} \quad (\text{B.21})$$

Using Equation B.21 in B.20 yields

$$Q_2^b = \epsilon_2 \sum_{n=1}^{\infty} a_n \sin \left(\frac{n\pi}{2} \right) \left[\Gamma_n^c(0) - \Gamma_n^c\left(-\frac{d}{2}\right) \right] \quad (\text{B.22})$$

By letting

$$Q_2 = Q_2^a + Q_2^b \quad (\text{B.23})$$

then

$$\begin{aligned} Q_2 &= \frac{1}{2} \epsilon_2 a_0 (s+1) + \epsilon_2 \sum_{n=1}^{\infty} a_n \Gamma_n^c \left(-\frac{d}{2} \right) \sin \left(\frac{n\pi}{2} \right) \\ &\quad + \epsilon_2 \sum_{n=1}^{\infty} a_n \sin \left(\frac{n\pi}{2} \right) \left[\Gamma_n^c(0) - \Gamma_n^c \left(-\frac{d}{2} \right) \right] \end{aligned} \quad (\text{B.24})$$

or

$$Q_2 = \frac{1}{2} \epsilon_2 a_0 (s+1) + \epsilon_2 \sum_{n=1}^{\infty} a_n \sin \left(\frac{n\pi}{2} \right) \Gamma_n^c \quad (\text{B.25})$$

since

$$\Gamma_n^c(0) - \Gamma_n^c \left(-\frac{d}{2} \right) = \cosh \left(\frac{n\pi d}{s+1} \right) \quad (\text{B.26})$$

Now for Q_3

$$Q_3 = Q_3^a + Q_3^b \quad (\text{B.27})$$

where

$$Q_3^a = -\epsilon_3 \int_0^h \left(\frac{V_2 - V_1}{s} \right) dy \quad (\text{B.28})$$

$$Q_3^b = -\epsilon_3 \int_0^h \sum_{n=1}^{\infty} \frac{n\pi}{s} \cos\left(\frac{n\pi}{2}\right) \cdot \left\{ b_n \cosh \left[\lambda_3 \left(y - \frac{h}{2} \right) \right] + c_n \sinh \left[\lambda_3 \left(y - \frac{h}{2} \right) \right] \right\} dy \quad (\text{B.29})$$

First, evaluating Q_3^a yields

$$Q_3^a = \frac{\epsilon_3}{s} (V_1 - V_2) |y|_0^h = \frac{h\epsilon_3}{s} (V_1 - V_2) \quad (\text{B.30})$$

Now for Q_3^b

$$\begin{aligned} Q_3^b &= -\epsilon_3 \sum_{n=1}^{\infty} \frac{n\pi}{s} \cos\left(\frac{n\pi}{2}\right) \int_0^h \left\{ b_n \cosh \left[\lambda_3 \left(y - \frac{h}{2} \right) \right] + c_n \sinh \left[\lambda_3 \left(y - \frac{h}{2} \right) \right] \right\} dy \\ &= -\epsilon_3 \sum_{n=1}^{\infty} \frac{n\pi}{s} \cos\left(\frac{n\pi}{2}\right) \left| \frac{s}{n\pi} \left\{ b_n \sinh \left[\lambda_3 \left(y - \frac{h}{2} \right) \right] + c_n \cosh \left[\lambda_3 \left(y - \frac{h}{2} \right) \right] \right\} \right|_0^h \\ &= -\epsilon_3 \sum_{n=1}^{\infty} \cos\left(\frac{n\pi}{2}\right) \\ &\quad \cdot \left[b_n \sinh \left(\frac{n\pi h}{2s} \right) - b_n \sinh \left(-\frac{n\pi h}{2s} \right) + c_n \cosh \left(\frac{n\pi h}{2s} \right) - c_n \cosh \left(-\frac{n\pi h}{2s} \right) \right] \\ Q_3^b &= -2\epsilon_3 \sum_{n=1}^{\infty} \cos\left(\frac{n\pi}{2}\right) b_n \sinh \left(\frac{n\pi h}{2s} \right) \end{aligned} \quad (\text{B.31})$$

Using Equations B.30 and B.31 in B.27 yields

$$Q_3 = \frac{h\epsilon_3}{s} (V_1 - V_2) - 2\epsilon_3 \sum_{n=1}^{\infty} \cos\left(\frac{n\pi}{2}\right) b_n \sinh \left(\frac{n\pi h}{2s} \right) \quad (\text{B.32})$$

Now for Q_4^a

$$\begin{aligned} Q_4^a &= \epsilon_4 \int_h^{\frac{l-h}{2}} \sum_{n=1}^{\infty} \left(\frac{n\pi}{s+1} \right) d_n \mathcal{F}_n^4(y) \sin\left(\frac{n\pi}{2}\right) dy \\ &= \epsilon_4 \sum_{n=1}^{\infty} \left(\frac{n\pi}{s+1} \right) \sin\left(\frac{n\pi}{2}\right) \int_h^{\frac{l-h}{2}} \mathcal{F}_n^4(y) dy \end{aligned} \quad (\text{B.33})$$

Evaluating the integral separately yields

$$\begin{aligned}
 \int_h^{\frac{l-h}{2}} \mathcal{F}_n^4(y) dy &= \int_h^{\frac{l-h}{2}} \exp(-\lambda l) \left\{ \cosh[\lambda(l-y)] + \frac{\epsilon_5}{\epsilon_4} \sinh[\lambda(l-y)] \right\} dy \\
 &= -\exp(-\lambda l) \left| \frac{s+1}{n\pi} \left\{ \sinh[\lambda(l-y)] + \frac{\epsilon_5}{\epsilon_4} \cosh[\lambda(l-y)] \right\} \right|_h^{\frac{l-h}{2}} \\
 &= -\frac{s+1}{n\pi} \left[\mathcal{H}_n^4\left(\frac{l-h}{2}\right) - \mathcal{H}_n^4(h) \right] \\
 \int_h^{\frac{l-h}{2}} \mathcal{F}_n^4(y) dy &= \frac{s+1}{n\pi} \left[\mathcal{H}_n^4(h) - \mathcal{H}_n^4\left(\frac{l-h}{2}\right) \right]
 \end{aligned} \tag{B.34}$$

Using Equation B.34 in B.33 yields

$$Q_4^a = \epsilon_4 \sum_{n=1}^{\infty} d_n \sin\left(\frac{n\pi}{2}\right) \left[\mathcal{H}_n^4(h) - \mathcal{H}_n^4\left(\frac{l-h}{2}\right) \right] \tag{B.35}$$

Next, evaluating Q_4^b yields

$$\begin{aligned}
 Q_4^b &= -\epsilon_4 \int_{-\frac{s+1}{2}}^0 \left\{ -\sum_{n=1}^{\infty} \frac{n\pi}{s+1} d_n \mathcal{H}_n^4\left(\frac{l-h}{2}\right) \cos\left[n\pi\left(\frac{x}{s+1} + \frac{1}{2}\right)\right] \right\} dx \\
 &= \epsilon_4 \sum_{n=1}^{\infty} \frac{n\pi}{s+1} d_n \mathcal{H}_n^4\left(\frac{l-h}{2}\right) \int_{-\frac{s+1}{2}}^0 \cos\left[n\pi\left(\frac{x}{s+1} + \frac{1}{2}\right)\right] dx \\
 &= \epsilon_4 \sum_{n=1}^{\infty} \frac{n\pi}{s+1} d_n \mathcal{H}_n^4\left(\frac{l-h}{2}\right) \left| \frac{s+1}{n\pi} \sin\left[n\pi\left(\frac{x}{s+1} + \frac{1}{2}\right)\right] \right|_{-\frac{s+1}{2}}^0 \\
 &= \epsilon_4 \sum_{n=1}^{\infty} \frac{n\pi}{s+1} d_n \mathcal{H}_n^4\left(\frac{l-h}{2}\right) \left[\sin\left(\frac{n\pi}{2}\right) - \sin(0) \right] \\
 Q_4^b &= \epsilon_4 \sum_{n=1}^{\infty} \frac{n\pi}{s+1} d_n \mathcal{H}_n^4\left(\frac{l-h}{2}\right) \sin\left(\frac{n\pi}{2}\right)
 \end{aligned} \tag{B.36}$$

By letting

$$Q_4 = Q_4^a + Q_4^b \tag{B.37}$$

then substituting Equations B.35 and B.36 in B.37 yields

$$\begin{aligned}
 Q_4 &= \epsilon_4 \sum_{n=1}^{\infty} d_n \sin\left(\frac{n\pi}{2}\right) \left[\mathcal{H}_n^4(h) - \mathcal{H}_n^4\left(\frac{l-h}{2}\right) \right] \\
 &\quad + \epsilon_4 \sum_{n=1}^{\infty} \frac{n\pi}{s+1} d_n \mathcal{H}_n^4\left(\frac{l-h}{2}\right) \sin\left(\frac{n\pi}{2}\right)
 \end{aligned} \tag{B.38}$$

Hence,

$$Q_4 = \epsilon_4 \sum_{n=1}^{\infty} d_n \sin\left(\frac{n\pi}{2}\right) \mathcal{H}_n^4(h) \quad (\text{B.39})$$

Total Charge. The total charge enclosed on the left electrode (see Figure B.1) can be determined by substituting Equations B.25, B.32, and B.39 into Equation B.4, which yields

$$\begin{aligned} Q = & \frac{1}{2} \epsilon_2 a_0 (s+1) + \epsilon_2 \sum_{n=1}^{\infty} a_n \sin\left(\frac{n\pi}{2}\right) \Gamma_n^c + \frac{h\epsilon_3}{s} (V_1 - V_2) \\ & - 2\epsilon_3 \sum_{n=1}^{\infty} \cos\left(\frac{n\pi}{2}\right) b_n \sinh\left(\frac{n\pi h}{2s}\right) + \epsilon_4 \sum_{n=1}^{\infty} d_n \sin\left(\frac{n\pi}{2}\right) \mathcal{H}_n^4(h) \end{aligned} \quad (\text{B.40})$$

Appendix C. Detailed Resistive Potential Solution

To determine the resistive element of the model, the potential distribution within the sensor coating layer is solved, using the low frequency boundary conditions on the interfaces to the dielectric layers. First, the conductive layer is divided into three regions, corresponding to the specified boundary data. Using the separation of variables technique on Laplace's equation, the potentials within each region are determined to be infinite Fourier series. The Fourier coefficients are determined by enforcing boundary conditions at the interfaces between the regions. A diagram of the conductive layer is depicted in Figure C.1, where the x axis has been translated by $-h$, so that $0 < y < p$, where $p = l - h$. For the resistance calculations, only the odd symmetry case of $V_1 = -V_2 = 1/2$ volt is considered, since no electric flux exists between the two electrodes with even symmetry ($V_1 = V_2$).

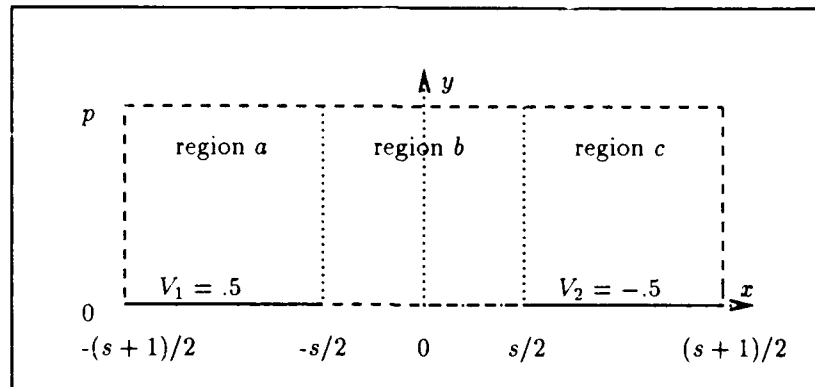


Figure C.1. Diagram of resistive layer for detailed solution

C.1 Potential Solution for Region a

Region a is the left region with $-(s+1)/2 \leq x \leq s/2$. From Figure C.1 and Equation 3.80, the potential within region a, ϕ_a , must satisfy the following conditions:

$$\nabla^2 \phi_a = 0 \quad (C.1)$$

$$\phi_a(x, 0) = \frac{1}{2} \quad (C.2)$$

$$\frac{\partial \phi_a}{\partial y}(x, p) = 0 \quad (C.3)$$

$$\frac{\partial \phi_a}{\partial x} \left(-\frac{s+1}{2}, y \right) = 0 \quad (C.4)$$

First, we seek a solution of the form

$$\phi_a(x, y) = v_a(y) + \omega_a(x, y) \quad (C.5)$$

where v_a is chosen to satisfy the non-homogenous boundary condition at the lower boundary. A selected value of

$$v_a = \frac{1}{2} \quad (C.6)$$

satisfies Equations C.1, C.2, C.3, and C.4. Therefore, ω_a must satisfy

$$\nabla^2 \omega_a = 0 \quad (C.7)$$

$$\omega_a(x, 0) = 0 \quad (C.8)$$

$$\frac{\partial \omega_a}{\partial y}(x, p) = 0 \quad (C.9)$$

$$\frac{\partial \omega_a}{\partial x} \left(-\frac{s+1}{2}, y \right) = 0 \quad (C.10)$$

To determine ω_a , we seek a solution of the form

$$\omega_a(x, y) = \Psi(x)\Phi(y) \quad (C.11)$$

Using Equation C.11 in C.7 yields

$$\Psi''\Phi + \Psi\Phi'' = 0 \quad (\text{C.12})$$

or

$$\frac{\Psi''}{\Psi} + \frac{\Phi''}{\Phi} = 0 \quad (\text{C.13})$$

Hence,

$$\frac{\Phi''}{\Phi} = -\frac{\Psi''}{\Psi} = -\lambda_a^2 \quad (\text{C.14})$$

where λ_a is the separation constant or eigenvalue for region a . Thus,

$$\Phi'' + \lambda_a^2 \Phi = 0 \quad (\text{C.15})$$

or

$$\Phi(y) = A \cos(\lambda_a y) + B \sin(\lambda_a y) \quad (\text{C.16})$$

Enforcing Equation C.8 yields

$$\Phi(0) = A = 0 \quad (\text{C.17})$$

Thus

$$\Phi(y) = B \sin(\lambda_a y) \quad (\text{C.18})$$

$$\Phi'(y) = B \lambda_a \cos(\lambda_a y) \quad (\text{C.19})$$

Enforcing Equation C.9 yields

$$\Phi'(p) = B \lambda_a \cos(\lambda_a p) = 0 \quad (\text{C.20})$$

Hence

$$\lambda_a = \frac{n\pi}{2p} \quad \text{for } n = 1, 3, 5, \dots \quad (\text{C.21})$$

or

$$\lambda_a = \frac{(2n-1)\pi}{2p} \quad \text{for } n = 1, 2, 3, 4, \dots \quad (\text{C.22})$$

For $\lambda_a = 0$, Equation C.15 reduces to

$$\Phi'' = 0 \quad (\text{C.23})$$

or

$$\Phi(y) = A_0 y + B_0 \quad (\text{C.24})$$

Enforcing Equation C.8 yields

$$\Phi(0) = B_0 = 0 \quad (\text{C.25})$$

Therefore,

$$\Phi(y) = A_0 y \quad (\text{C.26})$$

$$\Phi'(y) = A_0 \quad (\text{C.27})$$

Enforcing Equation C.9 yields

$$\Phi'(0) = A_0 = 0 \quad (\text{C.28})$$

which indicates that $\lambda_a = 0$ is not a possible eigenvalue. Thus, the complete eigenfunction is

$$\Phi_n(y) = B_n \sin \left[\frac{(2n-1)\pi y}{2p} \right] \quad (\text{C.29})$$

To determine $\Psi(x)$, let $\tilde{x} = x + (s+1)/2$, then $\tilde{\Psi}(\tilde{x}) = \Psi(x)$, and $\partial^2 \tilde{\Psi} / \partial \tilde{x}^2 = \partial^2 \Psi / \partial x^2$. Thus

$$\tilde{\Psi}'' - \lambda_a^2 \tilde{\Psi} = 0 \quad (\text{C.30})$$

or

$$\tilde{\Psi}_n(\tilde{x}) = C_n \cosh(\lambda_a \tilde{x}) + D_n \sinh(\lambda_a \tilde{x}) \quad (C.31)$$

$$\tilde{\Psi}'_n(\tilde{x}) = C_n \lambda_a \sinh(\lambda_a \tilde{x}) + D_n \lambda_a \cosh(\lambda_a \tilde{x}) \quad (C.32)$$

Enforcing Equation C.10 yields ($x = -\frac{s+1}{2}$ implies that $\tilde{x} = 0$)

$$\tilde{\Psi}'_n(0) = D_n \lambda_a = 0 \quad (C.33)$$

or $D_n = 0$. Thus,

$$\tilde{\Psi}_n(\tilde{x}) = C_n \cosh(\lambda_a \tilde{x}) \quad (C.34)$$

Hence,

$$\Psi_n(x) = C_n \cosh \left[\frac{(2n-1)\pi}{2p} \left(x + \frac{s+1}{2} \right) \right] \quad (C.35)$$

Using Equation C.29 and C.35 in C.11 yields

$$\omega_a(x, y) = \sum_{n=1}^{\infty} e_n \cosh \left[\frac{(2n-1)\pi}{2p} \left(x + \frac{s+1}{2} \right) \right] \cdot \sin \left[\frac{(2n-1)\pi y}{2p} \right] \quad (C.36)$$

where $e_n = B_n \cdot C_n$. Using Equations C.6 and C.36 in C.5 yields

$$\phi_a(x, y) = \frac{1}{2} + \sum_{n=1}^{\infty} e_n \cosh \left[\frac{(2n-1)\pi}{2p} \left(x + \frac{s+1}{2} \right) \right] \cdot \sin \left[\frac{(2n-1)\pi y}{2p} \right] \quad (C.37)$$

C.2 Potential Solution for Region b

Region b is the middle region with $-s/2 \leq x \leq s/2$. From Figure C.1, Equation 3.79, and Equation 3.80, the potential within region b, ϕ_b , must satisfy the following conditions:

$$\nabla^2 \phi_b = 0 \quad (C.38)$$

$$\frac{\partial \phi_b}{\partial y}(x, 0) = 0 \quad (C.39)$$

$$\frac{\partial \phi_b}{\partial y}(x, p) = 0 \quad (\text{C.40})$$

$$(\text{C.41})$$

First, we seek a solution of the form

$$\phi_b(x, y) = \Psi(x)\Phi(y) \quad (\text{C.42})$$

Using Equation C.42 in C.38 yields

$$\Psi''\Phi + \Psi\Phi'' = 0 \quad (\text{C.43})$$

or

$$\frac{\Psi''}{\Psi} + \frac{\Phi''}{\Phi} = 0 \quad (\text{C.44})$$

Hence,

$$\frac{\Phi''}{\Phi} = -\frac{\Psi''}{\Psi} = -\lambda_b^2 \quad (\text{C.45})$$

where λ_b is the separation constant or eigenvalue for region b . Thus,

$$\Phi'' + \lambda_b^2 \Phi = 0 \quad (\text{C.46})$$

or

$$\Phi(y) = A \cos(\lambda_b y) + B \sin(\lambda_b y) \quad (\text{C.47})$$

$$\Phi'(y) = -A\lambda_b \sin(\lambda_b y) + B\lambda_b \cos(\lambda_b y) \quad (\text{C.48})$$

Enforcing Equation C.39 yields

$$\Phi'(0) = B\lambda_b = 0 \quad (\text{C.49})$$

or $B = 0$. Enforcing Equation C.40 yields

$$\Phi'(p) = A\lambda_b \sin(\lambda_b p) = 0 \quad (C.50)$$

Thus,

$$\lambda_b = \frac{n\pi}{p} \quad \text{for } n = 1, 2, 3, \dots \quad (C.51)$$

For $\lambda_b = 0$, Equation C.46 reduces to

$$\Phi'' = 0 \quad (C.52)$$

or

$$\Phi(y) = A_0 y + B_0 \quad (C.53)$$

Enforcing Equation C.39 or C.40 yields

$$\Phi(0) = A_0 = 0 \quad (C.54)$$

Consequently,

$$\Phi_0(y) = B_0 \quad (C.55)$$

Thus, the complete eigenfunction is

$$\Phi(y) = \begin{cases} B_0 & \text{for } n = 0 \\ B_n \cos\left(\frac{n\pi y}{p}\right) & \text{for } n \neq 0 \end{cases} \quad (C.56)$$

Now for $\Psi(x)$

$$\Psi'' - \lambda_b^2 \Psi = 0 \quad (C.57)$$

or

$$\Psi_n(x) = C_n \cosh(\lambda_b x) + D_n \sinh(\lambda_b x) \quad (C.58)$$

For $\lambda_b = 0$

$$\Psi'' = 0 \quad (C.59)$$

or

$$\Psi_0 = C_0 x + D_0 \quad (C.60)$$

Thus, the complete x function is

$$\Psi(x) = \begin{cases} C_0 x + D_0 & \text{for } n = 0 \\ C_n \cosh\left(\frac{n\pi x}{p}\right) + D_n \sinh\left(\frac{n\pi x}{p}\right) & \text{for } n \neq 0 \end{cases} \quad (C.61)$$

Using Equation C.56 and C.61 in C.42 yields

$$\phi_b(x, y) = f_0 x + g_0 + \sum_{n=1}^{\infty} \left[f_n \cosh\left(\frac{n\pi x}{p}\right) + g_n \sinh\left(\frac{n\pi x}{p}\right) \right] \cdot \cos\left(\frac{n\pi y}{p}\right) \quad (C.62)$$

where

$$f_0 = B_0 \cdot C_0 \quad (C.63)$$

$$g_0 = B_0 \cdot D_0 \quad (C.64)$$

$$f_n = B_n \cdot C_n \quad (C.65)$$

$$g_n = B_n \cdot D_n \quad (C.66)$$

From Figure C.1, the potential in the conductive layer has odd symmetry since (for $s/2 \leq x \leq (s+1)/2$)

$$\phi(x, 0) = -\frac{1}{2} \quad (C.67)$$

$$\phi(-x, 0) = \frac{1}{2} \quad (C.68)$$

Since region b is the central region, its potential will also have odd symmetry. Thus,

$$\phi_b(x, y) = -\phi_b(-x, y) \quad (C.69)$$

or

$$\phi_b(x, y) + \phi_b(-x, y) = 0 \quad (C.70)$$

Using Equation C.62 in C.70 yields

$$2g_0 + 2 \sum_{n=1}^{\infty} f_n \cosh\left(\frac{n\pi x}{p}\right) \cos\left(\frac{n\pi y}{p}\right) = 0 \quad (C.71)$$

Thus (using orthogonality of cosine function)

$$g_0 = 0 \quad (C.72)$$

$$f_n = 0 \quad (C.73)$$

Hence,

$$\phi_b(x, y) = f_0 x + \sum_{n=1}^{\infty} g_n \sinh\left(\frac{n\pi x}{p}\right) \cos\left(\frac{n\pi y}{p}\right) \quad (C.74)$$

C.3 Potential Solution for Region c

Region c is the right region with $s/2 \leq x \leq (s+1)/2$. From Figure C.1 and Equation 3.80, the potential within region c, ϕ_c , must satisfy the following conditions:

$$\nabla^2 \phi_c = 0 \quad (C.75)$$

$$\phi_c(x, 0) = -\frac{1}{2} \quad (C.76)$$

$$\frac{\partial \phi_c}{\partial y}(x, p) = 0 \quad (C.77)$$

$$\frac{\partial \phi_c}{\partial x}\left(\frac{s+1}{2}, y\right) = 0 \quad (C.78)$$

First, we seek a solution of the form

$$\phi_c(x, y) = v_c(y) + \omega_c(x, y) \quad (C.79)$$

where v_c is chosen to satisfy the non-homogenous boundary condition at the lower boundary. The function

$$v_c = -\frac{1}{2} \quad (C.80)$$

satisfies Equations C.75, C.76, C.77, and C.78. Therefore, ω_c must satisfy

$$\nabla^2 \omega_c = 0 \quad (C.81)$$

$$\omega_c(x, 0) = 0 \quad (C.82)$$

$$\frac{\partial \omega_c}{\partial y}(x, p) = 0 \quad (C.83)$$

$$\frac{\partial \omega_c}{\partial x}\left(\frac{s+1}{2}, y\right) = 0 \quad (C.84)$$

For ω_c , we seek a solution of the form

$$\omega_c(x, y) = \Psi(x)\Phi(y) \quad (C.85)$$

Using Equation C.85 in C.81 yields

$$\Psi''\Phi + \Psi\Phi'' = 0 \quad (C.86)$$

or

$$\frac{\Psi''}{\Psi} + \frac{\Phi''}{\Phi} = 0 \quad (C.87)$$

Hence,

$$\frac{\Phi''}{\Phi} = -\frac{\Psi''}{\Psi} = -\lambda_c^2 \quad (C.88)$$

where λ_c is the separation constant or eigenvalue for region c . Thus,

$$\Phi'' + \lambda_c^2 \Phi = 0 \quad (C.89)$$

Since this result is identical to region a , including boundary conditions, region c will have the identical eigenfunction. From Equation C.29

$$\Phi_n(y) = B_n \sin \left[\frac{(2n-1)\pi y}{2p} \right] \quad (\text{C.90})$$

and

$$\lambda_c = \frac{(2n-1)\pi}{2p} \quad \text{for } n = 1, 2, 3, 4, \dots \quad (\text{C.91})$$

To determine $\Psi(x)$, let $\tilde{x} = x - (s+1)/2$. Then $\tilde{\Psi}(\tilde{x}) = \Psi(x)$, and $\partial^2 \tilde{\Psi} / \partial \tilde{x}^2 = \partial^2 \Psi / \partial x^2$. Thus,

$$\tilde{\Psi}'' - \lambda_c^2 \tilde{\Psi} = 0 \quad (\text{C.92})$$

or

$$\tilde{\Psi}_n(\tilde{x}) = C_n \cosh(\lambda_c \tilde{x}) + D_n \sinh(\lambda_c \tilde{x}) \quad (\text{C.93})$$

$$\tilde{\Psi}'_n(\tilde{x}) = C_n \lambda_c \sinh(\lambda_c \tilde{x}) + D_n \lambda_c \cosh(\lambda_c \tilde{x}) \quad (\text{C.94})$$

Enforcing Equation C.84 yields ($x = \frac{s+1}{2}$ implies that $\tilde{x} = 0$)

$$\tilde{\Psi}'_n(0) = D_n \lambda_c = 0 \quad (\text{C.95})$$

or $D_n = 0$. Thus,

$$\tilde{\Psi}_n(\tilde{x}) = C_n \cosh(\lambda_c \tilde{x}) \quad (\text{C.96})$$

or

$$\Psi_n(x) = C_n \cosh \left[\frac{(2n-1)\pi}{2p} \left(x - \frac{s+1}{2} \right) \right] \quad (\text{C.97})$$

Using Equation C.90 and C.97 in C.85 yields

$$\omega_c(x, y) = \sum_{n=1}^{\infty} h_n \cosh \left[\frac{(2n-1)\pi}{2p} \left(x - \frac{s+1}{2} \right) \right] \cdot \sin \left[\frac{(2n-1)\pi y}{2p} \right] \quad (\text{C.98})$$

where $h_n = B_n \cdot C_n$. Using Equations C.80 and C.98 in C.79 yields

$$\phi_c(x, y) = -\frac{1}{2} + \sum_{n=1}^{\infty} h_n \cosh \left[\frac{(2n-1)\pi}{2p} \left(x - \frac{s+1}{2} \right) \right] \cdot \sin \left[\frac{(2n-1)\pi y}{2p} \right] \quad (C.99)$$

Referring to Figure C.1, for $s/2 \leq x \leq (s+1)/2$

$$\phi(x, y) = \phi_c(x, y) \quad (C.100)$$

while

$$\phi(-x, y) = \phi_a(-x, y) \quad (C.101)$$

In addition, for $s/2 \leq x \leq (s+1)/2$

$$\phi(x, 0) = -\frac{1}{2} \quad (C.102)$$

$$\phi(-x, 0) = \frac{1}{2} \quad (C.103)$$

which represents odd symmetry. Thus for entire problem, we must also have odd symmetry. Hence,

$$\phi(x, y) = -\phi(-x, y) \quad (C.104)$$

or

$$\phi_c(x, y) + \phi_a(-x, y) = 0 \quad (C.105)$$

Using Equations C.37 and C.99 in C.105 yields

$$\sum_{n=1}^{\infty} (e_n + h_n) \cosh \left[\frac{(2n-1)\pi}{2p} \left(x - \frac{s+1}{2} \right) \right] \sin \left[\frac{(2n-1)\pi y}{2p} \right] = 0 \quad (C.106)$$

or $h_n = -e_n$. Thus,

$$\phi_c(x, y) = -\frac{1}{2} - \sum_{n=1}^{\infty} e_n \cosh \left[\frac{(2n-1)\pi}{2p} \left(x - \frac{s+1}{2} \right) \right] \cdot \sin \left[\frac{(2n-1)\pi y}{2p} \right] \quad (C.107)$$

C.4 Boundary Between Regions

The potential must be continuous across the interface between regions. In addition, the x component of the electric field must also be continuous across the interface, since the continuity has the same value in each region. Due to symmetry, either interface (between regions a and b , or between regions b and c) will produce the same boundary equations. Therefore, the interface between regions a and b will be evaluated ($x = -s/2$). From the above discussion, the region potentials must satisfy the following conditions:

$$\phi_a(-\frac{s}{2}, y) = \phi_b(-\frac{s}{2}, y) \quad (C.108)$$

$$\frac{\partial \phi_a}{\partial x}(-\frac{s}{2}, y) = \frac{\partial \phi_b}{\partial x}(-\frac{s}{2}, y) \quad (C.109)$$

From Equation C.37

$$\phi_a = \frac{1}{2} + \sum_{n=1}^{\infty} e_n \cosh \left[\frac{(2n-1)\pi}{2p} \left(x + \frac{s+1}{2} \right) \right] \sin \left[\frac{(2n-1)\pi y}{2p} \right] \quad (C.110)$$

and

$$\frac{\partial \phi_a}{\partial x} = \sum_{n=1}^{\infty} \frac{(2n-1)\pi}{2p} e_n \sinh \left[\frac{(2n-1)\pi}{2p} \left(x + \frac{s+1}{2} \right) \right] \sin \left[\frac{(2n-1)\pi y}{2p} \right] \quad (C.111)$$

From Equation C.74

$$\phi_b = f_0 x + \sum_{n=1}^{\infty} g_n \sinh \left(\frac{n\pi x}{p} \right) \cos \left(\frac{n\pi y}{p} \right) \quad (C.112)$$

and

$$\frac{\partial \phi_b}{\partial x} = f_0 + \sum_{n=1}^{\infty} \frac{n\pi}{p} g_n \cosh \left(\frac{n\pi x}{p} \right) \cos \left(\frac{n\pi y}{p} \right) \quad (C.113)$$

Using Equations C.110 and C.112 in C.108 yields

$$\frac{1}{2} + \sum_{n=1}^{\infty} e_n \Gamma_n^r \psi_n^a(y) = -\frac{s}{2} f_0 - \sum_{n=1}^{\infty} g_n \Psi_n^r \psi_n^b(y) \quad (C.114)$$

where

$$\Gamma_n^r = \cosh \left[\frac{(2n-1)\pi}{4p} \right] \quad (\text{C.115})$$

$$\Psi_n^r = \sinh \left(\frac{n\pi s}{2p} \right) \quad (\text{C.116})$$

$$\psi_n^a(y) = \sin \left[\frac{(2n-1)\pi y}{2p} \right] \quad (\text{C.117})$$

$$\psi_n^b(y) = \cos \left(\frac{n\pi y}{p} \right) \quad (\text{C.118})$$

The r superscript denotes quantities used in the resistive potential solution. The f_n and g_n terms are "sifted" by multiplying Equation C.114 by $\psi_m^b(y)$ and integrating over y ($0 \leq y \leq p$). Accordingly,

$$\frac{1}{2} \langle 1, 1 \rangle = \sum_{n=1}^{\infty} e_n \Gamma_n^r \langle \psi_n^a, 1 \rangle = - \frac{s}{2} f_0 \langle 1, 1 \rangle \quad (\text{C.119})$$

and

$$\sum_{n=1}^{\infty} e_n \Gamma_n^r \langle \psi_n^a, \psi_m^b \rangle = - \sum_{n=1}^{\infty} g_n \Psi_n \langle \psi_n^b, \psi_m^b \rangle \quad (\text{C.120})$$

where

$$\langle f(y), g(y) \rangle = \int_0^p f(y) \cdot g(y) dy \quad (\text{C.121})$$

Evaluating the various inner products yields

$$\langle 1, 1 \rangle = \int_0^p dy = p \quad (\text{C.122})$$

and

$$\begin{aligned} \langle \psi_n^a, 1 \rangle &= \int_0^p \sin \left[\frac{(2n-1)\pi y}{2p} \right] dy \\ &= - \frac{2p}{(2n-1)\pi} \left[\cos \left[\frac{(2n-1)\pi y}{2p} \right] \right]_0^p \\ &= - \frac{2p}{(2n-1)\pi} \left\{ \cos \left[\frac{(2n-1)\pi}{2} \right] - 1 \right\} \\ \langle \psi_n^a, 1 \rangle &= \frac{2p}{(2n-1)\pi} \end{aligned} \quad (\text{C.123})$$

Evaluating $\langle \psi_n^a, \psi_m^b \rangle$ yields

$$\langle \psi_n^b, \psi_m^b \rangle = \int_0^p \cos\left(\frac{n\pi y}{p}\right) \cdot \cos\left(\frac{m\pi y}{p}\right) dy \quad (C.124)$$

To simplify the algebra, let $\tau = \frac{\pi y}{p}$. Then $\frac{p}{\pi} d\tau = dy$, and

$$\langle \psi_n^b, \psi_m^b \rangle = \frac{p}{\pi} \int_0^\pi \cos(n\tau) \cdot \cos(m\tau) d\tau \quad (C.125)$$

Using (for integers a and b)

$$\int_0^\pi (\cos ax)(\cos bx) dx = \begin{cases} 0 & \text{for } a \neq b \\ \frac{\pi}{2} & \text{for } a = b \end{cases} \quad (C.126)$$

yields

$$\langle \psi_n^b, \psi_m^b \rangle = \begin{cases} 0 & \text{for } n \neq m \\ \frac{p}{2} & \text{for } n = m \end{cases} \quad (C.127)$$

Evaluating $\langle \psi_n^a, \psi_m^b \rangle$ yields

$$\langle \psi_n^a, \psi_m^b \rangle = \int_0^p \sin\left[\frac{(2n-1)\pi y}{2p}\right] \cos\left(\frac{m\pi y}{p}\right) dy \quad (C.128)$$

To simplify the analysis, let $\tau = \frac{\pi y}{p}$, and $\tilde{n} = \frac{(2n-1)}{2}$. Accordingly,

$$\langle \psi_n^a, \psi_m^b \rangle = \frac{p}{\pi} \int_0^\pi \sin(\tilde{n}\tau) \cos(m\tau) d\tau \quad (C.129)$$

Using (for $\alpha^2 \neq \beta^2$)

$$\int (\sin \alpha x)(\cos \beta x) dx = -\frac{\cos(\alpha - \beta)x}{2(\alpha - \beta)} - \frac{\cos(\alpha + \beta)x}{2(\alpha + \beta)} \quad (C.130)$$

yields

$$\begin{aligned} \langle \psi_n^a, \psi_m^b \rangle &= -\frac{p}{\pi} \left[\frac{\cos(\tilde{n} - m)\tau}{2(\tilde{n} - m)} + \frac{\cos(\tilde{n} + m)\tau}{2(\tilde{n} + m)} \right]_0^\pi \\ &= -\frac{p}{\pi} \left\{ \frac{\cos[(\tilde{n} - m)\pi] - 1}{2(\tilde{n} - m)} + \frac{\cos[(\tilde{n} + m)\pi] - 1}{2(\tilde{n} + m)} \right\} \\ &= \frac{p}{\pi} \left\{ \frac{1}{2(\tilde{n} - m)} + \frac{1}{2(\tilde{n} + m)} - \frac{\cos[(\tilde{n} - m)\pi]}{2(\tilde{n} - m)} - \frac{\cos[(\tilde{n} + m)\pi]}{2(\tilde{n} + m)} \right\} \end{aligned} \quad (C.131)$$

Since

$$\cos(\alpha \pm \beta) = \cos \alpha \cos \beta \mp \sin \alpha \sin \beta \quad (\text{C.132})$$

then

$$\cos[(\tilde{n} - m)\pi] = \cos(\tilde{n}\pi) \cos(m\pi) + \sin(\tilde{n}\pi) \sin(m\pi) \quad (\text{C.133})$$

$$\cos[(\tilde{n} + m)\pi] = \cos(\tilde{n}\pi) \cos(m\pi) - \sin(\tilde{n}\pi) \sin(m\pi) \quad (\text{C.134})$$

Using $\sin(m\pi) = 0$ and $\cos(\tilde{n}\pi) = \cos\left[\frac{(2n-1)\pi}{2}\right] = 0$ yields

$$\cos[(\tilde{n} \pm m)\pi] = 0 \quad (\text{C.135})$$

Thus

$$\langle \psi_n^a, \psi_m^b \rangle = \frac{p\tilde{n}}{\pi(\tilde{n}^2 - m^2)} \quad (\text{C.136})$$

or

$$\langle \psi_n^a, \psi_m^b \rangle = \frac{p(2n-1)}{2\pi\left[\left(\frac{(2n-1)}{2}\right)^2 - m^2\right]} = \frac{2p(2n-1)}{\pi[(2n-1)^2 - 4m^2]} \quad (\text{C.137})$$

Using Equations C.122 and C.123 in C.119 yields

$$\frac{p}{2} + \sum_{n=1}^{\infty} e_n \Gamma_n^r \frac{2p}{(2n-1)\pi} = -\frac{s}{2} f_0 p \quad (\text{C.138})$$

or

$$\left(\sum_{n=1}^{\infty} e_n \Gamma_n^r \frac{2}{(2n-1)\pi} \right) + \frac{s}{2} f_0 = -\frac{1}{2} \quad (\text{C.139})$$

Using Equations C.127 and C.137 in C.120 yields

$$\sum_{n=1}^{\infty} e_n \Gamma_n^r \frac{2p(2n-1)}{\pi[(2n-1)^2 - 4m^2]} = \frac{p}{2} (-g_m \Psi_m^r) \quad (\text{C.140})$$

or

$$g_m = -\frac{1}{\Psi_m^r} \sum_{n=1}^{\infty} e_n \Gamma_n^r \frac{4(2n-1)}{\pi [(2n-1)^2 - 4m^2]} \quad (\text{C.141})$$

Using Equations C.111 and C.113 in C.109 yields

$$\sum_{n=1}^{\infty} \frac{(2n-1)\pi}{2p} e_n \Theta_n^r \psi_n^a(y) = f_0 + \sum_{n=1}^{\infty} \frac{n\pi}{p} g_n \Phi_n^r \psi_n^b(y) \quad (\text{C.142})$$

where

$$\Theta_n^r = \sinh \left[\frac{(2n-1)\pi}{4p} \right] \quad (\text{C.143})$$

$$\Phi_n^r = \cosh \left(\frac{n\pi s}{2p} \right) \quad (\text{C.144})$$

Again, the superscript r denotes quantities used in the resistive potential solution. Sifting Equation C.142 with ψ_m^b yields

$$\sum_{n=1}^{\infty} \frac{(2n-1)\pi}{2p} e_n \Theta_n^r \langle \psi_n^a, 1 \rangle = f_0 \langle 1, 1 \rangle \quad (\text{C.145})$$

and

$$\sum_{n=1}^{\infty} \frac{(2n-1)\pi}{2p} e_n \Theta_n^r \langle \psi_n^a, \psi_m^b \rangle = \sum_{n=1}^{\infty} \frac{n\pi}{p} g_n \Phi_n^r \langle \psi_n^b, \psi_m^b \rangle \quad (\text{C.146})$$

Using Equations C.122 and C.123 in C.145 yields

$$\sum_{n=1}^{\infty} \frac{(2n-1)\pi}{2p} e_n \Theta_n^r \frac{2p}{(2n-1)\pi} = f_0 p \quad (\text{C.147})$$

or

$$f_0 = \frac{1}{p} \sum_{n=1}^{\infty} e_n \Theta_n^r \quad (\text{C.148})$$

Using Equation C.148 in C.139 yields

$$\sum_{n=1}^{\infty} e_n \left[\Gamma_n^r \frac{2}{(2n-1)\pi} + \frac{s}{2p} \Theta_n^r \right] = -\frac{1}{2} \quad (\text{C.149})$$

Using Equations C.127 and C.137 in C.146 yields

$$\sum_{n=1}^{\infty} \frac{(2n-1)\pi}{2p} e_n \Theta_n^r \frac{2p(2n-1)}{\pi [(2n-1)^2 - 4m^2]} = \frac{m\pi}{2} g_m \Phi_m^r \quad (\text{C.150})$$

or

$$\left(\sum_{n=1}^{\infty} \frac{2(2n-1)^2}{\pi [(2n-1)^2 - 4m^2]} e_n \Theta_n^r \right) - m g_m \Phi_m^r = 0 \quad (\text{C.151})$$

Using Equation C.141 in C.151 yields

$$\sum_1^{\infty} e_n \left\{ \frac{2(2n-1)^2}{\pi [(2n-1)^2 - 4m^2]} \Theta_n^r + \frac{m\Phi_m^r}{\Psi_m^r} \frac{4(2n-1)}{\pi [(2n-1)^2 - 4m^2]} \Gamma_n^r \right\} = 0 \quad (\text{C.152})$$

C.5 Summary of Coefficient Equations

Enforcing the boundary conditions at the interface between regions (for example, between regions *a* and *b*) yields the following equations, which must be solved to determine the potential coefficients of the resistive solution:

$$\sum_{n=1}^{\infty} e_n \left[\Gamma_n^r \frac{4}{(2n-1)\pi} + \frac{s}{p} \Theta_n^r \right] = -1 \quad (\text{C.153})$$

$$\sum_{n=1}^{\infty} e_n \left\{ \frac{2(2n-1)^2}{\pi [(2n-1)^2 - 4m^2]} \Theta_n^r + \frac{m\Phi_m^r}{\Psi_m^r} \frac{4(2n-1)}{\pi [(2n-1)^2 - 4m^2]} \Gamma_n^r \right\} = 0 \quad (\text{C.154})$$

where *m* is a positive number and

$$\Gamma_n^r = \cosh \left[\frac{(2n-1)\pi}{4p} \right] \quad (\text{C.155})$$

$$\Theta_n^r = \sinh \left[\frac{(2n-1)\pi}{4p} \right] \quad (\text{C.156})$$

$$\Phi_m^r = \cosh \left(\frac{m\pi s}{2p} \right) \quad (\text{C.157})$$

$$\Psi_m^r = \sinh \left(\frac{m\pi s}{2p} \right) \quad (\text{C.158})$$

Once the e_n terms are found, the g_m terms and f_0 can be found from the following relationships:

$$f_0 = \frac{1}{p} \sum_{n=1}^{\infty} e_n \Theta_n^r \quad (\text{C.159})$$

$$g_m = -\frac{1}{\Psi_m^r} \sum_{n=1}^{\infty} e_n \Gamma_n^r \frac{4(2n-1)}{\pi [(2n-1)^2 - 4m^2]} \quad (\text{C.160})$$

Appendix D. *List of Symbols*

<u>Symbol</u>	<u>Description</u>
α	Substitution variable used in potential solutions
a_n	Potential coefficients for layer 2
A_n	Arbitrary constant used in potential solutions
b_n	Potential coefficients for layer 3
B_n	Arbitrary constant used in potential solutions
c	Velocity of light
cm	Centimeters
c_n	Potential coefficients for layer 3
C_E	Capacitance between electrodes
C_g	Capacitance from one electrode to ground
C_i	Capacitance associated with insulator
C_n	Arbitrary constant used in potential solutions
C_s	Capacitance associated with substrate
C_T	Total capacitance between electrodes with one grounded
d	Insulator thickness, normalized to the electrode's width
d_n	Potential coefficients for layer 4
D_n	Arbitrary constant used in potential solutions
ϵ	Permittivity
$\epsilon_{r,z}$	Dielectric constant in layer z ($z = 1, 2, 3, 4, 5$)
ϵ_z^*	Complex dielectric constant in layer z ($z = 2, 3, 4, 5$)
E	Electric Field
e_n	Potential coefficient for regions a and c
F	Farads

<u>Symbol</u>	<u>Description</u>
$\mathcal{F}_n^4(y)$	Quantity used in the capacitive solution
f_0	Potential coefficient for region b
f_L	Critical frequency imposed by length L
f_p	Transition frequency of the sensor coating
$f(x)$	Quantity used in capacitive solution
Γ_n^c	Quantity used in capacitive solution
Γ_n^r	Quantity used in resistive solution
g_n	Potential coefficient for region b
G	Conductance
$g(x)$	Quantity used in capacitive solution
H	Magnetic Field
$\mathcal{H}_n^4(y)$	Quantity used in capacitive solution
h	Electrode height, normalized to the electrode's width
Hz	Hertz
\mathcal{I}_m	Quantity used in capacitive solution
I_m^1	Quantity used in capacitive solution
I_m^2	Quantity used in capacitive solution
I_{mn}^3	Quantity used in capacitive solution
I_{mn}^{3a}	Quantity used in capacitive solution
I_{mn}^{3b}	Quantity used in capacitive solution
I	Current
J	Current density
j	Complex number equal to $\sqrt{-1}$
k	Wavenumber

<u>Symbol</u>	<u>Description</u>
λ_z	Eigenvalue of layer/region z ($z = 2, 3, 4, 5, a, b, c$)
L	Length of the interdigitated structure
l	Thickness of sensor coating and electrode, normalized to the electrode's width
\mathcal{U}	Mhos
μ	Permeability
Ω	Ohms
ω	Angular frequency
ω_L	Critical angular frequency imposed by length L
ω_p	Angular transition frequency of the sensor coating
$\omega_3(x, y)$	Quantity used in capacitive solution
$\omega_a(x, y)$	Quantities used in resistive solution
$\omega_c(x, y)$	Quantities used in resistive solution
$\Phi(y)$	Quantity used in potential solutions
Φ_n^c	Quantity used in capacitive solution
Φ_n^r	Quantity used in resistive solution
$\Psi(x)$	Quantity used in potential solutions
Ψ_n^{even}	Quantity used in charge symmetry analysis
Ψ_n^{odd}	Quantity used in charge symmetry analysis
Ψ_n^{3even}	Quantity used in charge symmetry analysis
Ψ_n^{3odd}	Quantity used in charge symmetry analysis
Ψ_n^c	Quantity used in capacitive solution
Ψ_n^r	Quantity used in resistive solution
$\phi_z(x, y)$	Potential in layer/region z ($z = 2, 3, 4, 5, a, b, c$)
ϕ_n^z	Eigenfunction of layer z ($z = 2, 3, 4, 5$)

<u>Symbol</u>	<u>Description</u>
pF	Pico (10^{-12}) Farads
p	Sensor coating thickness, normalized to electrode's width
Q	Charge on one electrode
Q_1	Quantity used in charge symmetry analysis
Q_2	Quantity used in charge symmetry analysis
Q_3	Quantity used in charge symmetry analysis
Q_4	Quantity used in charge symmetry analysis
Q_5	Quantity used in charge symmetry analysis
Q^{even}	Quantity used in charge symmetry analysis
Q^{odd}	Quantity used in charge symmetry analysis
Q_2	Quantity used in charge calculations
Q_2^a	Quantity used in charge calculations
Q_2^{a1}	Quantity used in charge calculations
Q_2^{a2}	Quantity used in charge calculations
Q_2^b	Quantity used in charge calculations
Q_3	Quantity used in charge calculations
Q_4	Quantity used in charge calculations
Q_4^a	Quantity used in charge calculations
Q_4^b	Quantity used in charge calculations
ρ	Charge density
R_p	Resistance through the sensor coating layer
R_s	Resistance through the substrate
σ_z	Conductivity in layer z ($z = 1, 2, 3, 4, 5$)
s	Electrode separation, normalized to electrode's width

<u>Symbol</u>	<u>Description</u>
τ	Substitution variable used in potential solutions
Θ_n^c	Quantity used in capacitive solution
Θ_n^r	Quantity used in resistive solution
$v_3(x)$	Quantity used in capacitive solution
v_a	Quantity used in resistive solution for region a
v_c	Quantity used in resistive solution for region c
V	Voltage
V_z	Voltage of electrode z ($z = 1, 2$)

Bibliography

1. AFIT/ENP, Wright-Patterson AFB, OH. *METALIB, UNIX Programmer's Manual*, March 1989.
2. Alley, Gary D. "Interdigital Capacitors and Their Application to Lumped-Element Microwave Integrated Circuits," *IEEE Transactions on Microwave Theory and Techniques*, MTT-18(12):1028-1033 (December 1970).
3. Collins, Robert E. *Field Theory of Guided Waves*. New York, NY: McGraw-Hill Book Company, 1960.
4. Cotts, D. and Z. Reyes. *Electrically Conductive Organic Polymers for Advanced Applications*. Park Ridge, NJ: Noyes Data Corporation, 1986.
5. Dalby, Arne Brejning. "Interdigital Microstrip Parameters Using Empirical Formulas and Simplified Model," *IEEE Transactions on Microwave Theory and Techniques*, MTT-27(8):744-752 (August 1979).
6. Hill, Y. M. *et al.* "A General Method for Obtaining Impedance and Coupling Characteristics of Practical Microstrip and Triplate Transmission Line Configurations," *IBM Journal of Research and Development*, 13:314-322 (1969).
7. IMSL, Inc., Houston, TX. *IMSL MATH/LIBRARY, User's Manual*, April 1987.
8. Judd, S. V. *et al.* "An Analytical Method for Calculating Microstrip Transmission Lines Parameters," *IEEE Transactions on Microwave Theory and Techniques*, MTT-18(2):78-87 (February 1970).
9. Kitazawa, Toshihide. "Metallization Thickness Effects of Striplines with Anisotropic Media: Quasi-Static and Hybrid-Mode Analysis," *IEEE Transactions on Microwave Theory and Techniques*, MTT-37(4):769-775 (April 1989).
10. Kitazawa, Toshihide and Yoshio Hayashi. "Propagation Characteristics of Striplines with Multilayered Anisotropic Media," *IEEE Transactions on Microwave Theory and Techniques*, MTT-31(6):429-433 (June 1983).
11. Kitazawa, Toshihide and Yoshio Hayashi. "Asymmetrical Three-Line Coupled Striplines with Anisotropic Substrates," *IEEE Transactions on Microwave Theory and Techniques*, MTT-34(7):767-771 (July 1986).
12. Krage, Mark L. and George I. Haddad. "Frequency-Dependent Characteristics of Microstrip Transmission Lines," *IEEE Transactions on Microwave Theory and Techniques*, MTT-20(10):678-688 (October 1972).
13. Kraus, John D. *Electromagnetics* (Third Edition). New York, NY: McGraw-Hill Book Company, 1984.
14. Lee, Huan Lim. *Optimization of a Resin Cure Sensor*. MS thesis, Massachusetts Institute of Technology, Cambridge MA, 1982.
15. Smith, J. I. "The Even- and Odd-Mode Capacitance Parameters for Coupled Lines in Suspended Substrate," *IEEE Transactions on Microwave Theory and Techniques*, MTT-19(5):324-328 (May 1971).
16. Sze, S. M. *Semiconductor Devices, Physics and Technology*. New York, NY: John Wiley and Sons, 1985.

17. Weeks, William T. "Calculation of Coefficients of Capacitance of Multiconductor Transmission Lines in the Presence of a Dielectric Interface," *IEEE Transactions on Microwave Theory and Techniques*, MTT-18(1):35-43 (January 1970).
18. Wiseman, John M. *Investigation of the Impedance Modulation of Thin Films with a Chemically-Sensitive Field-Effect Transistor*. MS thesis, AFIT/GE/ENG/88D-6.61, 1988.
19. Yamashita, Eikichi and Kazuhiko Atsuki. "Strip Line with Rectangular Outer Conductor and Three Dielectric Layers," *IEEE Transactions on Microwave Theory and Techniques*, MTT-18(5):238-244 (May 1970).

Vita

Captain Henry P. Leal [REDACTED] He graduated from Eureka Senior High School in Eureka, California, and joined the USAF in 1973. After completing basic training, he served as a Cryptographic Equipment Systems Technician until entering the University of Washington under the Airman Education and Commissioning Program in March 1980. In August 1982, he graduated Magna Cum Laude and received the degree of Bachelor of Science in Electrical Engineering. In November 1982, he received a USAF commission and served as an engineering Project Officer at the Air Force Satellite Control Facility, Sunnyvale AFS, California, until October 1985. He then served as the Deputy Commander of the Vandenberg Tracking Station, Vandenberg AFB, California, until entering the School of Engineering, Air Force Institute of Technology, in May 1988.

[REDACTED]

REPORT DOCUMENTATION PAGE

Form Approved
OMB No. 0704-0188

1a. REPORT SECURITY CLASSIFICATION UNCLASSIFIED			1b. RESTRICTIVE MARKINGS		
2a. SECURITY CLASSIFICATION AUTHORITY			3. DISTRIBUTION / AVAILABILITY OF REPORT Approved for Public Release; Distribution Unlimited		
2b. DECLASSIFICATION / DOWNGRADING SCHEDULE					
4. PERFORMING ORGANIZATION REPORT NUMBER(S) AFIT/GE/MA/89D-1			5. MONITORING ORGANIZATION REPORT NUMBER(S)		
6a. NAME OF PERFORMING ORGANIZATION School of Engineering	6b. OFFICE SYMBOL (If applicable) AFIT/EN	7a. NAME OF MONITORING ORGANIZATION			
6c. ADDRESS (City, State, and ZIP Code) Air Force Institute of Technology Wright-Patterson AFB, OH 45433		7b. ADDRESS (City, State, and ZIP Code)			
8a. NAME OF FUNDING / SPONSORING ORGANIZATION	8b. OFFICE SYMBOL (If applicable)	9. PROCUREMENT INSTRUMENT IDENTIFICATION NUMBER			
8c. ADDRESS (City, State, and ZIP Code)		10. SOURCE OF FUNDING NUMBERS			
		PROGRAM ELEMENT NO.	PROJECT NO.	TASK NO.	WORK UNIT ACCESSION NO.
11. TITLE (Include Security Classification) RIGOROUS CALCULATIONS OF LUMPED ELECTRICAL PARAMETERS FOR A MICROSTRIP INTERDIGITATED ELECTRODE STRUCTURE					
12. PERSONAL AUTHOR(S) Henry P. Leal, Capt, USAF					
13a. TYPE OF REPORT MS Thesis	13b. TIME COVERED FROM _____ TO _____	14. DATE OF REPORT (Year, Month, Day) 1989 December		15. PAGE COUNT	
16. SUPPLEMENTARY NOTATION					
17. COSATI CODES			18. SUBJECT TERMS (Continue on reverse if necessary and identify by block number)		
FIELD	GROUP	SUB-GROUP	Interdigitated electrode parameters, coupled microstrip parameters, interdigitated microstrip parameters, interdigitated electrode structure electrical model.		
19. ABSTRACT (Continue on reverse if necessary and identify by block number)					
<p>This research investigates a microstrip interdigitated electrode structure used in integrated circuit sensors and presents an electrical model for the device. The structure is assumed to: (1) have a periodic arrangement of interdigitated electrodes, (2) have electrodes of sufficient length to ignore effects created by the ends of the structure, (3) be operating at a sufficiently low frequency, where the potential is essentially constant along the electrode's length and where the substrate is essentially a conductor, and finally (4) have five layers of homogeneous, isotropic, non-magnetic material in the plane transverse to the structure's length. Within these constraints, the problem focuses on solving for the potential distribution using Laplace's equation.</p> <p>The electrical model developed consists of three elements--a capacitance from each of two electrodes to ground, a capacitance between the electrodes, and a resistance through the sensor coating. The values for the individual elements are found from the</p>					
20. DISTRIBUTION / AVAILABILITY OF ABSTRACT <input type="checkbox"/> UNCLASSIFIED/UNLIMITED <input checked="" type="checkbox"/> SAME AS RPT. <input type="checkbox"/> DTIC USERS			21. ABSTRACT SECURITY CLASSIFICATION UNCLASSIFIED		
22a. NAME OF RESPONSIBLE INDIVIDUAL Capt Henry P. Leal			22b. TELEPHONE (Include Area Code) 513-255-3030		22c. OFFICE SYMBOL AFIT/EN

item 19 (continued):

potential solution. Potential functions, in the form of infinite Fourier series, are developed for each layer within a periodic cell. The coefficients of the Fourier series are determined by matching boundary conditions across interfaces between the material layers. These coefficients are estimated numerically by truncating the infinite series, and solving a linear system of equations.

Results are presented for a variety of cell parameters (cell dimensions and material properties), which illustrate the dependence of the individual elements on these cell parameters. Specifically, the results indicate that all model elements are strongly influenced by the electrical properties of the sensor coating; and therefore, all elements play a major role in the sensing action of the device. The frequency dependence of the model parameters are also developed, using a complex permittivity. Results are presented for various material parameters, which illustrate the high and low frequency limits of all model elements with a transition centered at the frequency where the sensor coating changes from a conductor to a lossy dielectric.

Thesis Chairman: Gregory T. Warhola, Capt, USAF
Assistant Professor of Applied Mathematics